THE DESIGN OF AN IMPULSE METER TO CHARACTERISE VERTICAL BLAST LOADS

by

Kurt Ralph Strydom

Thesis presented at the University of Stellenbosch in partial fulfilment of the requirements for the degree of

Master of Science in Mechanical Engineering

Department of Mechanical and Mechatronic Engineering
Stellenbosch University
Private Bag X1, 7602 Matieland, South Africa

Study Leaders: Prof G.N. Nurick — University of Cape Town
Mr K. van der Westhuizen — University of Stellenbosch

March 2007

Declaration

I, Kurt Ralph Strydom, hereby declare that the work contained in this thesis is my own original work and that I have not previously in its entirety or in part submitted it at any university for a degree.

Signature: .

K.R. Strydom

Date: 6/03/2007

Abstract

The Design of an Impulse Meter to Characterise Vertical Blast Loads

Kurt Ralph Strydom

Department of Mechanical and Mechatronic Engineering

Stellenbosch University

Private Bag X1, 7602 Matieland, South Africa

Thesis: MScEng (Mech)

March 2007

This report covers the development of an impulse meter for the characterization of vertically applied blast loads in terms of total impulse transferred to a test structure. The Spring-Mass Impulse Meter (SMI) was developed for the Blast Impact and Survivability Research Unit (BISRU) based at the University of Cape Town (UCT). The SMI was developed specifically for the measurement of impulses due to the momentum transfer between blasts from soil buried charges and thin plates or small structures for landmine related research. Several impulse measurement methods and concepts were investigated and compared; the SMI was shown by qualitative comparisons to be the concept that is most likely to satisfy BISRU's needs. The resulting SMI structure was analysed using Finite Element Analysis to confirm its structural integrity and acceptable dynamic response. The system dynamics and impulse response were analysed and optimised using single degree of freedom spring-mass models. The SMI was manufactured, installed at UCT and also calibrated against a horizontal ballistic pendulum with a series of bulge tests. The calibration tests were done on plates with thicknesses ranging from 1.6 mm to 4 mm using PE4 plastic explosive as the impulse source. Tests results showed the SMI to be capable of measuring impulses between 10 N·s and 75 N·s with accuracy and repeatability similar to that of a ballistic pendulum.

Opsomming

Die Ontwerp van 'n Impulsmeter vir die Karakterisering van Vertikale Plofbelastings

Kurt Ralph Strydom

Departement Meganiese en Megatroniese Ingenieurswese

Universiteit Stellenbosch

Privaatsak X1, 7602 Matieland, Suid Afrika

Tesis: MScIng (Meg)

Maart 2007

Hierdie verslag dek die ontwikkeling van 'n impulsmeter met die doel om vertikale plofbelastings te karakteriseer in terme van totale impuls oorgerdra aan 'n toetsstruktuur. Die Veer-massa Impuls meter, "*Spring-Mass Impulse Meter*" (SMI) is ontwikkel vir die "*Blast Impact and Survivability Research Unit*" (BISRU) wat by die Universiteit van Kaapstad gesetel is. SMI is spesifiek ontwikkel vir die meting van impuls as gevolg van die momentum oordrag tussen ontploffings vanaf grondbedekte plofladings en dun plate of kleiner strukture vir landmyn navorsing. 'n Aantal verskillende impuls meet-metodes en konsepte is ondersoek en vergelyk, die SMI is deur middel van kwalitatiewe vergelyking uitgewys as die konsep wat die grootste potensiaal het om aan BISRU se behoeftes te voorsien. Die gevolglike SMI struktuur is met Eindige Element Analises ondersoek om strukturele integriteit en aanvaarbare dinamiese respons te bevestig. Die stelsel dinamika en impuls respons is met behulp van een vryheidsgraad veer-massa modelle bestudeer en geoptimeer. Die SMI stelsel is vervaardig, by die Universiteit van Kaapstad geinstalleer en ook gekalibreer met betrekking tot 'n horisontale ballistiese pendulum tydens 'n reeks van plaat-duik toetse. Die kalibrasie en aanvaardingstoetse is op plate met diktes tussen 1.6 mm en 4 mm gedoen met PE4 springstof as impulsbron. Die toets resultate het getoon dat die SMI stelsel in staat was om impuls tussen 10 N·s en 75 N·s te meet met akkuraatheid wat vergelykbaar is met dié van 'n horisontale ballistiese pendulum.

Acknowledgements

Deo Optimo Maximo!

I wish to thank the following people for their contributions to this project:

My study leaders, Prof. Gerald Nurick and Mr. Kobus van der Westhuizen. Professor Nurick for his patience, guidance and help with the difficult qualification tests.
Mr. Van der Westhuizen for his support and guidance in the FE work and his editorial input.

Armscor and the National Research Foundation for funding this research.
Trevor Cloete for his advice and ideas, particularly the concept of an SMI.
Keith Balchin for his help in organising the installation of the SMI system.
Ferdi Zietsman for his excellent technical advice and the time he spent helping me to manufacture and install the SMI.
Johann du Toit for his support and understanding.

The team of people who did the heavy work during testing, by changing specimens and mounting the ballast mass:

Calvin Hammerse
Darren Pierce
Arno Verburg
Adriaan van der Westhuizen
Nicol du Toit
Francois du Toit

I would like to thank my late father Koot Strydom, my mother Tilly and brothers Eben, Rocco and Ockert for their inspiration and for instilling in me the love for all things that move, make noise, involve power and that harness man's knowledge of nature.

Contents

List of Tables

List of Figures

Nomenclature

A	Amplitude of vibration, [m]
c	Viscous damping coefficient, [N·s/m]
D	Cowper-Symonds reference strain rate, [s^{-1}]
	Burn diameter, [m]
d	Diameter, [m]
E	Youngs modulus, [N/m^2]
E_k	Kinetic energy, [J]
E_p	Potential energy, [J]
F_g	Gravitational force, [N]
F_k	Spring force, [N]
f	Force, [N]
g	Gravitational acceleration, [m/s^2]
h	Height, [m]
h_{max}	Maximum height, [m]
I	Impulse, [N·s]
k	Spring stiffness, [N/m]
L	Pendulum rod or tether length, [m]
m	Mass, [kg]
N	Normal force, [N]
n	Cowper-Symonds material property
P	Pressure, [Pa]
t	Time, [s]
V_{burn}	Burn Velocity, [m/s]
v	Velocity, [m/s]
v_0	Initial velocity, [m/s]
x	Deflection from the equilibrium point of a system, [m]
x_{max}	Peak horizontal deflection, [m]
$\dot{x}$	Velocity, [m/s]
$\ddot{x}$	Acceleration, [m/s^2]
Δv	Change in velocity, [m/s]

δ/t	Deflection thickness ratio
ε_A	Amplitude measurement error factor
ε_{km}	Stiffness and mass measurement error factor
ε_{ULT}	Ultimate tensile strain
ζ	Damping ratio
θ	Angle, [rad]
μ	Dynamic friction coefficient
ρ	Density, [kg/m^3]
σ	Stress, [N/m^2]
σ_{YT0}	Static tensile yield stress, [N/m^2]
τ	Period of oscillation, event duration [s]
Φ	Nurick dimensionless number
ω_n	Natural frequency of a system, [rad/s]

Acronyms

BISRU	Blast Impact and Survivability Research Unit
CAD	Computer Aided Draugthing and Design
COG	Centre of Gravity
EMI	Electromagnetic Interference
FEA	Finite Element Analysis
FEM	Finite Element Method
LED	Light Emitting Diode
LVDT	Linear Variable Differential Transformer
SHM	Simple Harmonic Motion
SMI	Spring Mass Impulse Meter
SMI25	25 N·s module of the Spring Mass Impulse meter system
SMI50	50 N·s module of the Spring Mass Impulse meter system
SMI75	75 N·s module of the Spring Mass Impulse meter system
SMI100	100 N·s theoretical module of the Spring Mass Impulse meter system
UCT	University of Cape Town
1-DOF	Single Degree of Freedom

1. Introduction

Impulse is the integral of an applied force over time and it is one of the most important parameters used to characterise an impact, since it can be used as a general expression of the magnitude of an impact or suddenly applied force. Therefore it is logical that accurate impulse measurement will be one of the most important aspects of impact related experiments. For example, the response of a plate structure will vary according to the impulsive forces applied to it, ranging from large plastic deformation, to tearing and fragmentation. The ability to accurately characterise blast loads and the response of structures due to similar loads will greatly aid in the design of structures to contain or resist blast loads.

According to Nurick and Martin (1989), since the early 1950's a large amount of research has been performed on the response of thin plates subjected to impulsive loads. These experiments relied on various impulse sources, varying from underwater blasts, air-blasts from explosive sources to direct impulsive loading. The most common measurements made in these types of experiments were explosive mass, standoff distance, deformed plate shape, applied impulse and deformation-time history.

BISRU and its predecessors have used a horizontal ballistic pendulum to measure applied impulse for more than 20 years. Ballistic pendulums are simple or compound pendulums that are instrumented to measure pendulum deflection amplitude after an impulse is applied to the pendulum. The applied impulse is then calculated from the simple impulse response equation of the ballistic pendulum.

A common problem with the horizontal ballistic pendulum is that its line of action is orthogonal to gravity, making it difficult to use it to do research into buried charges. As this type of research is of great importance in the design of landmine resistant structures it was decided that the development of a device for the characterization of vertical blast waves would be of strategic interest to BISRU.

In the absence of data on the momentum transfer from buried charges to plate specimens it was decided to build a device that could measure impulses up to 100 N·s.

If an impulse of this magnitude is applied using an air blast it would require a charge with a mass in the order of 50 g of PE4, which is well within the 75 g rating of the UCT blast cell.

It was also decided that the device must be able to perform the thin plate bulge tests with which BISRU has considerable experience. This would aid the calibration and test development of the new device against the existing horizontal ballistic pendulum. Another desirable feature is that the new device must be able to use most of the existing jigs that are used on the horizontal ballistic pendulum.

2. Background

Impulse is the result of a suddenly applied force, and manifests itself as a sudden change in the momentum and velocity of the body on which it is applied. Ideally an impulse results in an instantaneous velocity change due to a sudden application of force. In most real systems the change in velocity is very rapid, but not instantaneous.

2.1. Impulse measurement

2.1.1. Direct measurement

The direct measurement of impulse entails measuring the velocity of a test specimen during and after the application of an impulse. Alternatively the impulse may be calculated from the integration of the acceleration history or differentiation of the displacement time history. Impulse can also be calculated from the temporal integration of the pressure or force applied to a body. In many cases the response of the test specimen may be a function of the impulse shape, and the dynamic response of the support structure, adding a further variable to the measurements.

The above mentioned methods are potentially the most accurate in determining impulse, but are extremely difficult and costly to perform. The speed at which the forces are applied necessitates the use of very fast data sampling. Small measurement and integration errors in the time domain have serious detrimental effects on the accuracy of these methods.

2.1.2. Indirect measurement

Indirect measurement of impulse may be made by applying the impulse to a test specimen that forms part of a system or mechanism that has a well known impulse response. The applied impulse can then be calculated using the system's known impulse response. Indirect impulse measurement is usually only used to calculate total impulse.

If the period of the impulse is significantly smaller than that of the first mode of oscillation of the measurement system it may be assumed that the system will give an

accurate measurement of the applied impulse. This type of measurement system integrates the applied impulse mechanically and measures the total impulse with no sensitivity to the specific shape of the impulse. The ballistic pendulum is a good example of such a device.

Another indirect method for impulse estimation is to do calibrated experiments where the impulse delivered by a given mass of explosive in a specific loading condition is well known. This method does not account for the effect that reflected shock waves and poor detonation may have on the applied impulse.

2.2. The ballistic pendulum

A ballistic pendulum is the simplest device used for measuring impulse. Simply stated, it consists of a mass suspended by long thin cables, forming a compound pendulum.

The pendulum mass comprises of the test specimen and clamping jig that are fixed to one end of an I-beam, which forms the main mass, and a set of balancing masses on the opposite end of the I-beam. The purpose of the balancing masses is to keep the principal axis of inertia of the pendulum mass orthogonal to gravity. Figure 2.1 shows an example of the horizontal pendulum system used by BISRU.

The impulse vector is applied through the centre of gravity of the ballistic pendulum and ideally collinear to the principal axis of inertia. After the impulse is applied the pendulum goes into simple harmonic motion (SHM) as the energy in the system is converted between kinetic energy and gravitational potential energy. During this motion the peak deflection amplitude is recorded and later used to calculate the applied impulse.

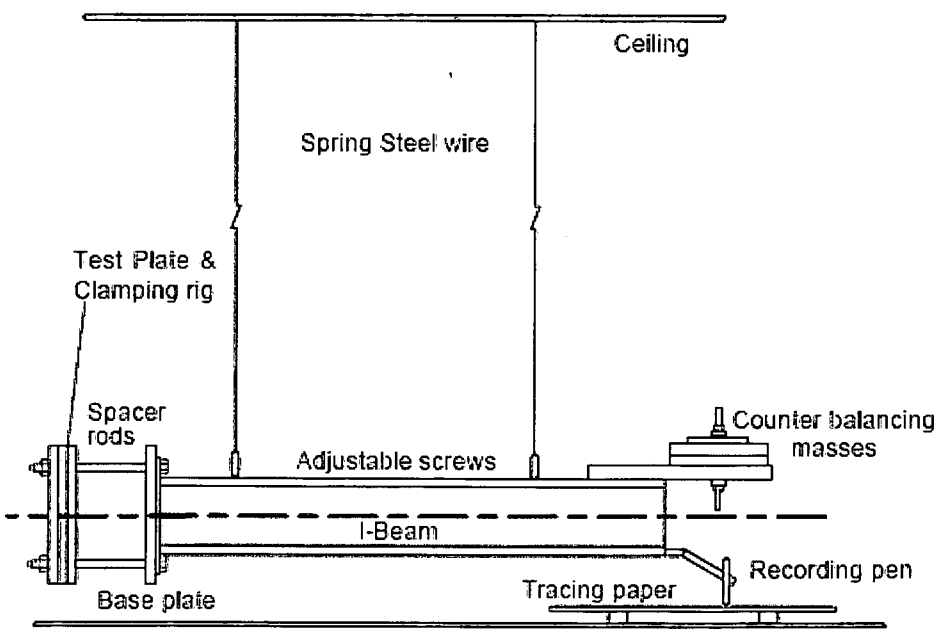

Figure 2.1: A horizontal ballistic pendulum (Jacob et.al., 2004).

A simple pendulum with mass m suspended by a tether of length l is presented in Figure 2.2. If a horizontal impulse is applied to the initially stationary mass, it will suddenly gain momentum and have an initial velocity v_0. The kinetic energy E_k gained due to the sudden motion may be stated as follows:

$$E_k = \frac{1}{2} m v_0^2 \qquad \textbf{Equation 2.1}$$

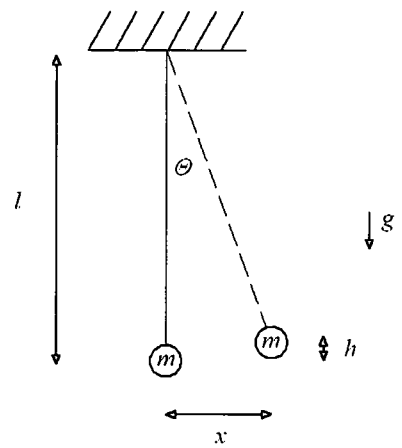

Figure 2.2 A simple pendulum shown in equilibrium and with exaggerated deflection.

During SHM the pendulum mass will tend to move parallel to the horizontal impulse vector, but due to the constraining effect of the tether it will move in a large radius arc. This curvilinear motion results in a simultaneous vertical and horizontal motion, x and h respectively. The vertical motion does work against gravity which is a conservative force, allowing the problem to be solved using energy methods. Work done by the pendulum against gravity converts kinetic energy into gravitational potential energy E_p, which can be written as:

$$E_p = mgh \qquad \textbf{Equation 2.2}$$

By equating the kinetic and potential energies it is possible to form an expression for the initial velocity, v_0 in terms of the peak height h_{max} to which the pendulum moved.

$$E_k = E_p \qquad \textbf{Equation 2.3}$$

$$\frac{1}{2} m v_0^2 = mgh_{\max} \qquad \textbf{Equation 2.4}$$

$$v_0^2 = 2gh_{max} \qquad \textbf{Equation 2.5}$$

$$v_0 = \sqrt{2gh_{max}} \qquad \textbf{Equation 2.6}$$

The peak height however, is not as convenient to measure as the peak horizontal deflection x_{max}. Most horizontal ballistic pendulums only record the horizontal deflection and it is therefore necessary to derive an expression for h in terms of x. The vertical and horizontal deflection of the mass, h and x, can both be expressed as functions of the tether angle θ.

$$h = l[1 - \cos(\theta)] \qquad \textbf{Equation 2.7}$$

$$x = l\sin(\theta) \qquad \textbf{Equation 2.8}$$

Equations 2.8 can be rewritten to give the deflection angle in terms of the horizontal deflection.

$$\theta = \arcsin\left(\frac{x}{l}\right) \qquad \textbf{Equation 2.9}$$

This expression for the deflection angle can then be substituted into Equation 2.7 to give the vertical deflection in terms of the measured horizontal deflection.

$$h = l\left[1 - \cos\left(\arcsin\left(\frac{x}{l}\right)\right)\right] \qquad \textbf{Equation 2.10}$$

Equation 2.10 can now be substituted into Equation 2.6 to give the initial velocity in terms of the peak horizontal deflection.

$$v_0 = \sqrt{2gl\left[1 - \cos\left(\arcsin\left(\frac{x_{max}}{l}\right)\right)\right]} \qquad \textbf{Equation 2.11}$$

This expression for the initial velocity can be used in the impulse momentum equation, Equation 2.12, to calculate the applied impulse from the peak horizontal deflection.

$$I = mv_0 \qquad \textbf{Equation 2.12}$$

Thus if the pendulum's mass, tether length, peak horizontal deflection and the gravitational acceleration is known, the preceding four equations may be combined to yield the applied impulse:

$$I = m\sqrt{2gl\left[1-\cos\left(\arcsin\left(\frac{x_{\max}}{l}\right)\right)\right]} \qquad \textbf{Equation 2.13}$$

where:

Applied impulse	$= I$
Pendulum mass	$= m$
Gravitational acceleration	$= g$
Tether length	$= l$
Peak horizontal deflection	$= x_{max}$

2.3. Other devices

The Canadian Centre for Mine Action Technology (2006 presents the devices shown in Figure 2.3 and Figure 2.4on its website. These devices seem to be instrumented to measure the force exerted by a blast load on a structure. The explosive charges or mine simulators would then be buried in the soil bins shown. Very little detail was given on these devices, but the pictures give a good indication of the size and construction methods used in these types of tests.

Figure 2.3: Canadian Centre for Mine Action Technologies (2006) apparatus for the measurement of blast effects from small buried charges. Rating 100 g C4.

Figure 2.4: Canadian Centre for Mine Action Technologies (2006) apparatus for the measurement of blast effects from larger buried charges. Rating 2 kg C4. Total load is measured with four large force transducers.

2.4. Preliminary FEA

The experimental work presented in this thesis was based on plate bulge experiments; one of the reasons for this is the large pool of experimental data available. A second, more important reason for using bulge tests were their relative simplicity. With fewer variables than buried charges, plate bulge tests ensure that calibration tests can be more accurately and consistently compared due to less possible experimental variation.

Plate bulge tests have been extensively studied by several authors and a thorough study of the work done prior to 1988 is presented by Nurick and Martin (1989) in a two part article that reviewed the theoretical predictions and the experimental work done on impulsively loaded plates. Their first part compares and discusses 22 numerical methods used to predict the midpoint displacement of circular and square plate specimens, while the second part of the article discusses the experimental studies on plate response. Detail descriptions of the methods used by different authors to generate impulse as well as the methods they used to measure deformation-time histories are given in the second part.

The second article also refers to the particularly important work performed by Humphreys (1965), whom by means of high speed photography, recorded the deformation-time histories of explosively loaded beam specimens mounted on ballistic pendulums. It is reported that Humphreys confirmed the two key assumptions to the successful use of a ballistic pendulum. Firstly, that the impulse application occurs with negligible pendulum motion. This implies that the system remains at its equilibrium position due to its own inertia and that the tethers therefore exert negligible force on the pendulum during impulse application, confirming the applicability of conservation of momentum. Furthermore, he proved that for large period pendulums, the specimen deformation occurs so rapidly that the pendulum undergoes negligible motion during the deformation; therefore the shift in the COG of the pendulum would have a negligible effect on the recorded pendulum motion.

The second article also proposes considerable modifications to Johnson's dimensionless damage parameter α, Equation 2.14, defined by Johnson (1972). Johnson's dimensionless damage parameter was initially used to asses the impact behaviour of

metals, but was modified in order to allow the comparison of experiments based on different specimen dimensions.

$$\alpha = \frac{\rho v^2}{\sigma_d} or \frac{I^2}{A^2 t^2 \rho \sigma_d} \qquad \textbf{Equation 2.14}$$

Where:

Material density	ρ
Impact velocity	v
Damage stress	σ_d
Impulse	I
Area of the plate	A
Material thickness	t

The "modified damage number, Φ" which they proposed is what is today known as the Nurick dimensionless number Φ, shown in Equation 2.15. Unlike any previous damage parameter, the Nurick dimensionless number accounted for specimen geometry and loading geometry, which allowed different specimen and load geometry combinations in different materials to be compared. A least squares analysis of the deflection-thickness ratio, shown in Equation 2.16, versus the Nurick dimensionless number of 109 circular specimen data in points is presented. The equation that characterises the fit is shown in Equation 2.17.

$$\Phi = \frac{I\left(1+\ln\left(R/R_o\right)\right)}{\pi R t^2 \sqrt{\rho \sigma_0}} \qquad \textbf{Equation 2.15}$$

Where:

Loaded radius	R_0
Plate radius	R
Material static yield stress	σ_0

$$\frac{\delta}{t}$$ **Equation 2.16**

Where:

Measured midpoint deflection δ

$$\frac{\delta}{t} = 0.425\Phi + 0.277$$ **Equation 2.17**

The paper also notes that most of the data points fall within a ±1 deflection-thickness ratio confidence limit about the least squares fit described above.

A conference paper by Nurick (1989) further supports the importance of the ±1 deflection-thickness ratio confidence limit about the least squares fit. In this paper Nurick again explains his dimensionless number as an extension to the Johnson dimensionless damage number, but adds that the results of a statistical analysis showed that 90% of circular specimen data points should lay within a ±0.98 deflection-thickness ratio offset of the least squares fit. The 99% confidence limit is reported to be ±1.99 deflection-thickness ratio.

Thus the Nurick dimensionless number is a common technique used to compare new test data with published data. New data may be deemed trustworthy if it falls within the confidence limits of the least squares fit presented by Nurick since it follows the trends of previous data.

A good example of Finite Element modelling of plate bulge tests can be found in Olson et.al. (1993). The paper primarily investigates the dynamic response of square plate specimens at impulsive loadings sufficient to cause partial or complete tearing at specimen boundaries. Analyses were performed using a non-linear FE program, NAPSSE, with special purpose plate elements. Like most FE models of this nature it took advantage of the quarter symmetry of the problem, and only a quarter of the total specimen geometry was modelled. Olson et.al. reported that their modelling efforts succeeded in predicting not only the peak midpoint displacement accurately, but also the deformed shape of the specimens showing large inelastic deformation. The material model they used included a dynamic yield stresses model, using the Cowper-Symonds relationship described by Jones (1989), shown in Equation 2.18. The Cowper-Symonds

relationship calculates the dynamic yield stress σ_d, by adjusting the static yield stress σ_0 according to two material parameters, n and D, and the strain rate $\dot{\varepsilon}$.

$$\sigma_y = \sigma_0 \left[1 + \left|\dot{\varepsilon}/D\right|^{1/n}\right] \qquad \textbf{Equation 2.18}$$

The inclusion of the strain rate dependent yield strength such as this is essential in modelling the high and moderate strain rate response of materials such as mild steel, which show marked strain rate strengthening. Certain metals such as aluminium alloys show much less strain rate sensitivity and the Cowper-Symonds relationship is less prominent in modelling the response of those metals.

Olson et.al. used a special charge geometry aimed at delivering a pressure pulse that was evenly distributed over the face of the specimen. For this reason they modelled the impulsive load as an evenly distributed pressure load on the face of the specimen. The profile of the pressure loading was assumed to be of a square form and it is reported that the duration of the impulse was also assumed to be 15 μs. The magnitude of the pressure load was calculated using the assumed duration and the size of the loaded area. Despite the crude definition of the loading Olson et.al. was able to model the deformed profile accurately to within less than a deflection-thickness ratio.

Questions about accuracy do however arise from the load model used by Olson et.al. The accuracy of three types of load modelling techniques for FEA models was investigated by Farrow et.al. (1995). Their analysis of circular specimens was performed with the ABAQUS FE code's implicit solution scheme using axisymmetric shell elements and a material model similar to that of Olson et.al. The load models which were compared included a constant initial transverse velocity profile, a triangular shaped initial transverse velocity profile and an evenly distributed pressure load. They assumed the pressure load to be constant over the burn period of the explosive charge, which was also assumed to be 15 μs, similar to the assumptions of Olson et.al. These assumptions were based on the geometry of the charges they used. The results of the FEA predictions were compared using a non-dimensional analysis based on the Nurick dimensionless number and plate deflection-thickness ratio. The results of the comparison clearly shows that the triangular initial velocity profile over predicts the least squares fit calculated by Nurick and Martin (1989) by a plate deflection-thickness

ratio. The uniform velocity approach and the even pressure load were found to match the least squares fit remarkably well.

A more recent paper by Jacob et.al. (2004) titled "Scaling aspects of quadrangular plates subjected to localised blast loads — experiments and predictions" also performs some modelling of the blast loading of plate specimens. Their numerical work was performed using the general FEA package, ABAQUS\Explicit using eight node hexahedral elements. The use of solid elements allowed the simulation of shock propagation through the plate thickness, something that was not possible with plate elements. The load models used by Jacob et.al. differ slightly from those described in the previous paragraphs by the fact that he uses a localised pressure load. The equations he used to calculate the pressure load was also used in this thesis and is presented in section 6.3.1. The main difference between the localised loads used by Jacob et.al. and the evenly distributed pressure load models previously described, is the addition of a formula to calculate the burn diameter, which is the localised area over which the blast pressure is assumed to act. Jacob et.al. also compares their FEA and experimental data using the Nurick dimensionless number and the deflection-thickness ratio. The numerical and experimental data presented shows good correlation with each other and the least squares fit determined by Nurick (1989), proving the applicability of the load model used.

As previously said, BISRU has much experience in thin circular plate bulge tests and a significant amount of experimental data on this type of test is available. In the bulge test a thin metal plate would be mounted between two 20 mm thick clamp plates as shown in Figure 2.5. Both of the clamp plates have a 100 mm diameter hole that would define the unsupported area of the specimen. A high explosive charge would then be mounted on a thin, 100 mm diameter disk of polystyrene foam which would fit snugly in one of the holes in the clamp plate. Upon detonation of the explosive the thin plate would be loaded by a gas pressure pulse and deform, a process that usually takes less than 200 μs.

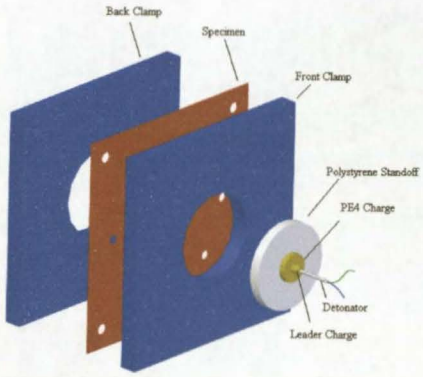

Figure 2.5: A thin plate bulge test specimen setup for a circular specimen.

A series of FE analyses was done for this thesis, simulating this type of test. The aim of the analyses was to confirm correct modelling procedure and to gain experience, since this type of transient dynamic modelling was necessary for simulating the structural response of the new impulse meter. The bulge test simulation would give two metrics which could be compared to experimental data, midpoint deflection and the deflected profile.

A separate goal of this analysis was to confirm the fact that the inertia of the clamp structure played no role in the deflected profile of the specimen. This meant that a rigidly clamped specimen, in which the clamped edge was constrained to prevent any motion, would have the same deflected profile as a clamp that was free to be blown away.

A quarter symmetry model of an 89 mm square specimen, shown in Figure 2.6, was built using 45 000 eight-node hexahedral elements. The model included a strain rate dependent material model as well as a model to simulate the contact and friction between the clamp and the specimen.

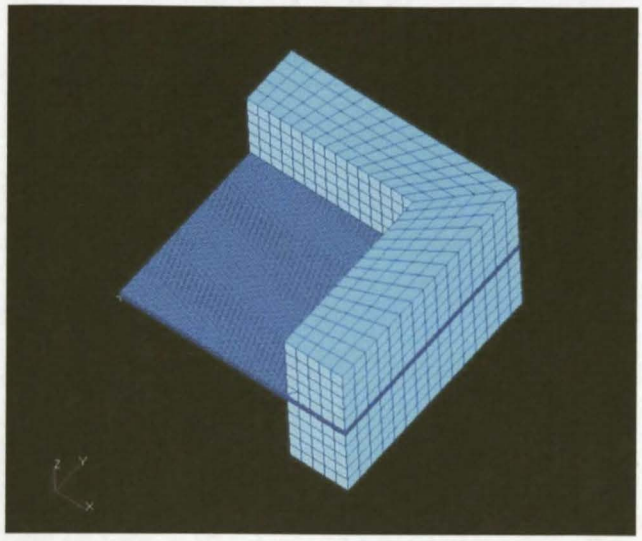

Figure 2.6: A quarter symmetry FEA model of a squarer plate specimen and clamp used in thin plate bulge tests.

The specimen was uniformly loaded on the lower face with a square (versus time) pressure pulse of 15 μs duration, similar tot that shown in Figure 2.7. The pressure pulse was sized by considering the required impulse, the blast loaded surface and the pulse duration, in a manner similar to Olson et.al. (1993).

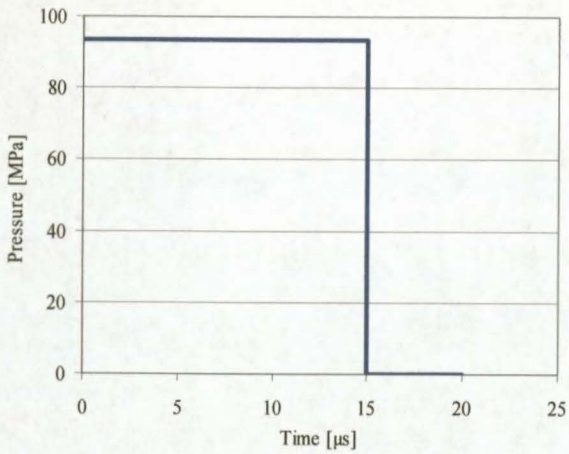

Figure 2.7 A typical pressure pulse for a 14 N·s Impulse.

Clamping force due to a set of clamping bolts was simulated using an evenly distributed constant pressure applied to the upper and lower exposed faces of the clamp plates. The inertia of the clamp sandwich support structure was changed by adding a point mass element and varying the mass of that element for the different simulations. Two extreme

cases were also modelled. One where the edges of the clamp was rigidly fixed, simulating infinite inertia and the other where the clamp sandwich was totally unconstrained, simulating the absolute minimum inertia.

The results of the FEA simulations are shown in the figures that follow. Figure 2.8 shows that the deflection history of the specimen midpoint relative to the clamp sandwich is unaffected by the mass of the clamp sandwich and its support structure. The deflected shapes from various simulations are compared with a profile obtained experimentally by Olson et.al. in Figure 2.9, once again, there is no sign that the mass of the clamp sandwich (and its support structure) has any effect on the response of the specimen.

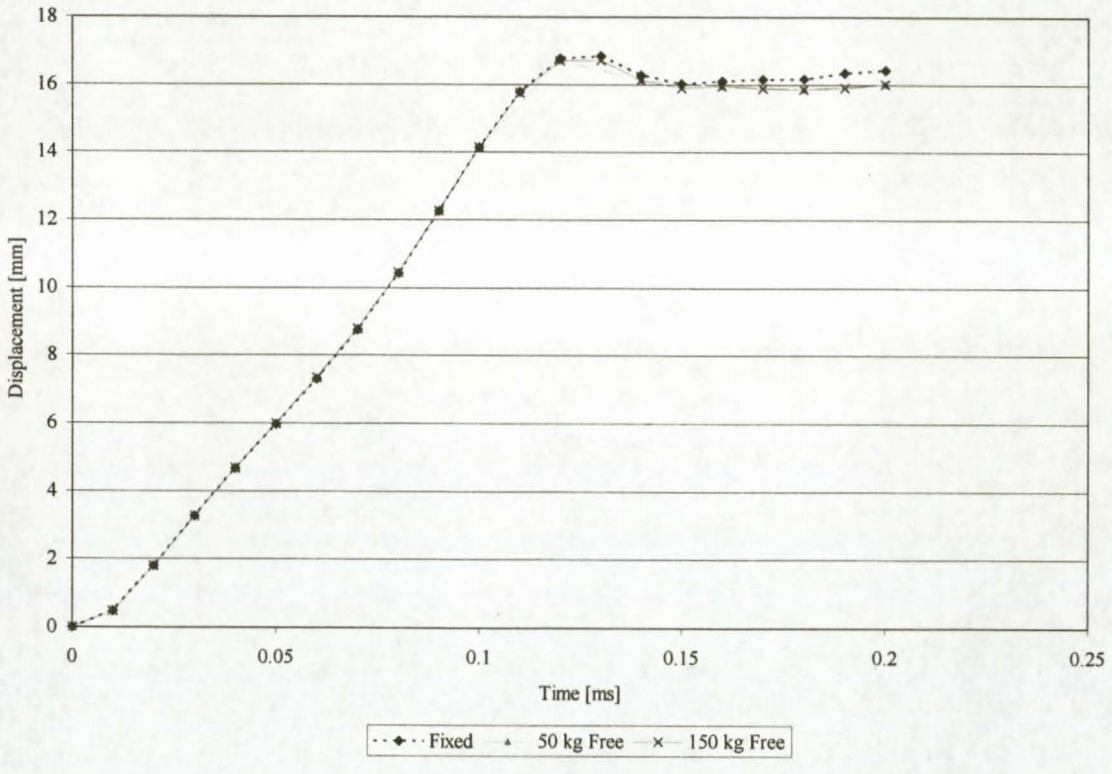

Figure 2.8: The time-deflection graph from three simulations (45 000 nodes) using identical specimens, but different clamp support masses.

Given that the data presented in Figure 2.9 is for a 1.6 mm plate thickness, it is reasonable to declare the results acceptable since the simulated profile is within 1 deflection-thickness of the experimental profile.

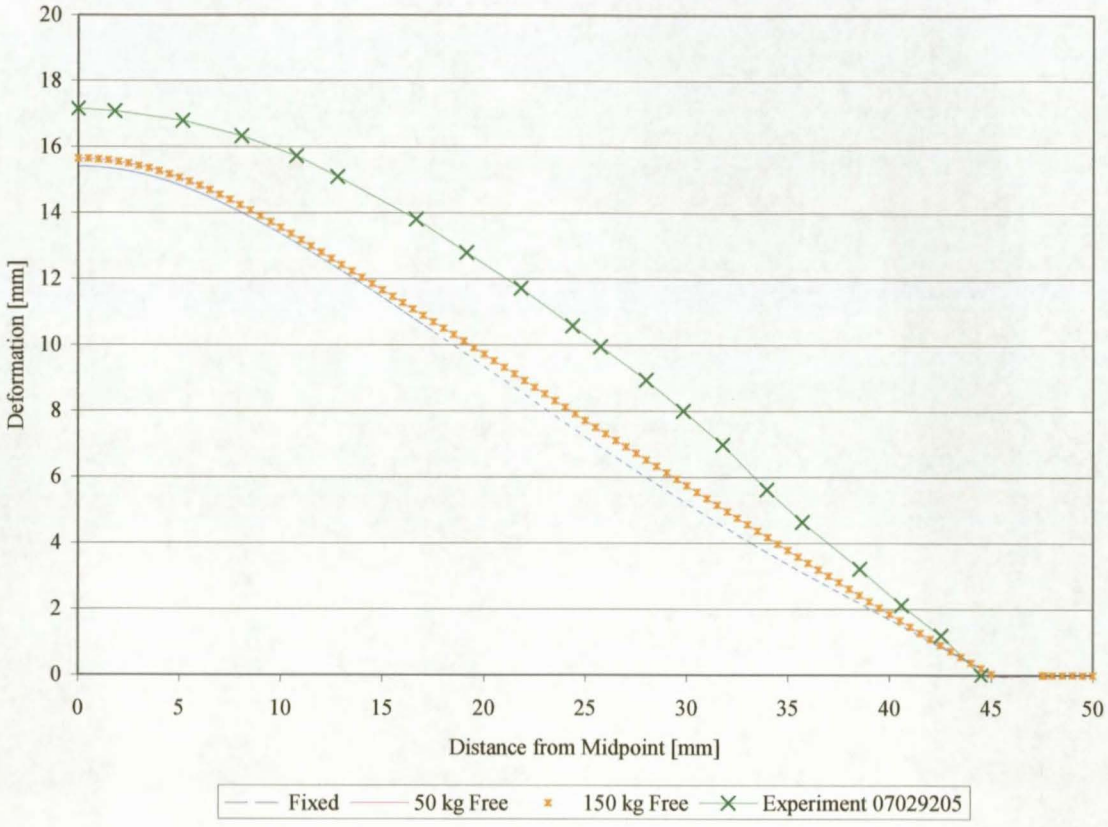

Figure 2.9: Simulated vs. experimental results for a 14.2 N·s load case.

3. Concepts

Various concepts were explored in the preliminary design phase. Most of these concepts were aimed at exploiting the known impulse responses of simple systems. This chapter explains the concepts.

3.1. Cantilever beam

Rod and heavy target mass type ballistic pendulums have been used by the U.S. Army Ballistic Research Laboratories and their subcontractors, with excellent results. (Drotleff et.al., 1996) The cantilever beam impulse meter, as shown in Figure 3.1, is a rod and heavy target mass type of ballistic pendulum, with the rod parallel instead of perpendicular to the ground. An impulse, parallel, but opposite to the gravity vector may then be applied to a test specimen mounted on the target mass, changing the beam's momentum and velocity.

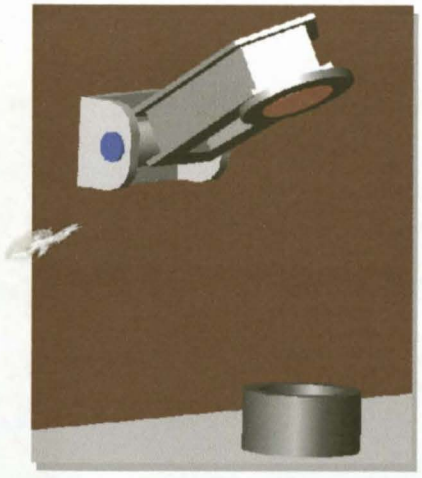

Figure 3.1: An impression of a cantilever beam impulse meter.

Being a rotational system, the linear momentum due to the applied impulse will be converted to angular momentum, causing the cantilever to rotate about its pivot. This angular momentum is lost during the upward motion as the cantilever beam's kinetic energy is converted to gravitational potential energy. If the cantilever was initially at rest the maximum angular deflection can be used to calculate the initial velocity of the target mass. Cantilever beams can be difficult to implement since the beam has to be

very stiff and light to ensure that the impulse response of the beam does not influence deflection measurements. The pivot used in this type of system also needs to be carefully designed in order to void friction problems.

3.2. Ballistic projectile

A ballistic projectile is a simple target mass suspended by a light cable, with a test specimen mounted on the target mass. The impulse is applied to the test specimen, changing the linear momentum and velocity of the target mass. If the impulse vector is parallel and opposite to gravity and acts through the COG of the mass, it will move upward and its kinetic energy will be converted to gravitational potential energy. Thus the maximum deflection can be directly related to the velocity change of the target mass and the applied impulse, if the target mass was initially at rest. Stability of the target mass during upward travel may cause concern at higher impulse levels since the impulse has to act very accurately through its COG.

The ballistic projectile is ideally suited to measure large impulses since its impulse response has a second order relationship between deflection and impulse. This means that impulse measurement accuracy improves dramatically with impulse magnitude. The impulse response of the ballistic projectile can easily be adjusted by changing the mass of the target mass.

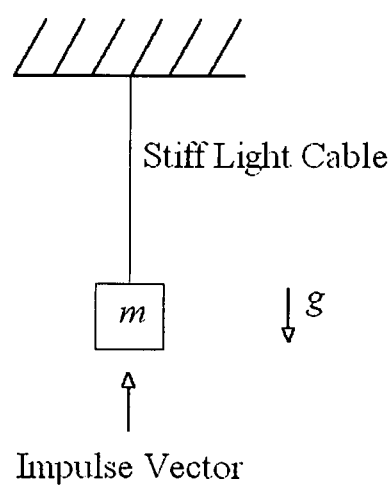

Figure 3.2: A ballistic mass suspended by a light tether.

3.3. 1-DOF spring mass system

The single degree of freedom spring mass concept is similar to the ballistic projectile in that the impulse is applied to a specimen mounted on a suspended target mass. A spring suspension is used in stead of a cable suspension thus converting kinetic energy to a change in the elastic potential energy of the spring, which is always kept in tension. The spring mass has a linear relationship between applied impulse and the vertical deflection and the impulse response of this system can easily be modified by increasing the mass of the target mass or the stiffness of the suspension spring.

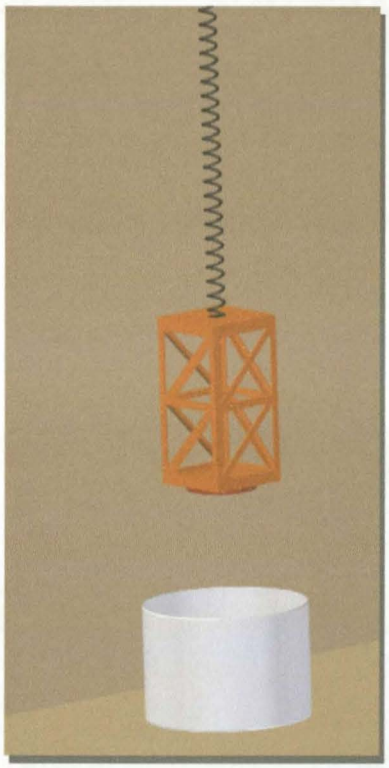

Figure 3.3: An impression of a constrained spring mass impulse meter.

3.4. Constrained ballistic projectile

A constrained ballistic projectile is similar to a ballistic projectile with the exception that it is constrained to move only in the vertical direction. This may be for stability or for safety reasons. The constraining structure used must be carefully designed to ensure consistent friction losses.

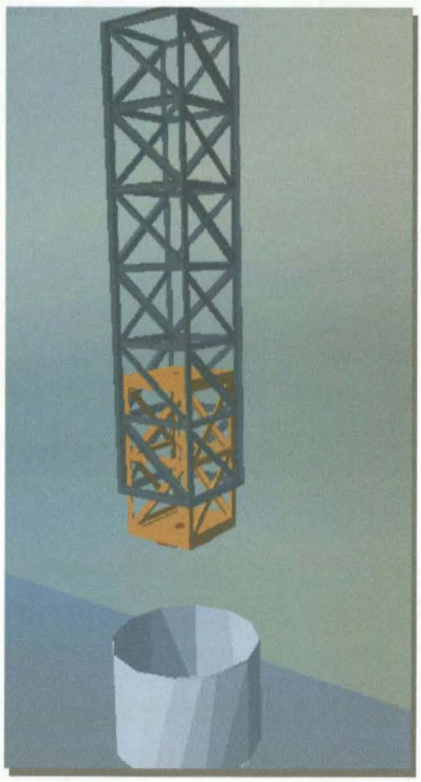

Figure 3.4: An impression of a constrained ballistic projectile impulse meter.

3.5. Direct motion measurement

Direct motion measurement can best be applied using high speed digital cameras. Using camera pairs or a mirror setup enables the time-displacement history of almost any point on the test specimen to be recorded. The digital photographs may then be analysed using special software to calculate the velocity of any point on the surface of the test specimen. Optical recording techniques have the disadvantage of smoke and dust obscuration (necessitating flash x-ray techniques) and multi camera systems are notoriously difficult to synchronize.

Direct motion measurement can also be applied using an accelerometer. The acceleration data may be integrated to yield the velocity, or analysed to estimate the applied force necessary to cause the measured acceleration. System dynamics makes it very difficult to estimate the force applied to the system, while the successful integration of acceleration data is extremely difficult.

3.6. Force measurement

Force measurement with load cells can be used to measure the forces acting on a test specimen. Impulse may be calculated by integrating the force history. This method is potentially very accurate, but is also very dependent on the system dynamics. With this measurement system it would be very important to have very fast data capturing equipment in order to accurately capture the peak forces.

4. Specification Development

Due to the unique nature of a device for the measurement of vertical impulses it was very difficult to form a set of specifications; the only fixed parameters were the ability to operate inside the available 6.5 m high, 3.5 m long and wide test cell with a 75 g PE4 rating.

It was also envisaged that the new device be able to perform the in-house standard bulge tests on 244 mm × 244 mm plates with a 100 mm loaded diameter. This would aid in the test development and calibration.

Due to a lack of data on the momentum transfer between buried charges and test specimens with a small standoff distance, the expected maximum impulse could not be determined. Therefore a decision was made to design for an arbitrary maximum impulse of 100 N·s.

Apart from the set of fixed quantitative design parameters that limits the size and impulse rating, a set of qualitative specifications was also formed to effectively compare the performance of different concepts.

Constant energy absorption characteristics were considered important; in order to ensure that test results are repeatable, energy losses in any of the measurement systems must be predictable and preferably small.

The measurement device should also have good impulse resolution, preferably less than 0.5 N·s for most tests.

Needless to say, the measurement system would be exposed to the harsh environment inside an active blast chamber, and thus needed to be simple, robust and cheap.

The new measurement device will be needed for various experiments of different types and charge sizes, necessitating a wide measurement range and the ability to easily make modifications.

Simplicity was another important parameter forced by the innovative and complex nature of this device. Simpler systems are usually easier to troubleshoot, improving the chances of success.

Each of the qualitative parameters was compared relative to the other parameters to determine their importance in ensuring a good design. Table 4.1 shows the scores and relative importance of the qualitative parameters. The scoring system may be described as follows:

1. The parameter is less important than the one to which it is compared.
2. The parameter is equally important as the one to which it is compared.
3. The parameter is more important than the one to which it is compared.

For example, constant energy absorption characteristics are one of the most important characteristics sought from this system, since it ensures test repeatability. Good measurement resolution is of little value if the measurement repeatability is worse than the resolution. Therefore constant energy absorption characteristics were deemed more important than most any other characteristic.

Table 4.1: Qualitative design parameter importance rating.

Parameter	1	2	3	4	5	6	7
1. Constant Energy Absorption Characteristics		2	1	1	1	1	1
2. Good Measurement Resolution	3		1	1	2	1	1
3. Low Friction	3	3		1	2	1	1
4. Low Cost	3	3	2		3	2	1
5. Wide Measurement Range	3	2	2	1		1	1
6. Ease of Modification	3	2	3	2	2		1
7. Robustness & Simplicity	3	2	3	2	1	2	
Score	18	14	12	8	11	8	6
Importance [%]	23.4	18.2	15.6	10.4	14.3	10.4	7.8

5. Concept Evaluation

Each of the concepts was evaluated in Table 5.1 on a scale of one (poor) to three (excellent), to see how well they satisfy each of the qualitative design parameters. By multiplying these scores with the importance of each of the qualitative parameters it could be established how well a concept would perform in satisfying all the qualitative design parameters. The concept scores were normalised to that of the winning concept to establish an order of preference.

Table 5.1: Concept evaluation against the qualitative design parameters.

	Relative Value [%]	Ballistic Projectile	Tower Trolley (Constrained Projectile)	Swing Arm	Spring Mass	Direct Motion Measurement	Force Measurement
Constant Friction Characteristics	23.4	3	1	1	3	3	3
Good Measurement Resolution	18.2	2	2	2	3	2	2
Low Friction	15.6	3	1	1	3	3	3
Low Cost	10.4	3	2	3	3	1	1
Wide Measurement Range	14.3	3	3	3	3	3	3
Ease of Modification	10.4	3	2	2	3	3	3
Robust & Simplicity	7.8	3	2	2	3	1	1
Score	100	282	175	186	300	245	245
Normalised Score		0.94	0.58	0.62	1.00	0.82	0.82

By using Table 5.1, it was possible to prove that the spring mass concept was the best option to pursue and that the ballistic projectile was the second most likely concept to guarantee success within the given parameters. The spring mass concept did very well in satisfying the most important design parameters, since it has minimal friction losses and no bearings or guides that can cause varying friction losses. Its simplicity and low cost also made it much more attractive than the direct and force measurement methods. Therefore the decision was made to pursue the design of the spring mass concept.

6. Detail Design

When an explosion takes place the resulting pressure wave grows radially, thus the pressure associated with the blast front reduces with the square of the distance from the centre of the blast. The SMI configuration was based on this fact. All of the sensitive parts of the device like the suspension spring and displacement recorder were positioned as far away as possible from the blast to ensure their reliable and accurate operation. Modularity was promoted by creating an interface that could easily be modified to accept any clamping jig. The end result of the detail design process is shown in Figure 6.1.

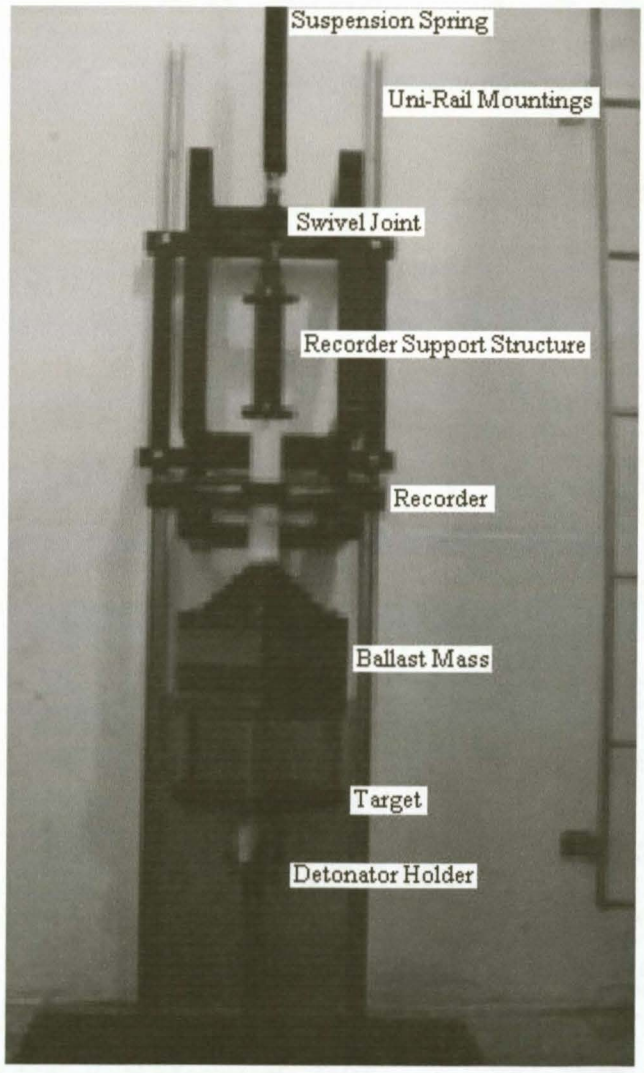

Figure 6.1: The completed SMI system.

The main components of the SMI are:

1. *The target mass*

The target mass assembly shown in Figure 6.2 represents more than 90% of the SMI's moving mass. It includes the test specimen, the necessary clamping structure that contains the bulge test specimen and the target base which may be modified to accept other test specimen geometries. In tests where very large or small impulses are applied to a test specimen, the response of the SMI may be optimised by changing the mass and rigidity of the target base with the addition and removal of ballast mass plates.

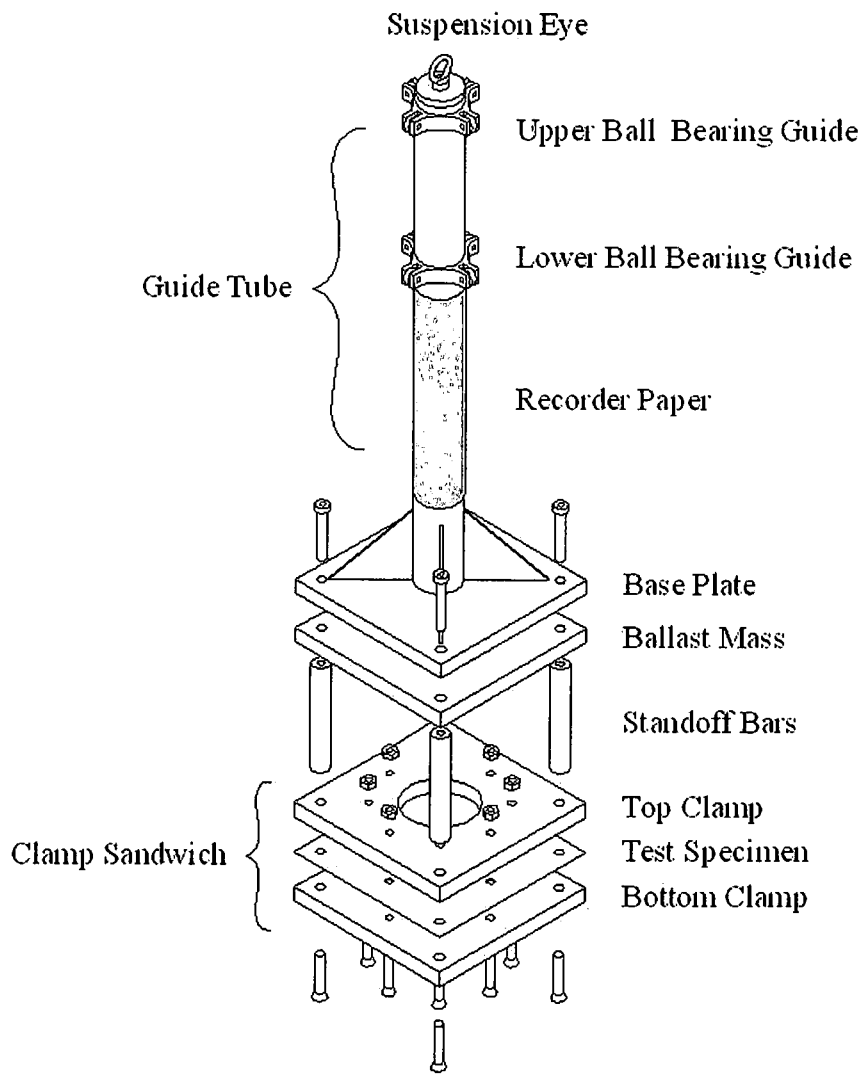

Figure 6.2: The target mass assembly.

The upper part of the target base is formed by the guide tube which serves to increase the distance between the blast and the suspension spring. The guide tube also has two sets of ball bearing guides that may be used to guide its travel if the guide tube is placed inside a cylindrical support tube. Soon after the SMI was built and tested it was found that the ball bearing guides were unnecessary and a support tube concept was not used again. The bottom part of the guide tube accepts an A4 sized piece of paper for recording the SMI deflection.

The base plate, which forms the basis of the target mass, is of prime importance to the design as it must allow a wide range of specimens and jigs to be fixed to the target mass. It was decided to use a flat surface made from a 20 mm thick steel plate. This means that almost any test specimen can be mounted using standoff bars and relatively simple adapter plates.

2. *Suspension spring*

The suspension spring is the most important component of this system as it converts the momentum of the target mass to potential energy. A tension spring was chosen for this purpose due to its ease of manufacture and the fact that spring buckling would be very improbable. A very important factor in the design of the spring was to ensure that it will be as light as possible to maintain the assumption of a massless spring. Despite this, calculations were corrected to better predict the response of a 1-DOF system with a heavy spring. It is also essential that the spring operates in its linear force-deflection region; this is generally achieved by designing a low stiffness spring with a large amount of travel and using only the central 75% of the total extension range. A set of three springs were designed to allow impulse measurement up to 75 N·s. All three of the springs were tested for preload, stiffness and linearity prior to use. The results of those tests are presented in Appendix E and should be of future use in monitoring the condition of the springs and for possible replacement purposes.

It was decided that the peak deflection be limited to an amplitude of 100 mm in order to allow the use of A4 sized recorder paper. A peak amplitude of 100 mm meant that the spring must be able to extend more than 267 mm without yielding, even though only 200 mm extension is required, to ensure a linear spring coefficient in the operating zone.

$$267 \approx \frac{2 \times 100}{0.75} \text{ [mm]} \qquad \textbf{Equation 6.1}$$

A series of impulse response simulations were performed where the target mass, spring stiffness and applied impulse were varied to keep the deflection amplitude below 100 mm amplitude. The minimum mass estimates for these simulations were obtained from the CAD solid models. More detail about the impulse response simulations is presented in Section 6.5 and further particulars regarding the spring design and testing are presented in Appendix E.

3. Swivel joint

A swivel joint was also included in the suspension design, between the spring and the suspension cable, in order to decouple the suspension cable from the coupled extension-rotation behaviour that is associated with tension springs. Rotational decoupling is necessary to keep the suspension cable from winding up and down. When a cable is wound up or down, its length changes, causing spurious vertical motion of the target mass and measurement errors.

The swivel joint shown in Figure 6.3 was placed in the wrong position, it is very important to realise that all the loosely connected masses between the target mass and the suspension spring add to the inertia of the spring and not that of the target mass. This negates all the efforts to design mass optimised springs and seriously detracts from the accuracy of the massless spring assumption. Unfortunately this was only realised after the initial tests, and the data had to be corrected using the method presented in Appendix B. The correct position for the swivel joint is above the suspension spring.

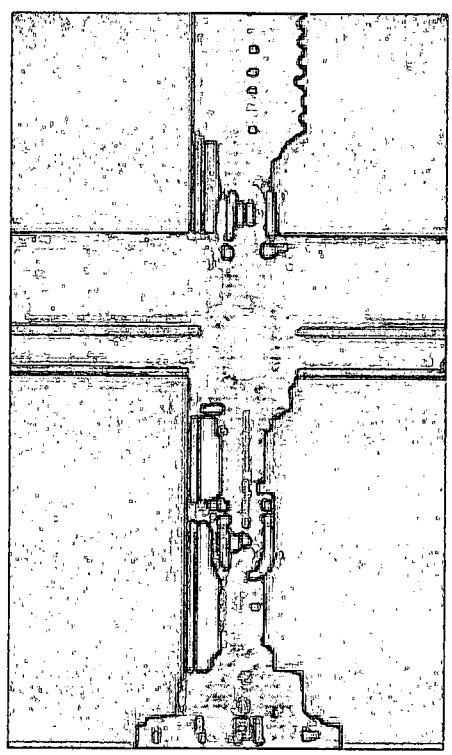

Figure 6.3: The swivel joint.

Suspension support

The suspension support took the form of an overhead beam that was bolted to the walls, 6 m above the floor of the blast cell. The overhead beam was designed to be able to carry a 1000 kg static load with a safety factor of 3.2 on yield stress. An adjustable saddle clamp was designed to fit on the overhead beam, so that the distance between the target mass and the wall could easily be adjusted. The installed suspension support is shown in Figure 6.4.

Figure 6.4: The overhead suspension support showing the saddle clamp and suspension cable.

4. Deflection recorder

Various recorder concepts were investigated, ranging from LVDT systems to optical methods using LEDs and photo-diodes. The deflection recorder design was eventually based on the pen and paper recorders successfully used by BISRU in its horizontal ballistic pendulums. This simple recorder has the advantage that it is cheap and robust while being insensitive to the electrical noise generated by detonators. It was decided to use a set of four spring-loaded pens arranged radially about the guide tube, around which the A4-sized recording paper is wrapped. Four equi-spaced pens pressing on a tube also tends to centre and stabilise the tube during travel.

Having multiple pens also serve as redundant systems so that at least one peak deflection recording is almost guaranteed in the event that one or more of the pens lose contact with the recording paper. The recorder range was based on the size of an A4 sheet of paper, which allows a total movement of at least 200 mm. Examples of deflection recordings obtained during testing are presented in Appendix D.
Figure 6.5 shows the successful recorder design.

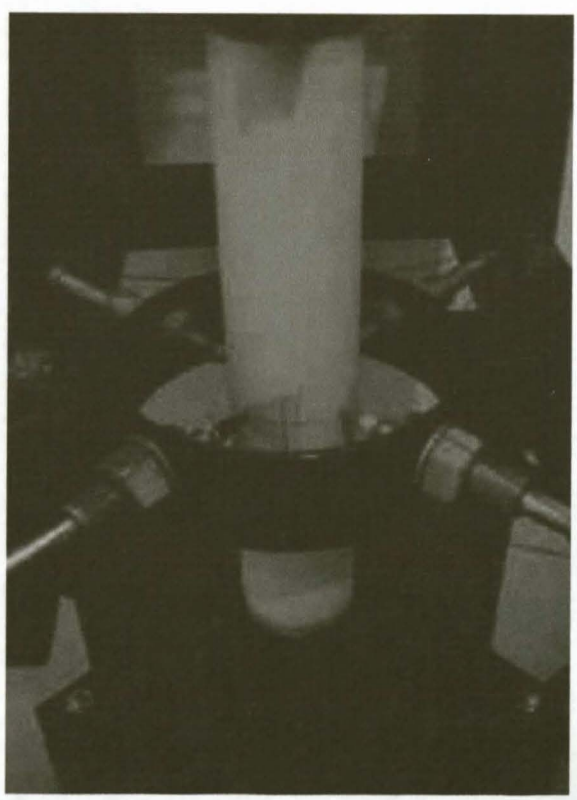

Figure 6.5: A view of the final recorder.

5. Recorder support

The recorder support system was designed to be adjustable since the standoff distance would be one of the main variables while testing with buried charges. The recorder support system shown in Figure 6.6 is fixed to a set of wall mounted rails which allow the support to be positioned up to 1.4 m above the floor. A simple FEM model consisting of beam elements was used to assess the strength and stiffness of the structure. A simulation was also run to ensure that the first modes of vibration of the recorder support system were high enough to have little effect on the recorder measurements.

The support structure was designed so that the system would survive a minor impact of the target mass at low velocity. It was also designed to be strong enough to support a static vertical load of 1200 N without failure.

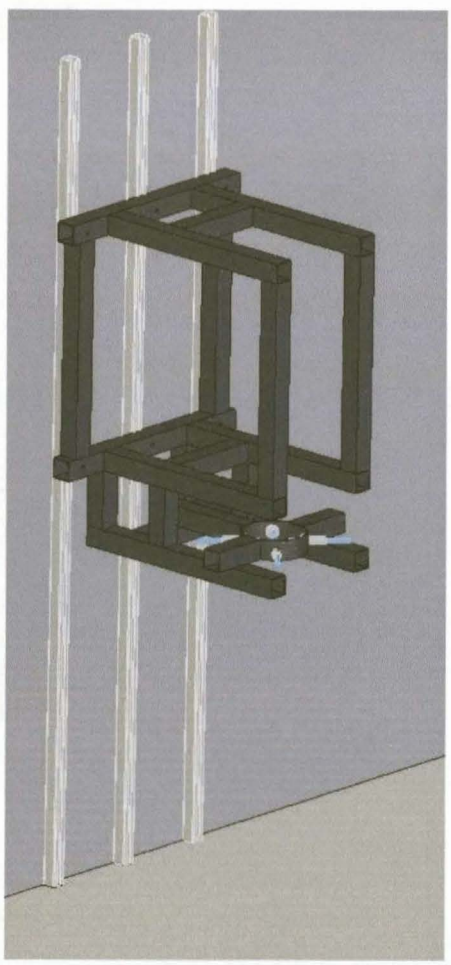

Figure 6.6: The recorder support, showing the recorder and wall mounted guide rails.

6. *Arrestor*

When doing experiments using buried charges the shape and size of crater formed by the blast is of great interest, this makes it necessary to design an arrestor that will stop the downward moving target mass from impacting the soil and destroying the crater. There are two design strategies for an arrestor. The first strategy would be to arrest the moving target mass as soon as possible after it attains peak height using a braking mechanism.

An alternative strategy would be to stop the mass a few millimetres below the equilibrium position at which the impulse was applied, using a stiff tension spring with stiffness $k_{arrestor}$, in parallel with the suspension spring. A schematic of a spring based arrestor system is presented in Figure 6.7. The dedicated cable from which the arrestor spring is suspended would be set up to be slack while the target mass is at or above the system equilibrium position. Thus the upward travel of the target mass and its peak deflection recording will be unaffected by the arrestor system.

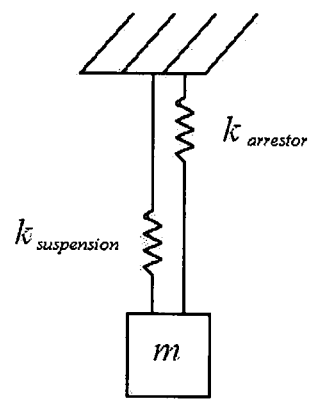

Figure 6.7: A diagram of the spring based arrestor system.

The friction brake system would be too intricate, requiring a fast reliable response time, which could be varied according to the expected target mass travel and standoff distance. That degree of sophistication was considered unreliable given the harsh post-blast environment within the blast cell.

It was decided that a spring arrestor system would be the most likely to achieve success given the time, robustness and budget requirements. A spring arrestor would impose a minimum standoff distance, but would be very cheap and simple to employ. A braking system design requires a number of moving parts that would greatly increase both the operational hazards and failure modes associated with the use of the system. The spring arrestor system was designed to be able to arrest the falling target mass within 30 mm to 50 mm below its equilibrium height, depending on the mass of the target mass and the applied impulse.

Analyses showed that an arrestor spring with a stiffness of 140 000 N/m is sufficient to stop the 80 kg target mass falling from a peak height of 80 mm within 36 mm while applying a peak force of 5 kN on the overhead beam. The overhead beam from which the impulse meter is suspended was designed for a maximum load of 500 kg (static) with a safety factor of six on yielding.

Details of the arrestor spring are presented in Appendix E, Table E.3.

6.1. Design procedure

The design of the various SMI components was done in a very specific order to ensure that the minimum number of design iterations were necessary.

1. Identify the most common type of test and the test specimen associated with the test of interest.
2. Decide on the maximum impulse magnitude that will be applied.
3. The next step is to decide on the maximum amplitude of SMI movement.
4. Based on the choices made in steps 1 to 3, CAD and FEA assisted design is done to ensure a suitable target mass. The main design drivers at this stage are to ensure that the target mass is as light as possible, stable in flight and strong enough to survive the blast loads. The mass of the target mass has a great influence on the frequency of the SMI response and its sensitivity. This step also requires the design of the recorder and supporting structure.
5. Once the minimum mass of the target mass, maximum applied impulse and allowable deflection are fixed, enough design data is available to design a spring. The spring design is driven by low mass, low stiffness, linearity and the ability to survive large extension.

   Parallel with the suspension spring design is that of the arrestor system.

6.2. CAD design

A set of CAD solid models were constructed to determine the form and fit of the various components of the impulse meter. Assemblies of the components are shown in Figure 6.8 and Figure 6.9. The geometric design of the target mass was focussed on creating a low COG to ensure stability and to reduce the risk of buckling and high stresses due to the inertia of the upper parts of the target mass.

The target mass was designed to have a stiff heavy base, as close to the blast source as possible. This design strategy put the stiff part of the structure where it is most needed with the added benefit that the final velocity of the heavy base would be lower than that of a lighter base for a similar impulse. The lower parts of the target mass were intended to absorb the momentum imparted by the impulse, so that the impulse seen by the upper more fragile parts of the structure is much lower than that seen by the specimen. The base was also designed to shield the upper parts, and especially the recorder from the blast.

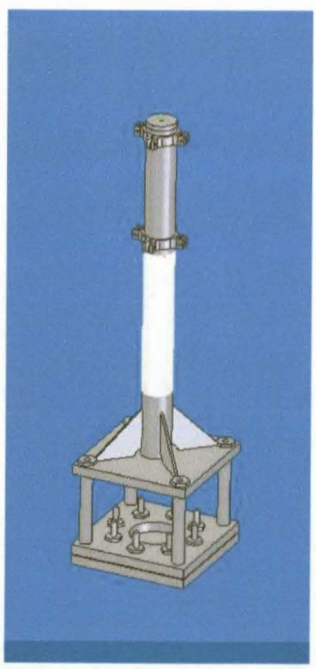

Figure 6.8: A conceptual design of the target mass and the clamp sandwich.

The upper part of the target mass was made of a long thick-walled tube that would act as a platform for a guide mechanism and to increase the moment of inertia about the non-axial-symmetric axes. The guide mechanism consisted of two sets of four ball bearings that were mounted on the upper part of the guide tube, as shown in Figure 6.2. These bearings would just clear a concentric guide tube around them and would only contact the guide tube in case of a skew shot and then with the minimum of friction. Early SMI tests showed that these guide bearings were unnecessary, since the system was sufficiently stable.

In order to make the recorder as robust as possible, a set of four stationary spring-loaded recording pens were used with the recording paper taped to the guide tube. After each test the recorder pens are disengaged and the recording paper is removed for inspection and replaced with a clean sheet.

Four pens were chosen to improve the redundancy of the measurements, to balance the contact force of opposing pens and to better quantify the tilt in the system at maximum deflection. A balanced set of four pens will also acts as a guide for the target mass.

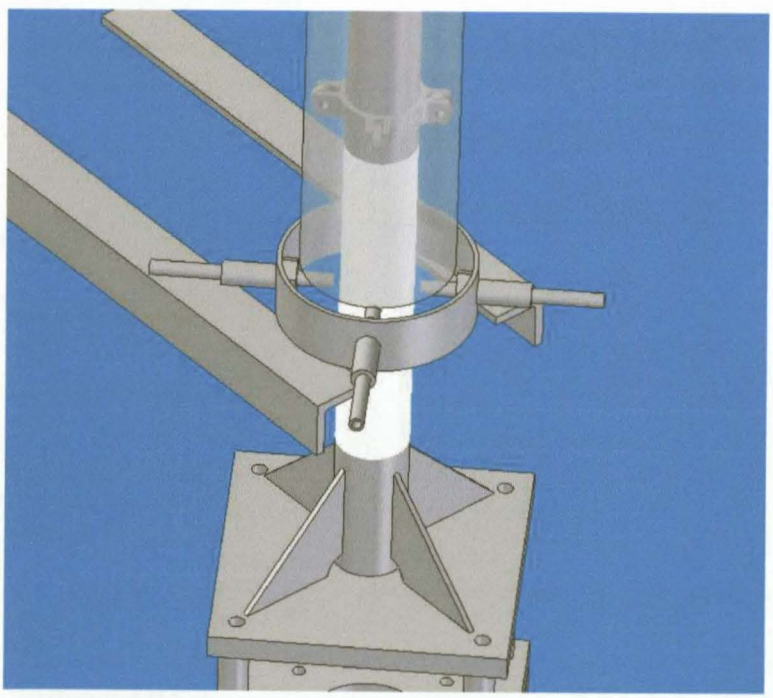

Figure 6.9: A close-up view of the recorder concept.

6.3. FEM analysis

Due to the non–linear behaviour of steel at high strain rates and the large deformations associated with blast loading, it was necessary to analyse most of the FEM models using a non-linear FE solver. The target mass was modelled with MSC.Patran and analysed using MSC.Dytran.

MSC.Dytran User's Guide (2005) states that MSC.Dytran is a three-dimensional explicit finite element code that specialises in the analysis of dynamic finite element problems which incorporates a high degree of material and geometric non-linearity.

The main concern in the design of the impulse meter was to ensure minimal yielding of the material from which the target mass is constructed. It was also necessary to ensure that the structure has a high axial stiffness so that the response of the target mass does not influence the recorded deflection. If the target mass and the support tube in particular, are seen as a set of linear springs of different stiffness in series, then it is easier to visualise that the out-of-phase vibration of these springs will make it difficult to relate the displacement of the top spring to that of the COG of the set.

One coarse meshed full model of the SMI25 (25 N·s impulse) module was built for a 25 N·s load case and two finely meshed quarter (using symmetry) FE models were built, one for the 25 N·s load case and the other for the 100 N·s load case. The analysis strategy was to assess the effect of mesh density by comparing the results of the coarse and finely meshed SMI25 models. The two fine meshed models served to explore the extremes of load cases and to verify that the SMI25 module structure would be the highest stressed since it has the smallest target mass, and consequently the thinnest target mass base plate. The thinner base plate reduces the plate's bending stiffness and consequently the stiff gussets that strengthen the support tube have to carry more of the bending load on the base plate.

6.3.1. The FEA model

Two FE model geometries of the target mass were created for the two load cases. The SMI25 model for the 25 N·s load case had a 20 mm thick base plate and no ballast mass as shown in Figure 6.10, The SMI100 model was identical except for the addition of ballast mass which effectively increased the base plate thickness to 120 mm.

The test specimen was modelled as a 40 mm mild steel plate mounted on 20 mm and 30 mm diameter standoff bars for the 25 N·s and 100 N·s load cases respectively. A "semi-rigid" test specimen was chosen to generalise the model for easier comparison and to reduce the analysis time while still ensuring a conservative model. A stiff plate would better represent the worst case scenario as it would transmit the impulse to the upper part of the structure without smearing it over time as a "very flexible" plate would. Therefore the period of the impulse seen by the upper parts of the structure would be a minimum, causing higher accelerations and higher inertial forces.

Figure 6.10: The SMI25 fine model.

Heat affected zones near welds were not modelled nor were the fillet welds themselves. The welded joints were modelled by shared nodes between welded parts. The bolted joints on the SMI were also not modelled and the different parts were connected by means of shared nodes. The use of shared nodes to simplify the modelling of bolted joints should be admissible since the highest loading seen by the structure is a

compressive force at the bolted interface. This type of loading only reduces bolt tension and thus has little effect on the bolts. Using non-linear spring elements and a contact model would be computationally expensive and several spring elements would be necessary to transfer bending moment from the stand off bar to the base plate of the target mass. Shared nodes between the standoff bar and base plate would give momentum transfer, albeit more severe than in reality and higher tensile stiffness to the joint at the cost of higher localised stresses and lower damping. Thus the model will still be conservative in estimating failure.

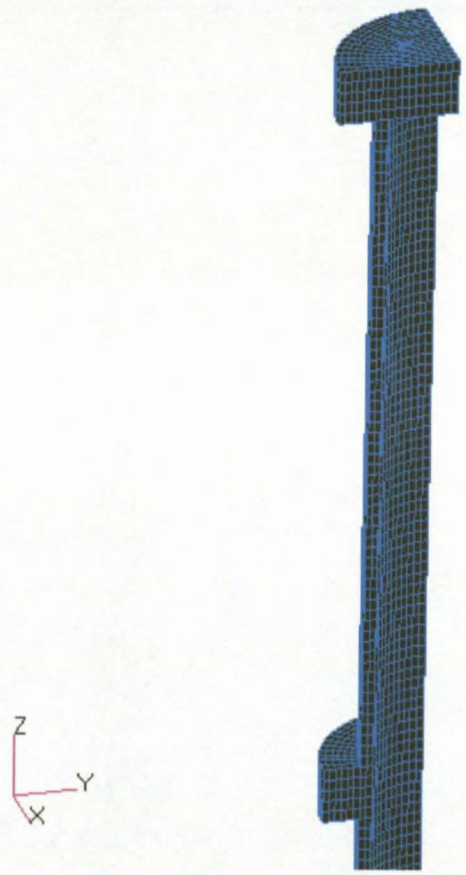

Figure 6.11: The mesh on the guide tube which is identical for both fine models.

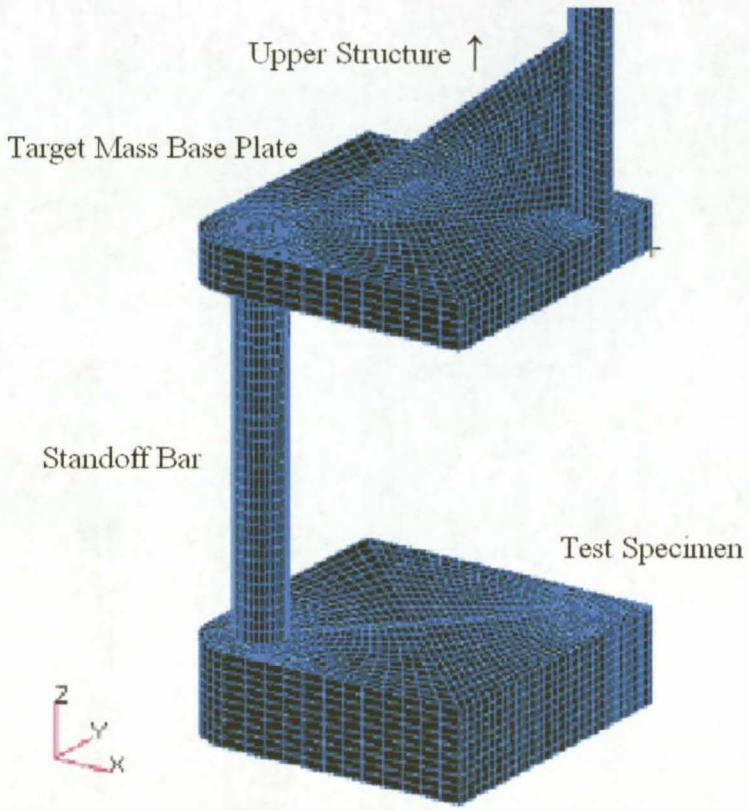

Figure 6.12: A close-up of the FEM quarter model of the SMI25 fine meshed test specimen and target mass. The simulated target had a mass of 35.44 kg.

The SMI was modelled using a consistent set of non-standard "impact form" SI units in order to improve mathematical conditioning of the problem since very small time steps, small lengths and very large pressures were involved. Table 6.1 shown below compares the impact form units to the standard SI units.

Table 6.1: A comparison of the standard SI units and the set of consistent, non-standard SI units used for FEA analyses.

Property	Basic units	Standard form	Impact form
Time	T	s	ms
Length	L	m	mm
Mass	M	kg	g
Temperature	Θ	K	K
Density	$M{\cdot}L^{-3}$	kg/m3	g/mm3
Force	$M{\cdot}L{\cdot}T^{-2}$	N	N
Pressure	$M{\cdot}L^{-1}{\cdot}T^{-2}$	Pa	MPa
Energy	$M{\cdot}L{\cdot}T^{-1}$	J	mJ

Elements

Most of the elements used were eight node hexahedral solid elements (35000 for SMI25, 40000 for SMI100), a small number of pentahedral elements were also necessary. The hexahedral and pentahedral elements used are the only solid elements available in Dytran apart from tetrahedral elements, the use of which is strongly discouraged by the Dytran manuals. All Dytran solid elements, like that of most explicit FE solvers, use only single point Gauss integration to reduce the computational effort. The effect of the resulting hourglass or zero-energy modes brought on by reduced integration was controlled through the use of the Flanagan-Belytschko Stiffness method which applies forces to reduce hourglass deformation. These basics of Gauss integration and the problems associated with reduced integration are discussed in most FEM textbooks such as Cook (1995).

Material properties

Since the SMI is constructed from mild steel it was modelled with Cowper-Symonds strain rate dependent yield strength to account for strain rate dependent yield strength, Jones (1989). The Cowper-Symonds relationship, which relates the dynamic yield stress σ_d at a specific strain rate $\dot{\varepsilon}$, to the static yield strength σ_0, given the material constants D and n, is shown in Equation 6.2. The DYMAT24 material model described in the MSC.Dytran Theory Manual (2005) was applied to all solid elements with the commonly accepted coefficients for mild steel as:

Table 6.2: Properties of mild steel. Chung Kim Yuen (2005), Callister (2000).

D	40	s^{-1}
n	5	-
σ_{YT0}	270	MPa
ε_{ULT}	0.3	
E	207	GN/m^2

$$\frac{\sigma_d}{\sigma_0} = 1 + \left(\frac{\dot{\varepsilon}}{D}\right)^n \qquad \textbf{Equation 6.2}$$

Material damping was not modelled. Given that the structure is very stiff and that its modal damping could not easily be measured it was decided not to model material damping. An undamped material model would predict stresses that are higher than in reality, ensuring a conservative model.

Boundary conditions

Symmetry boundary conditions were applied to the symmetry sides of the quarter symmetry model. The 25 N·s and 100 N·s loads applied to the models were chosen to show the structure's response at the extremities of its working envelope. The impulse due to the blast was modelled as a single square wave pressure pulse, similar to Figure 2.7. The magnitude of the impulse due to a pressure load P, which acts on a circular surface of diameter D, for a period of time τ may be calculated using Equation 6.3.

$$I = F\tau = \left(P\frac{\pi D^2}{4}\right)\tau \qquad \textbf{Equation 6.3}$$

A spatially even pressure load was applied to the bottom surface of the test specimen. Equation 6.4 was used to calculate the duration τ of the pressure pulse, based the charge geometry and the 7000 m/s burn velocity of PE4, Jacob et.al. (2004). A schematic of the charge geometry is shown in Figure 6.13.

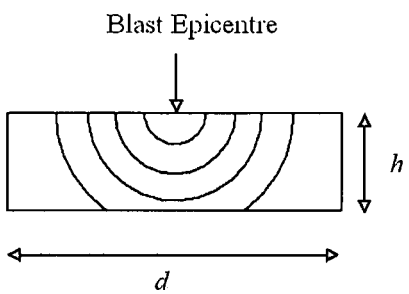

Figure 6.13: The hemispherical travel of a detonation wave from the epicentre of a right circular explosive charge.

$$\tau = \frac{\sqrt{(d/2)^2 + h^2}}{V_{burn}} \qquad \textbf{Equation 6.4}$$

Where d is the charge diameter, h the charge height and V_{burn} is the burn velocity of PE4.

The surface, on which the pressure load was applied, was taken as the burn diameter D, which can be empirically related to the charge geometry as reported by Chung Kim Yuen et.al. (2000) by:

$$\frac{d}{D} = (0.9h)^{0.3} \qquad \textbf{Equation 6.5}$$

The load pressure P was calculated from the calculated load area and the pulse duration by:

$$P = \left(\frac{I}{\tau \pi (D/2)^2} \right) \qquad \textbf{Equation 6.6}$$

No other boundary conditions were applied to the model. Gravity was ignored due to its negligible effect relative to that of the applied impulse over the small analysis time.

6.3.2. FEA results

Model checks

Dytran calculates its analysis time step size based on the Courant criterion, therefore the analysis will remain stable as long as the time step does not become increasingly smaller. None of the analyses presented in this thesis were reported to have stability problems by the Dytran Error Summary file.

A further check on the accuracy of results is to compare the hourglass energy with the total energy of the simulated structure. The forces used to control hourglassing dissipates energy, Dytran is able to output the amount of energy used to control hourglassing as "ENERGY-HRG". When a model becomes unstable due to the presence of large scale or wide spread hourglass instability, the fraction of the total energy dissipated in controlling hourglass deformation becomes considerable. Ideally the fraction of the total energy spent in controlling hourglassing should be zero, generally it is suggested that mesh refinement be considered if the hourglass energy becomes more than 10% of the total energy.

The coarse SMI25 model showed that more than 11% of the total energy was spent on controlling hourglass instability. Thus a finer mesh was used in modelling the SMI25 and SMI100 quarter models. The results of the analyses on the finer meshed models showed a drastic reduction in the energy expenditure on hourglass instability control. Both of the fine models spent less than 2% of their total energy on hourglass instability control.

The normal checks which include conservation of momentum and the conservation of the total energy were performed and all models satisfy these conditions. Information about the analysis results and the actual loads are presented in Table 6.3. The actual loads differed from the proposed loads due to the fact that loads were applied to groups of element faces which did not form a perfect burn diameter circle.

Table 6.3: The details of the FEA models.

Model	Proposed Load [N·s]	Actual Load [N·s]	Model Mass [kg]	FEM Z Momentum [N·s]	Average Velocity [m/s]	Hourglass Energy Magnitude [%]
SMI25 Coarse	25	32.5	36.5	32.5	0.89	11.5
SMI25 Fine	25	29.5	35.4	29.5	0.83	2.6
SMI100	100	98.4	76	98.4	1.29	1.02

The steady state response of the fine and coarsely meshed SMI25 models are compared in Figure 6.14 In order to effectively compare the dynamic response for the SMI25 models in Figure 6.14, it was necessary correct the displacement data for slight differences in the impulse applied to the two models. This was done by subtracting displacement due to the mean velocity, leaving only the displacement due to higher order dynamics.

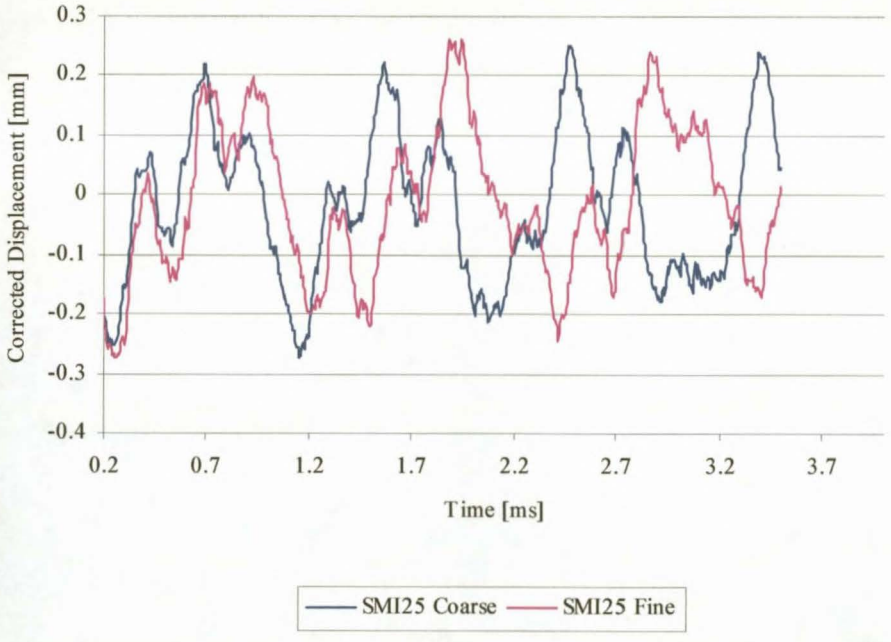

Figure 6.14: A comparison of the steady-velocity corrected displacement of the target masses of the SMI25 models.

As expected, the coarse model shows shorter period oscillations in its response due to the higher stiffness caused by large elements and the resulting hourglass control. The larger amplitude of the coarse model response can be attributed to the slight differences in mass and loads of the two models being compared.

After closer inspection it was found that the deformation difference was proportional to the momentum difference. Figure 6.15 shows how the amount of energy spent on hourglass control in the SMI25 coarse mesh model varies with time.

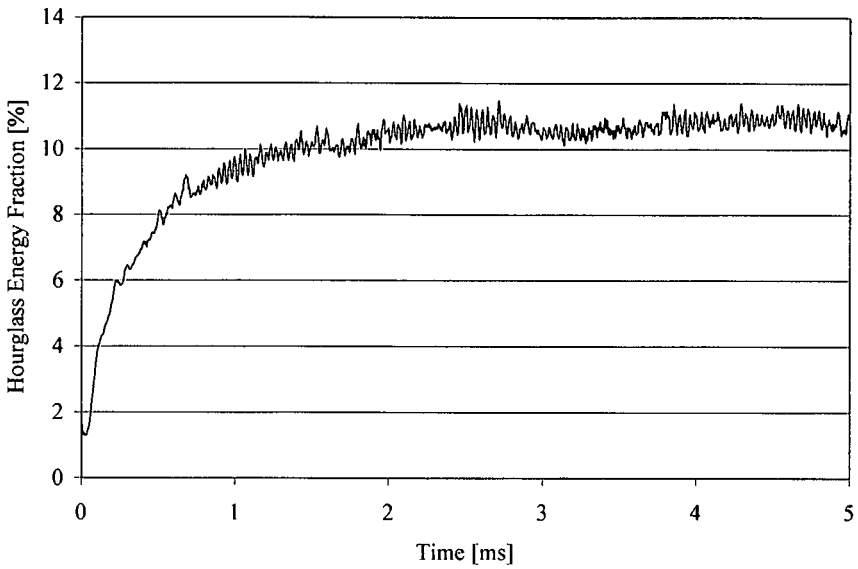

Figure 6.15: The growth of the hourglass instability for the SMI25 coarse model.

Plastic deformation

Figure 6.20 shows that the transient behaviour of the test specimen top surface midpoint, which includes plastic deformation, dies out after 500 μs, leaving only a steady state vibration superimposed on a constant velocity. Therefore the plastic deformation present at 500 μs is representative of the maximum deformation.

The results of the SMI25 fine model in Figure 6.16 and Figure 6.17 showed less than 2% plastic deformation resulting from a 29.5 N·s impulse while the coarse model presented in Figure 6.18 showed significantly less at 1.22% for a 32.5 N·s load. This discrepancy may in part be due to the large elements used in the coarse model and their tendency to spread the localised deformation over a much larger surface. However, it was noted from animated results of the FEA analyses that the position of peak plastic strain in both models was similar shortly after the application of the load. While the plastic strain had remained stagnant at the bottom surface of the test specimen in the coarse model, the finer meshed model showed it to slowly, compared to the initial strain rate, migrate closer to the centre of the thickness of the test specimen before stagnating there at 6 m·s. This observation coupled with the ability of the finer mesh to simulate higher order vibration modes points to the likelihood that the difference in response might have been caused by reflected shockwave effects that the coarse model could not predict. Unfortunately the investigation of this phenomenon fell outside of the scope of this project.

The plasticity predicted by these models was restricted to the test specimen and the standoff bars. Based on the small degree of the plastic deformation, and the fact that it is restricted to easily replaceable parts, the SMI25 design is considered fit for purpose.

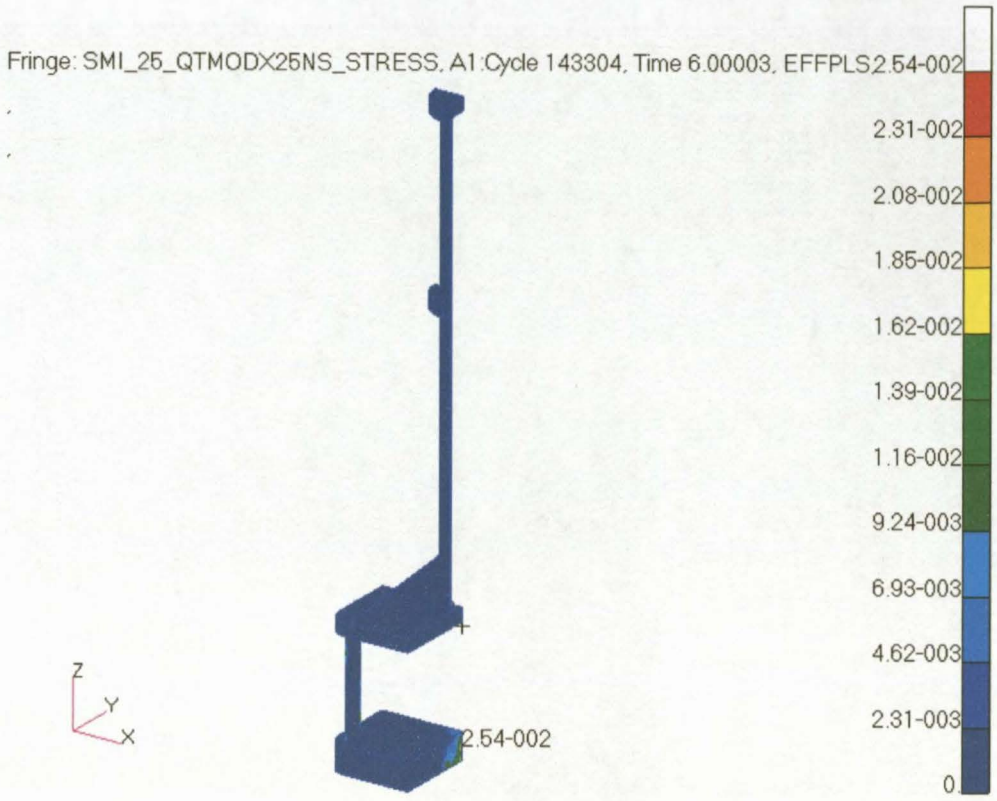

Figure 6.16: SMI25 fine mesh model, plastic strain after 6 ms.

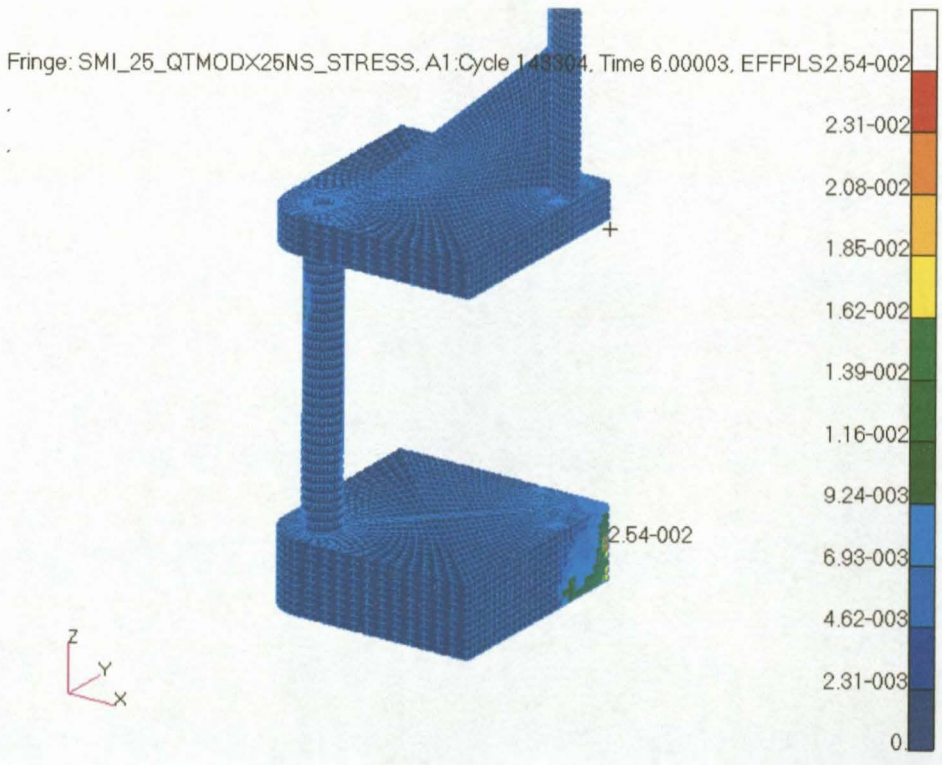

Figure 6.17: A close-up of Figure 6.16, 29.5 N·s load, 3.5 µs duration, 77 mm burn diameter.

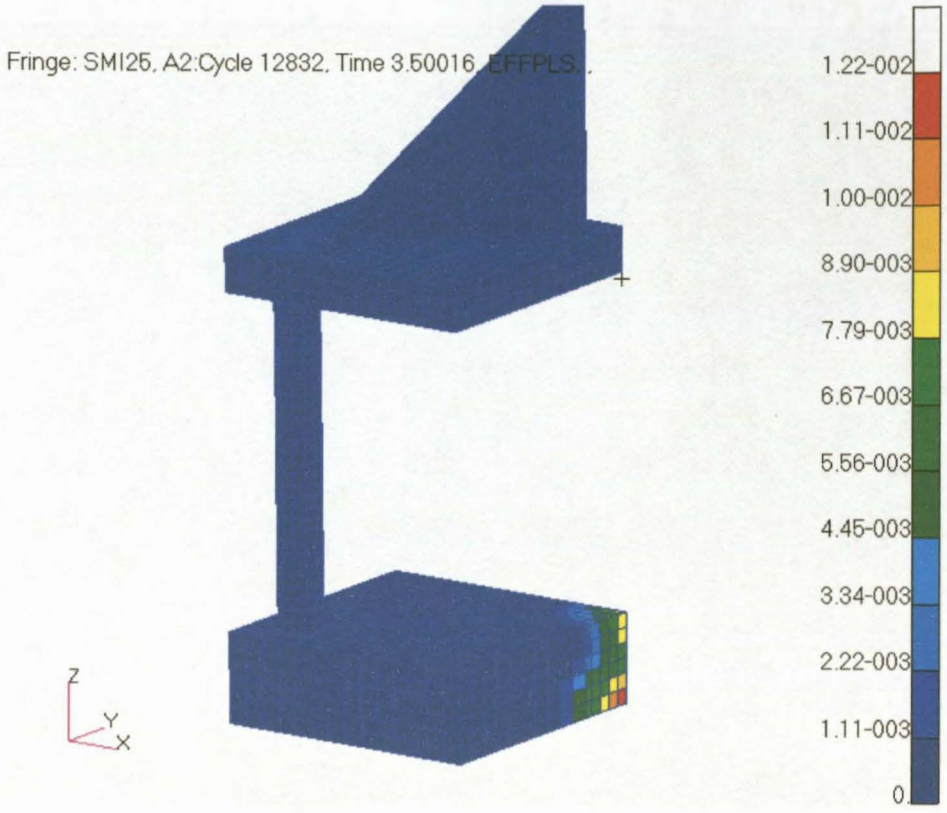

Figure 6.18: A section from the coarse mesh full model of the SMI 25 module. Plastic Strain after 3.5 ms, 25 N·s impulse, 3.5 µs duration, 77 mm burn diameter.

The SMI100 analysis results presented in Figure 6.19 shows no yielding in the upper part of the structure, but that localised plastic deformation did occur in the standoff bars and the test specimen. Two recommendations based on these analyses are that the test specimen should be considered sacrificial and that the standoff bars should be larger than 30 mm in diameter for high impulse tests.

During the early design phase it was decided to use the ballast mass as a momentum absorber to protect the upper parts of the target mass structure during high impulse tests. By changing the ballast mass it was possible to limit the velocity change of the target mass to less than 1 m/s. At low impulse this translates to a light target mass with a high amplitude response, while ballast mass must be added at higher impulse to reduce the initial velocity to 1 m/s. Increased ballast mass at high impulse also has the added benefit that it supports the base plate better, reducing the load on the gussets that strengthen the support tube.

This design philosophy was proved correct by these analyses since a fourfold increase in impulse did not cause buckling or significantly higher stresses in the upper structure.

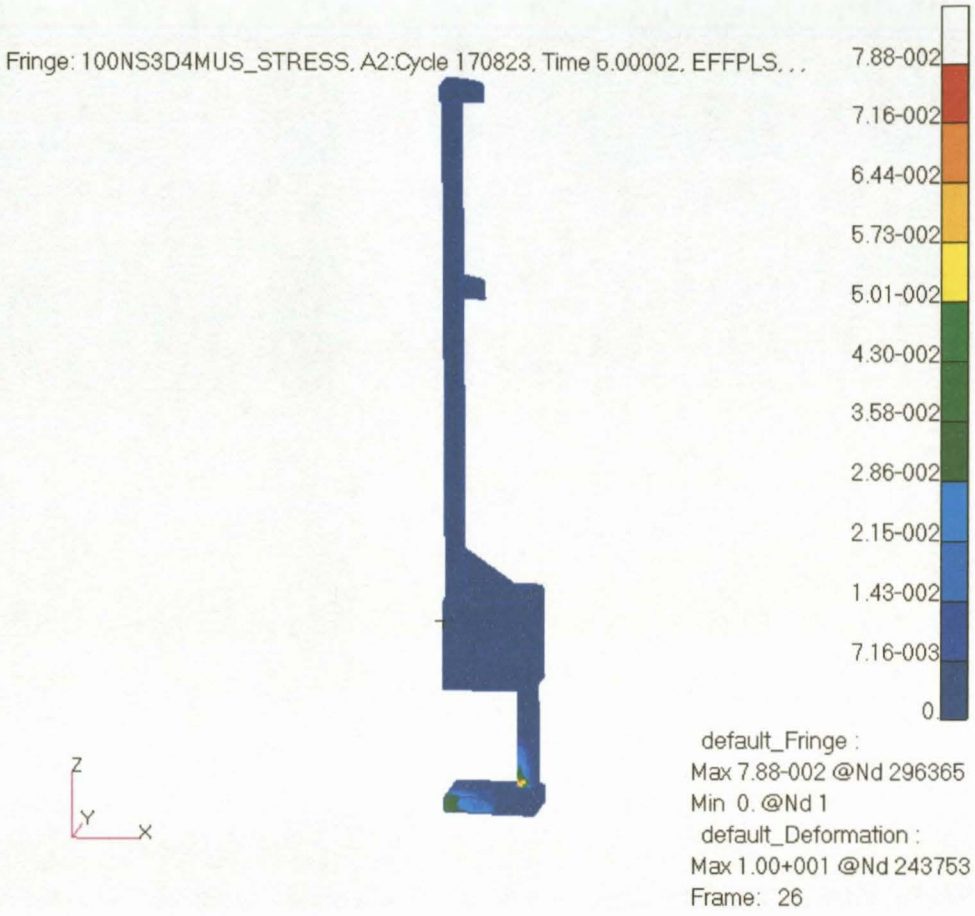

Figure 6.19: The effective plastic strain after 5 ms in the SMI100 due to a 100 N·s impulse applied over 4.3 µs on a burn diameter of 117 mm.

Steady state vibration

Table 6.4 and Table 6.5 summarises the simulation results presented in Figure 6.20 to Figure 6.23, which present the vertical motion of three nodes, the first on the upper surface of the semi-rigid test specimen, the second on the base plate of the target mass and the third at the top of the guide tube. Each table gives the amplitude and frequency of the vibration of the most important nodes in the structure.

Vertical offset, which is reported for each node, is the steady state amount that the structure deforms and is a good indication of global plastic deformation. In all cases it was found that the target mass structure is equally or more deformation resistant than the 40 mm test specimen. In general the vertical offset does not cause concern since it is established within the first 500 μs after the momentum transfer begins, during this period the system will have moved less than 500 μm. Thus it is safe to assume that the associated shift in the COG is a single sudden movement at the beginning of the target mass motion, which will have no effect on the rigid target mass assumption or the measured deflection.

From Table 6.4 the conclusion is drawn that the SMI25 module possesses acceptable axial stiffness. The amplitudes of its vertical oscillation components are low enough as to have no effect on deflection recordings. It is also important to note that the structure will vibrate for about 250 periods before the peak recording is made. During this time structural damping should have significantly reduced the vibration amplitudes. The structural vibrations in the SMI25 module will thus have almost no effect on the recorded amplitudes.

Table 6.4: The response of the SMI25 fine mesh model to a 29.5 N·s impulse.

Node Position	Amplitude [mm]	Vertical Offset [mm]	Frequency [Hz]
Guide Tube Top Midpoint	0.31	-0.1	1030
Target mass	0.25	0	934
40 mm Test Specimen Top Midpoint	0.22	0.1	950

The vibration amplitudes predicted for the SMI100 simulation are also of little concern, since the target mass peak displacement for such a load will be close to 100 mm. At worst, the vibration of the structure will cause a 2.8% uncertainty on the measured deflection, but given the effect of structural damping and the high frequency of vibration this should be much less. The 4.28 mm vertical offset predicted for the top of the test specimen is quite realistic since such large deformations were also noted during the SMI qualification tests.

Table 6.5: The response of the SMI100 model to a 100 N·s impulse.

Node Position	Amplitude [mm]	Vertical Offset [mm]	Frequency [Hz]
Guide Tube Top Midpoint	0.5	-0.53	1280
Target mass	< 0.1	0	NA
40 mm Test Specimen Top Midpoint	0.9	4.28	1150

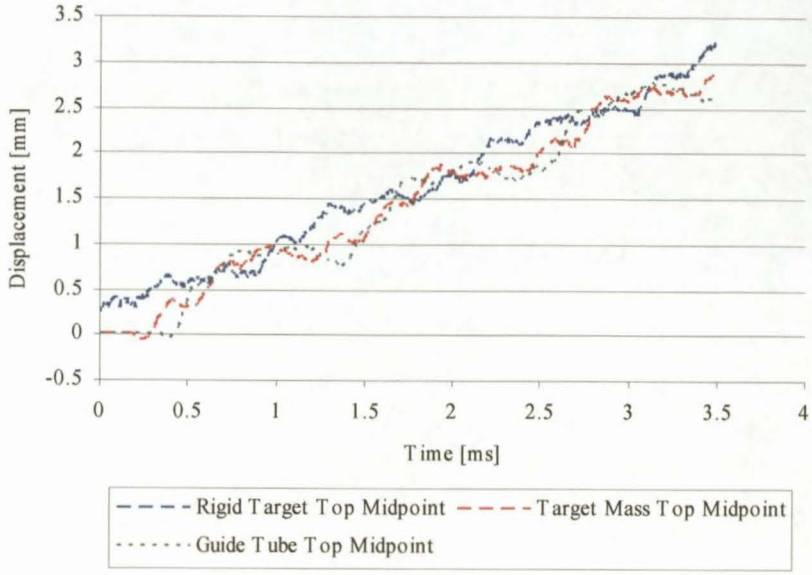

Figure 6.20: A plot of the displacement versus time of three nodes for SMI25 fine mesh model. Mean velocity of 0.83 m/s.

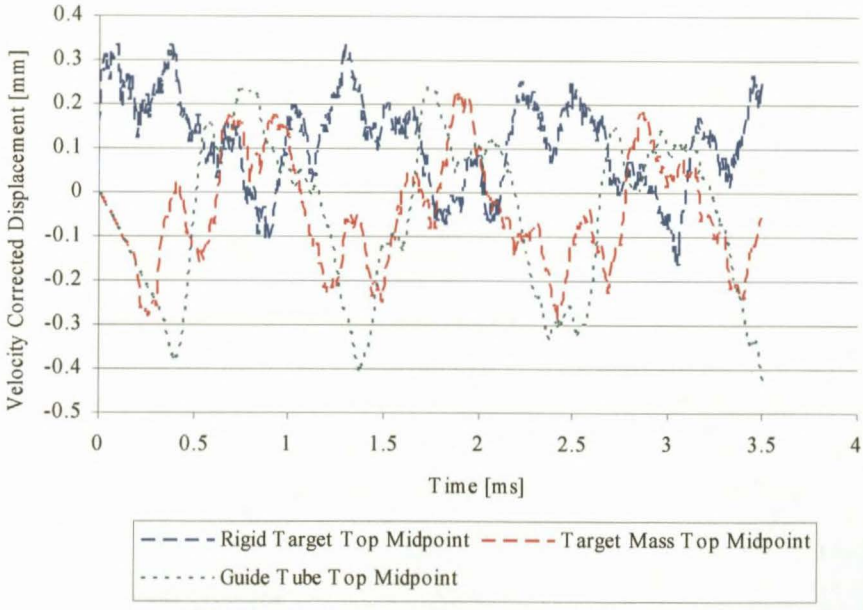

Figure 6.21: A steady-velocity corrected displacement plot of three nodes for SMI25 fine mesh model. Mean velocity of 0.83 m/s.

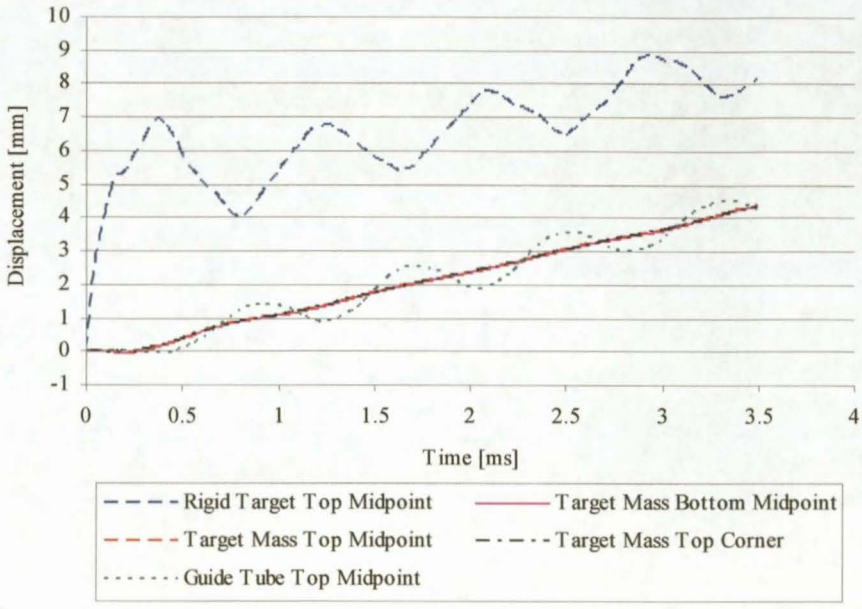

Figure 6.22: A plot of the displacement versus time of five nodes for SMI100 model. Mean velocity of 1.29 m/s.

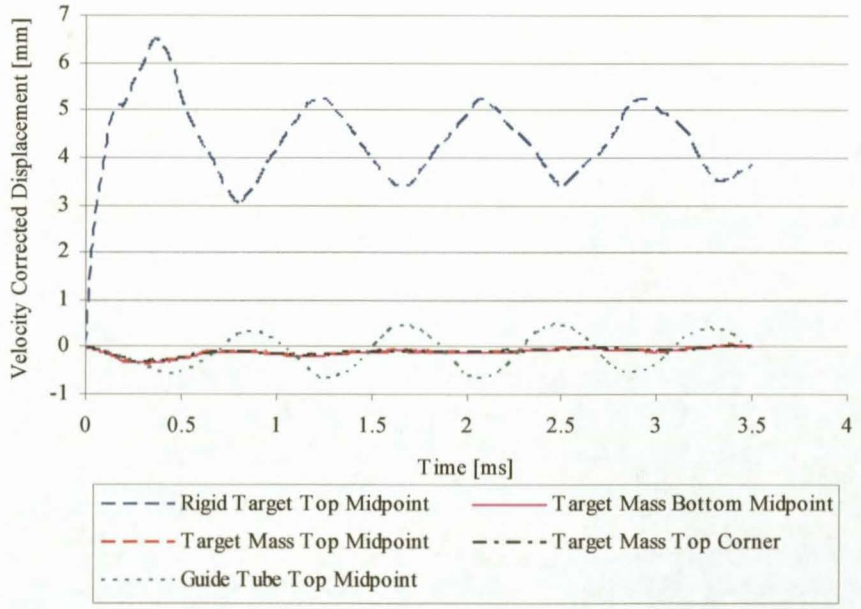

Figure 6.23: A steady-velocity corrected displacement plot of five nodes for SMI100 model. Mean velocity of 1.29 m/s.

6.4. Derivation of the impulse response of a 1-DOF spring-mass system with no losses

In order to model the SMI system it is necessary to derive its impulse response from the system which is closely represented by a single degree of freedom spring-mass system. Figure 6.24 shows such a system, with mass m and stiffness k, in a gravitational field with the constant gravitational acceleration g. Time varying displacement, velocity and acceleration is denoted by $x, \dot{x}$ and $\ddot{x}$ respectively. The assumptions in this derivation are that the mass is rigid and the spring is perfectly linear elastic and massless.

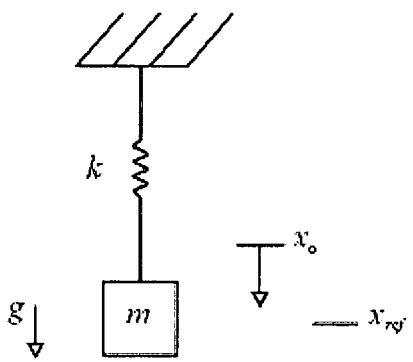

Figure 6.24: A 1-DOF spring mass system, x_0 indicates the end position of the unstretched spring and x_{ref} indicates the end position when stretched by the dead weight of the mass.

From first principles the force F_k generated by a spring:

$$F_k = kx \qquad \textbf{Equation 6.7}$$

From Newton's second law:

$$F = m\ddot{x} \qquad \textbf{Equation 6.8}$$

And the constant gravitational force on the mass is:

$$F_g = mg \qquad \textbf{Equation 6.9}$$

Therefore, from the free body diagram in Figure 6.25, for the spring-mass system to be in equilibrium:

$$mg = -kx_{ref} \qquad \textbf{Equation 6.10}$$

The deflection of the spring due to the weight of the mass can be expressed as:

$$x_{ref} = -\frac{mg}{k} \qquad \textbf{Equation 6.11}$$

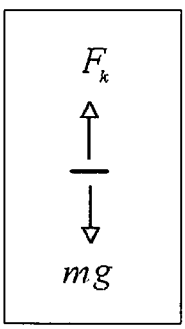

Figure 6.25: The free body diagram of the spring-mass system in equilibrium.

If an additional force or acceleration is applied to the mass, the system will have the following equation of motion:

$$mg + m\ddot{x} = -k\left(x - x_{ref}\right) - kx_{ref} \qquad \textbf{Equation 6.12}$$

Equation 6.12 describes the motion of a spring mass system due to an applied acceleration $\ddot{x}$, in a constant gravitational field, and may be rewritten as:

$$m\ddot{x} = -k\left(x - x_{ref}\right) - \left(mg + kx_{ref}\right) \qquad \textbf{Equation 6.13}$$

Since the gravitational acceleration imposed on a system remains constant, and given that:

$$mg = -kx_{ref} \qquad \textbf{Equation 6.10}$$

The last terms of Equation 6.13 can be cancelled since:

$$0 = mg + kx_{ref} \qquad \textbf{Equation 6.14}$$

Thus Equation 6.11 can be written as:

$$m\ddot{x} = -k\left(x - x_{ref}\right) - 0 \qquad \textbf{Equation 6.15}$$

The reference displacement of the system can now be changed from x_0 to x_{ref}, since x_{ref} is constant. Thus, $x_{ref} = x = 0$, giving:

$$0 = m\ddot{x} + kx \qquad \textbf{Equation 6.16}$$

It is important to note at this stage that Equation 6.16, like Equation 6.12, can be used to describe the motion of a spring-mass system due to an applied acceleration $\ddot{x}$, in a constant gravitational field. Initially the constant gravitational effects were included in Equation 6.12. It was however shown in the steps that follow Equation 6.12 that the effects of gravity remain constant and the gravity related terms cancel each other. Equation 6.16 may therefore be defined as the equation of motion of a spring mass system disturbed from its gravitational equilibrium position $x = 0$.

Equation 6.16 can be shown to have the temporal solution, Inman (2001):

$$x = A\sin\left(\omega_n t + \phi\right) \qquad \textbf{Equation 6.17}$$

with:

A The amplitude of the displacement

ϖ_n The natural frequency of the system, given by:

$$\varpi_n = \sqrt{k/m} \qquad \textbf{Equation 6.18}$$

ϕ The phase shift of the system, determined by non-zero initial displacement, x_0 and velocity, v_0 conditions, Inman (2001).

$$\phi = \tan^{-1}\left(\frac{\omega_n x_0}{v_0}\right) \qquad \textbf{Equation 6.19}$$

Since impulse I is an instantaneous change in system momentum, it may also be defined as an instantaneous change in the velocity Δv of a rigid mass. Therefore:

$$I = m\,\Delta v \qquad \textbf{Equation 6.20}$$

For a stationary mass the applied impulse will result in an initial velocity v_0, which is related to the impulse by:

$$\Delta v = v_0 = \frac{I}{m} \qquad \textbf{Equation 6.21}$$

The instantaneous velocity of the mass at any time may be calculated by taking the derivative of the system equation, Equation 6.16.

$$\frac{dx}{dt} = \omega_n A \cos(\omega_n t + \phi) \qquad \textbf{Equation 6.22}$$

For a system initially stationary and in equilibrium, the phase shift term $\phi = 0$, thus the instantaneous velocity *v(t)* may be expressed as:

$$v(t) = \omega_n A \cos(\omega_n t) \qquad \textbf{Equation 6.23}$$

Equation 6.23 relates the impulse response amplitude *A* to the initial velocity. Therefore the impulse response amplitude may be calculated if the initial velocity due to the impulse is known.

$$A = \frac{v_0}{\omega_n \cos(0)} \qquad \textbf{Equation 6.24}$$

where: $t = 0, v(t) = v_0, x(t) = 0$

By combining Equations 6.18, 6.21 and 6.24, we can simplify the impulse response amplitude equation.

$$\varpi_n = \sqrt{k/m} \qquad v_0 = \frac{I}{m} \qquad A = \frac{v_0}{\omega_n \cos(0)}$$

$$\begin{aligned} A &= \frac{I/m}{\sqrt{k/m}} \\ &= \frac{I}{\sqrt{\frac{km^2}{m}}} \\ &= \frac{I}{\sqrt{km}} \end{aligned} \qquad \textbf{Equation 6.25}$$

By rewriting Equation 6.17 and noting that the phase shift defined in Equation 6.19 is zero since the system is excited in its equilibrium state ($x_0 = 0$), the system impulse response may now be written as:

$$x = \frac{I}{\sqrt{km}} \sin(\omega_n t) \qquad \textbf{Equation 6.26}$$

Equation 6.26 shows that the only parameter needed to simulate the ideal impulse response of a spring mass system is the suspension stiffness, system mass and the natural frequency of the system. Using these values the response of the system can be evaluated for any impulse. The impulse response amplitude, Equation 6.25, can be rewritten to give the applied impulse in terms of the response amplitude recorded in SMI tests. We measure A and wish to calculate I. Thus, in the ideal, frictionless case the applied impulse may be calculated by:

$$I = A\sqrt{km} \qquad \textbf{Equation 6.27}$$

Equations 6.26 and 6.27 are good first order design tools, but not suitably accurate for calculating the impulse in SMI experiments, since they do not compensate for friction losses or spring dynamics. All of the test results presented in this thesis was calculated using a form of Equation 6.26 which was modified to correct for friction losses and spring mass effects. Derivations of these corrections are presented in Appendix A.

For every SMI test case there is an ideal combination of suspension stiffness and target mass parameters that would give the maximum impulse resolution possible. In order to calculate good combinations of these parameters a mathematical, single degree of freedom spring-mass model representing the SMI system was set up. The resulting model which was based on Equation 6.25 was used to predict the deflection of the target mass for a series of impulses between 10 N·s and 75 N·s. This was repeated for three different combinations of suspension stiffness and target mass.

The three combinations of system variables were needed to ensure good measurement resolution over the large impulse span of interest to the SMI. Each of the three basic configurations spanning about 25 N·s each is shown in Figure 6.26, which shows the

expected response for the three different combinations of suspension stiffness and target masses. The response predicted by this figure serves as a quick reference guide for test setups where an optimised impulse resolution is not of great importance. Again the peak deflection was limited to 100 mm amplitude.

For example:
If the SMI25 module with a suspension spring of stiffness 1595 N/m, was set up with a target mass of 38 kg, it would be possible to read from Figure 6.26 that this combination of system parameters would allow impulse measurement between 0 N·s to 25 N·s. If these values are substituted into Equation 6.27 it is found that the amplitude in the 25 N·s load case will be 0.102 m. If the response amplitude is much higher than 100 mm it becomes necessary to increase the mass of the target mass to prevent damage to the SMI the recorder.

$$0.102 = \frac{25}{\sqrt{1595 \times 38}} \text{ [m]}$$

If a test was to be performed with an impulse of say 40 N·s, it would become necessary to move to the SMI50 module with a suspension spring stiffness of 3954 N/m and increase the ballast mass to give a 90 kg target mass.

Figure 6.26 is intended to be a first order selection tool for planning an SMI test. The maximum impulses that can be measured with the SMI modules is presented in Table 6.6.

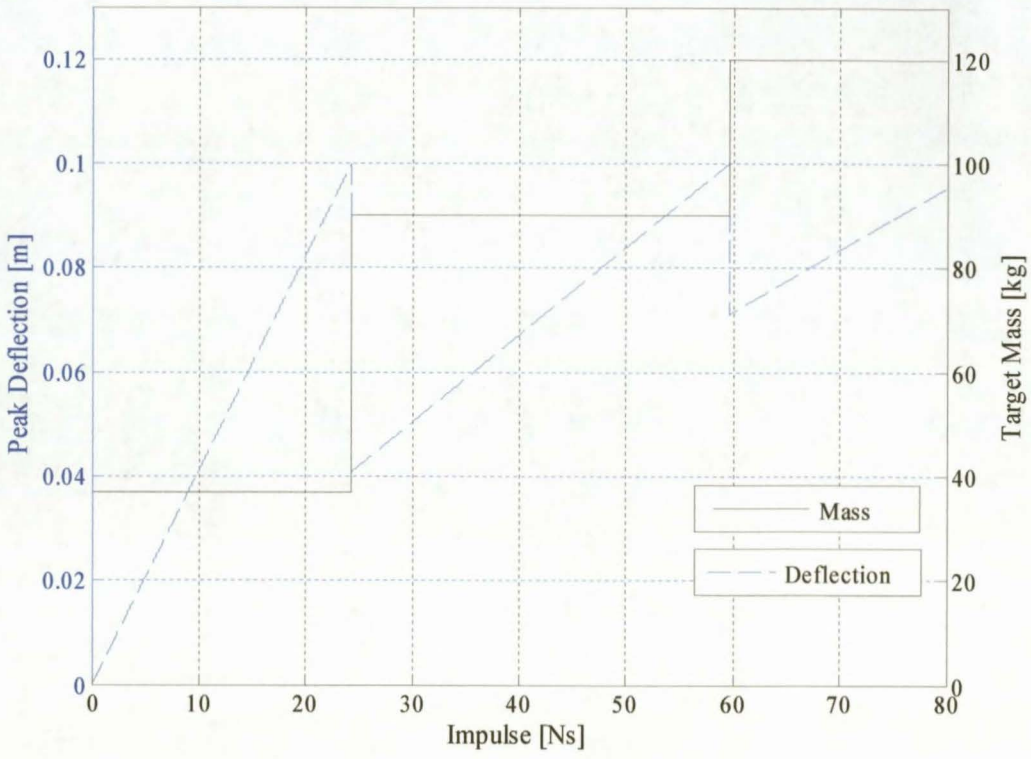

Figure 6.26: Peak Deflection vs. Impulse for different projectile masses and three different springs with k_1=1595 N/m, k_2=3954 N/m, k_3=5873 N/m. The spring stiffness is inversely proportional to the slope of the impulse-deflection curve.

Table 6.6: Impulse measurement capacity of the SMI modules.

Module	Spring Stiffness [N/m]	Peak Design Impulse [N·s]
SMI25	1595	24
SMI50	3954	60
SMI75	5873	82

7. Calibration Tests

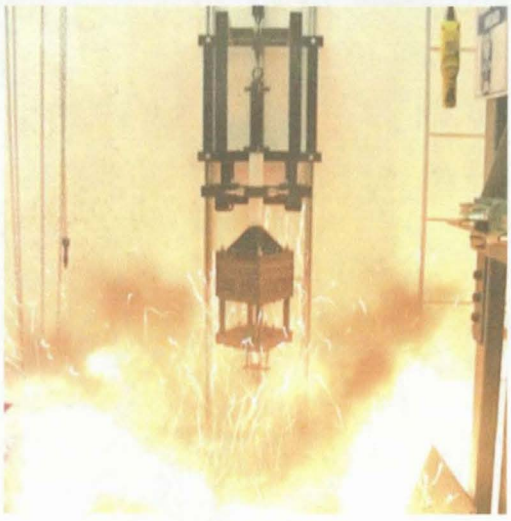

Figure 7.1: The flame produced by an explosion.

A series of calibration experiments were conducted to assess the performance of the SMI relative to a horizontal ballistic pendulum and published data. Bulge tests were performed on mild steel plates of 1.6 mm, 2.5 mm and 4 mm in thickness and an extra series of tests, similar to the bulge tests, but on 20 mm thick steel plates were done for impulse measurements above 35 N·s. Video and still images of the SMI system and some of the qualification tests are presented in Appendix G. Some of the qualification tests were also simulated on BISRU's ballistic pendulum to verify the relative accuracy. Data of experiments performed by Chung Kim Yuen (1997) on mild steel plates were also used for comparison. A summary of the tests performed for this thesis can be seen below in Table 7.1. The test operational procedure is described in detail in Appendix C. The full test results are presented in Appendix F.

Table 7.1: Summary of tests performed.

Test bed	Number of tests
SMI25	20
SMI50	11
SMI75	8
Horizontal Ballistic Pendulum	9

7.1. Dimensionless analysis

The test data collected from the SMI25 and SMI50 tests was compared to that of similar experiments done by other researchers using the Nurick dimensionless number Φ for mode 1 failure and the plate midpoint deflection to thickness ratio. Teeling-Smith and Nurick (1991) report that Menkes and Opat first defined mode 1 failure of beam specimens in 1973, as large inelastic deformation, with mode 2 failure characterised by the start of tearing. Only specimens that showed mode 1 failure were considered for this thesis, since the fragmentation of specimens showing higher failure modes could cause a change in the target mass, violating the conditions for conservation of momentum.

The Nurick dimensionless number, which was introduced in section 2.4, accounts for material properties, specimen thickness and load geometry. The expression for Φ pertinent to circular plate specimens was presented in Equation 2.15.

Figure 7.3 shows that most of the SMI test results falls within the 90% confidence intervals for bulge tests performed on horizontal ballistic pendulums, which were noted by Nurick (1989). This is further proof that horizontal ballistic pendulum experiments can be duplicated on the SMI system. Table 7.2 presents the tensile properties of the materials used in the bulge tests. The dynamic strains were measured using a clip-gauge in a hydraulic tensile test frame and the yield stresses were calculated from the measured strain data. Since the measured yield stress was a dynamic measurement it was necessary to calculate the static yield stresses using the Cowper-Symonds relationship.

Dimensionless analysis allows the comparison of experimental results based on different materials and load geometries. Figure 7.2 compares the SMI data with that of similar tests performed on a ballistic pendulum by Chung Kim Yuen (1997). The fact that the SMI data falls within the range of data points of experiments performed by Chung Kim Yuen on a horizontal ballistic pendulum is proof that the SMI system is capable of reproducing the experiments performed on a ballistic pendulum.

Table B.1: Deviation of the SMI modules response from the ideal impulse response.

Parameter	Unit	SMI25			SMI50		SMI75	
Spring mass	kg	2.60	2.60	2.60	2.91	2.91	4.97	4.97
Swivel joint mass	kg	0.8	0	0.8	0.8	0.8	0.8	0.8
Target mass	kg	35.00	35.80	37.19	98.03	125.46	125.46	117.24
Spring stiffness	N/m	1595	1595	1595	3954	3954	5873	5873
$y = mI + c$								
m difference	m/N·s	-1.00E-05	-2.60E-05	-7.20E-06	-5.00E-07	-3.00E-07	-6.00E-07	-7.00E-07
c difference	m	3.30E-04	8.50E-04	3.26E-04	8.55E-04	1.24E-03	7.30E-04	6.59E-04

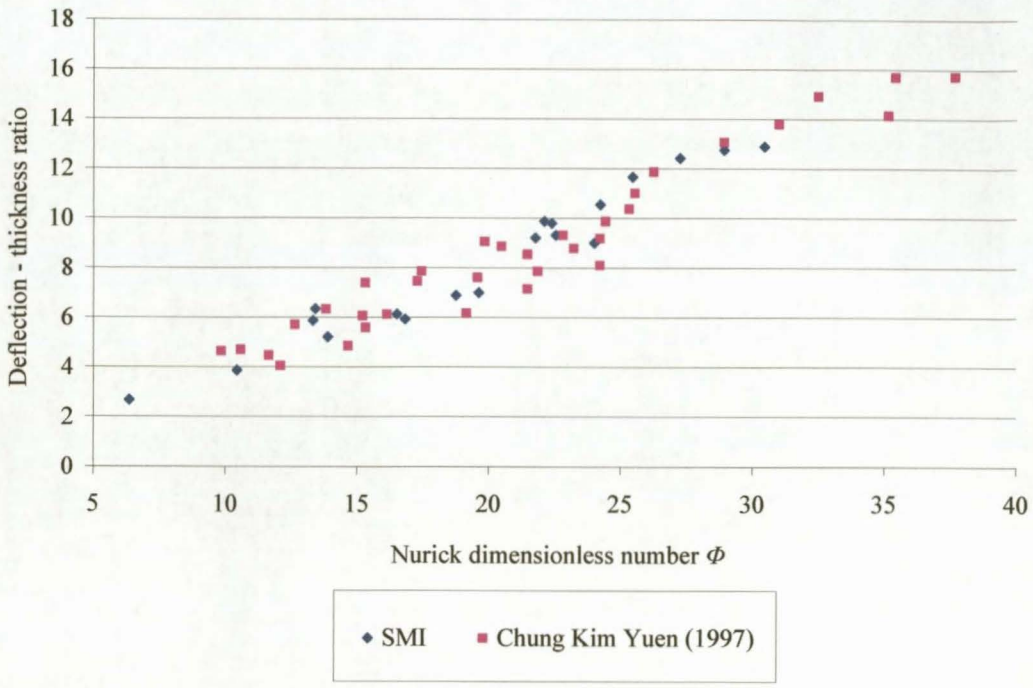

Figure 7.2: A dimensionless comparison of SMI25 and SMI50 bulge test results versus that of Chung Kim Yuen (1997).

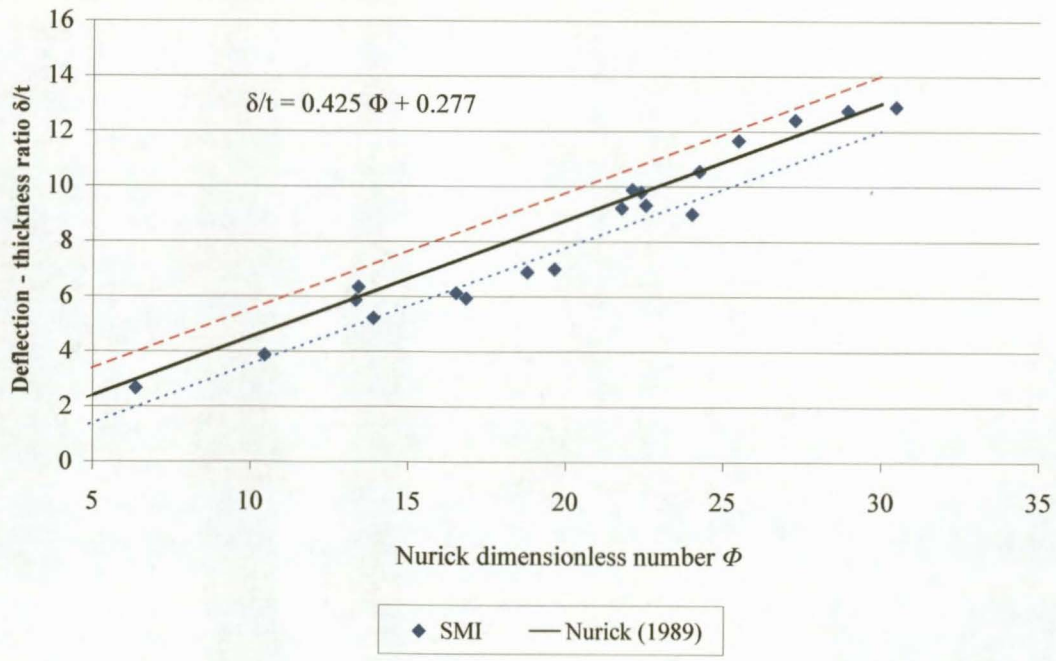

Figure 7.3 A comparison of SMI data with a least squares fit and ±1 deflection-thickness range, which defines the 90% confidence interval of a statistical survey done by Nurick (1989) .

7.2. SMI25 impulse vs. charge mass comparison

The SMI25 module is intended for tests where small impulses below 25 N·s are to be measured. Given that most plate bulge tests are performed in this impulse zone it is likely that the SMI25 will be the module most frequently used by BISRU. Most SMI25 tests were performed with the charge positioned about 0.7 m above the floor.

SMI25 tests were performed using two charge diameters, 33 mm and 40 mm. Initially tests were conducted with a 33 mm charge diameter to allow the comparison of charge mass versus impulse with results from Nurick and Radford (1998). The impulse versus charge mass results is shown in Figure 7.4. The SMI25 results compare well with those of Nurick and Radford and Chung Kim Yuen (1997), falling within the trend of the data. The results of Figure 7.4 are however too closely spaced to give clear indications as to the linearity of the response.

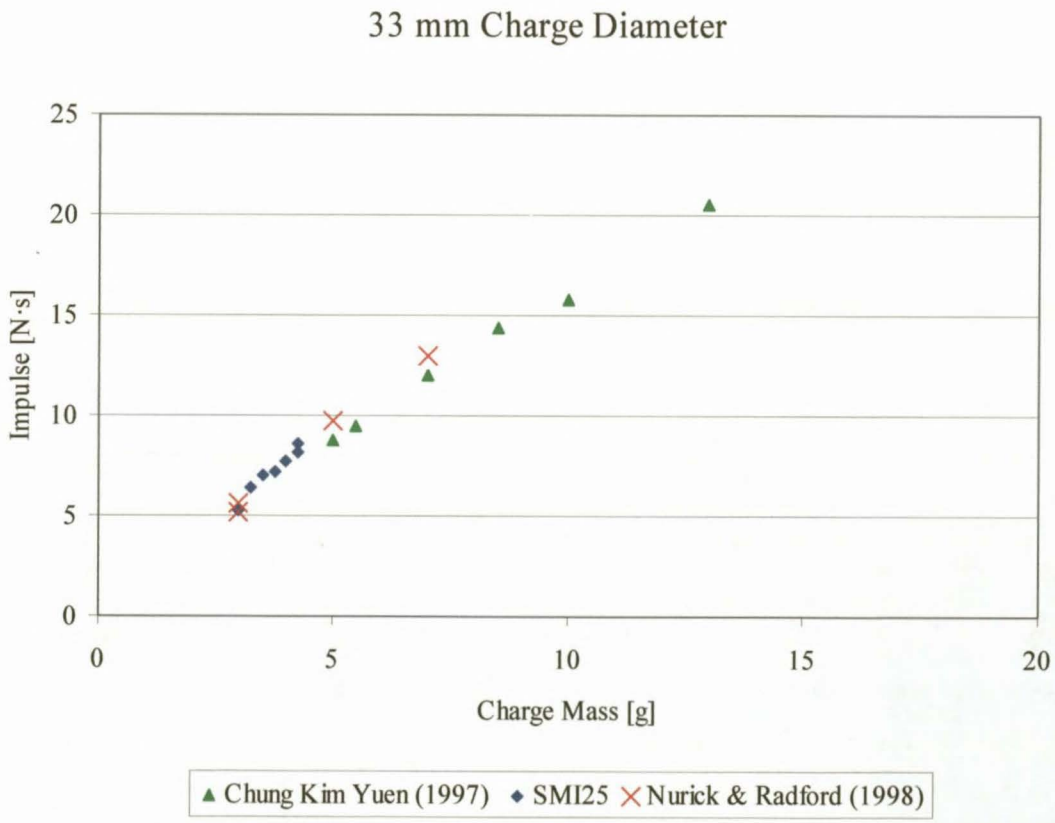

Figure 7.4: A comparison of the impulse measured by the SMI25 module for a 33 mm charge diameter and similar tests found in literature.

The linearity of the SMI25 impulse vs. charge mass data is better illustrated in Figure 7.5, which covers the SMI25 tests performed with 40 mm charge diameters. In this case the SMI25 compares very well with data from horizontal ballistic pendulum tests performed for this thesis, with the data obeying a linear trend as expected. Again the spread in experimental results is made clear by the difference in the horizontal ballistic pendulum results presented by Chung Kim Yuen (1997) and those performed for this thesis.

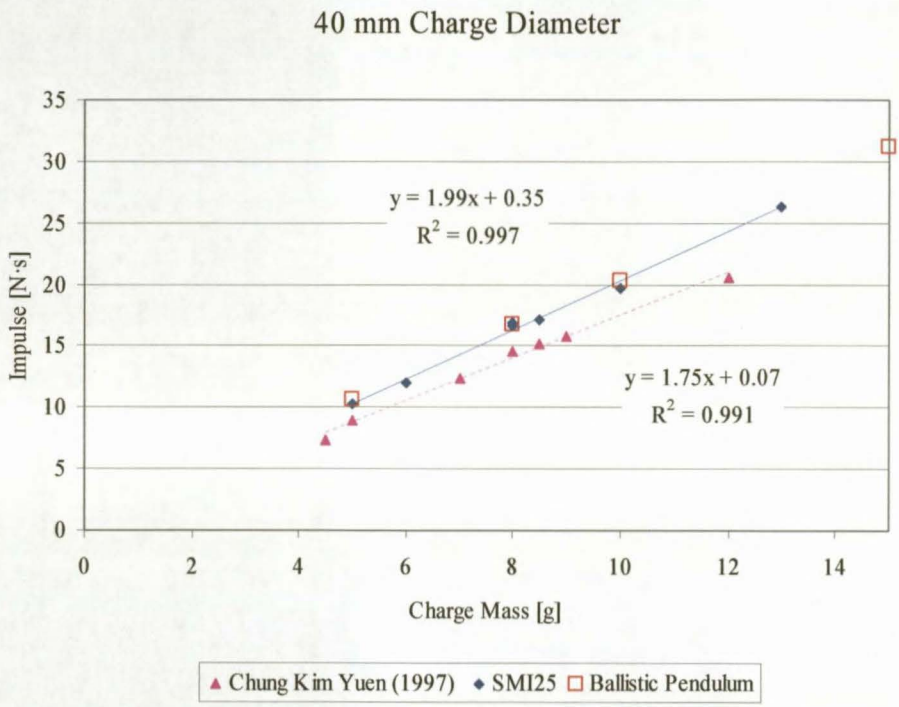

Figure 7.5: A comparison of the measured impulse vs. charge mass for a 40 mm charge diameter as measured by the SMI25 module, the ballistic pendulum and Chung Kim Yuen (1997). All data points represent plate specimens with mode 1 failure.

7.3. SMI50 impulse vs. charge mass comparison

The second SMI module to be tested was the SMI50, which is intended for measuring impulses between 25 N·s and 50 N·s. This impulse zone represents the limits of plate bulge tests since the 100 mm diameter specimens invariably tear if they are less than 4 mm thick. The clamp sandwich used to contain the plate specimens also begins to fail at these impulses. The upper part of the working envelope was therefore evaluated using a "semi-rigid" 244 mm × 244 mm, 20 mm thick, solid plate clamped to the 20 mm thick front clamp with a 100 mm diameter hole as used in the usual thin plate tests. No comparable test data could be found in literature, since these impulses are above that of the common bulge tests. For this reason the SMI50 tests were only correlated against the horizontal ballistic pendulum data generated for this thesis. The SMI50 tests were mostly performed with the charge positioned approximately 0.5 m above the floor. Figure 7.6 presents the SMI50 test results, which show a linear trend, but with an average of about 8.6% lower impulse per charge mass than the horizontal ballistic pendulum.

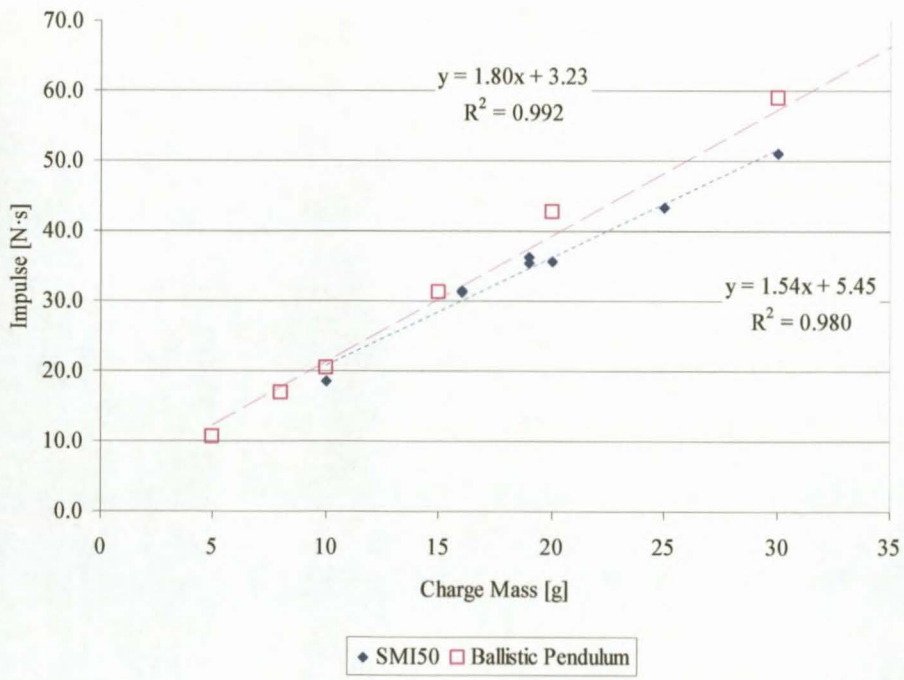

Figure 7.6: A comparison of the measured impulse vs. charge mass for a 40 mm charge diameter as measured by the SMI50 module and a ballistic pendulum. All data points represent plate specimens with mode 1 failure or "semi-rigid" specimens.

7.4. SMI75 impulse vs. charge mass comparison

The last SMI module to be tested was the SMI75, which is intended for measuring impulses between 50 N·s and 75 N·s. As a result of the high impulse magnitude solid, 20 mm thick, plates loaded over a 100 mm diameter area were used as test specimens for all SMI75 tests. The loaded area was defined by a 20 mm thick front clamp with a 100 mm diameter hole, which was clamped to the front surface of the test specimen. The explosive charge, mounted on a 100 mm diameter 12 mm thick polystyrene standoff disk, was then placed in the hole in the front plate. The SMI75 tests were performed with the explosive charge positioned approximately 0.58 m to 0.68 m above the floor.

Figure 7.7 shows a comparison of the SMI75 results with that from the horizontal ballistic pendulum. On average the SMI75 impulse measurements show about 8.8% lower measured impulse versus charge mass than similar tests done on the horizontal ballistic pendulum.

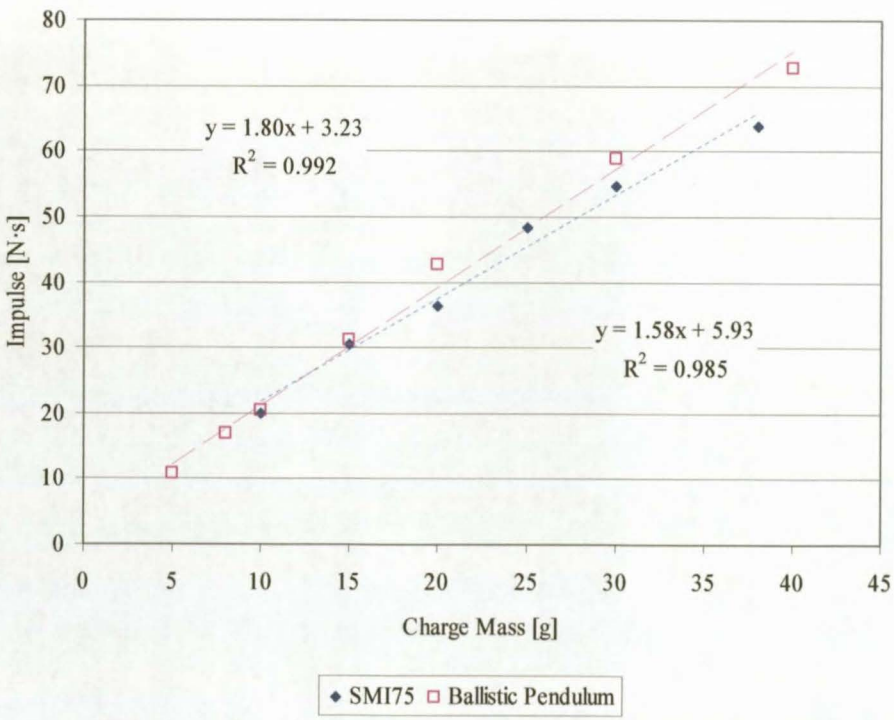

Figure 7.7: A comparison of the measured impulse vs. charge mass for a 40 mm charge diameter as measured by the SMI75 module and a ballistic pendulum. All data points represent plate specimens with mode 1 failure or "semi-rigid" specimens.

7.5. Test data quality and repeatability

Some of the tests performed on the SMI system were repeated to assess the system's ability to consistently give the same impulse measurement for identical tests. The variation of the measured impulses from the mean measured impulse for identical tests is presented in Figure 7.8 for each of the repeated measurements.

Figure 7.8 not only gives a measure of test repeatability, but will also give an indication as to the validity of test data. The repeated tests show good repeatability with about ±2.5% variation in repeated measurements. The increased variation in measured impulse for identical tests above 40 N·s is attributed to a change in the experimental procedure brought on by the high blast loads.

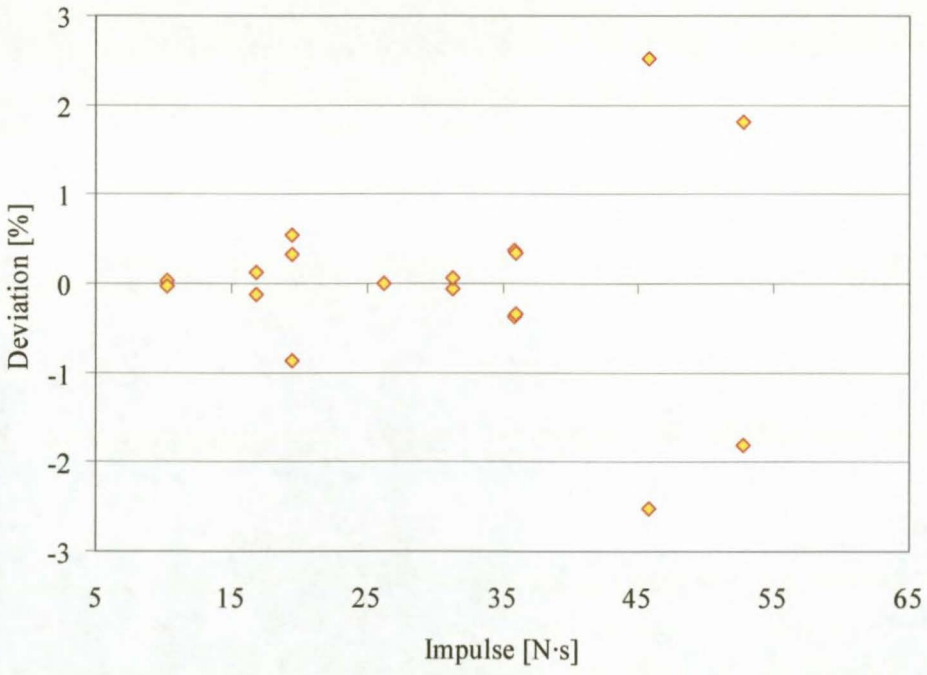

Figure 7.8: The deviation from the mean measured impulse of identical tests done with the SMI system. The SMI system has measurement repeatability to less than ±1% for the qualification tests measurements below 40 N·s.

Figure 6.2 shows the normal clamp setup with a set of 8 M10 bolts on a PCD of 170 mm to clamp a thin test specimen between two 20 mm thick plates with 100 mm diameter holes. Another set of 4 M12 bolts on a 200 mm square grid is used to bolt the

clamp sandwich to the standoff bars. At loads above 35 N·s, bending of the back clamp plate causes the thread to be stripped out of the M10 nuts. It was expected that the bending, which caused the axial failure of the M10 bolted joints, could be reduced by replacing the back clamp and the test specimen by a single 20 mm thick plate. With the first repeated test above 35 N·s the M10 bolts continued to fail and it was decided to continue testing at higher impulse with only the set of 4 M12 bolts to keep the clamp together. Based on the deterioration in test repeatability it seems that this may have been a bad decision.

It has now been established that the data for the impulse measurements above 35 N·s which were performed using semi-rigid test specimens is less perfect than those performed at lower impulse magnitudes. Now the question arises whether the error in the data is larger than that of similar tests performed by other authors.

Figure 7.9 presents the deviation of measured impulse from the impulse predicted by a least squares fit of the ballistic pendulum results shown in Figure 7.7. All of the tests presented were performed using a 40 mm charge diameter and only specimens that displayed mode 1 failure are presented.

The mean deviation and deviation range of each data set in Figure 7.9 is presented in Table 7.3. This table shows that both data sets are characterised by 10% to 20% variations between the measured impulse and that predicted by a least squares fit.
Table 7.3 therefore leads to the conclusion that the impulse source is the main cause of the variation in measured impulse versus charge mass. The fact that the SMI results show the same degree of variation as those by Chung Kim Yuen (1997) proves that the SMI has impulse measurement accuracy much smaller than the uncertainty associated with the impulse source.

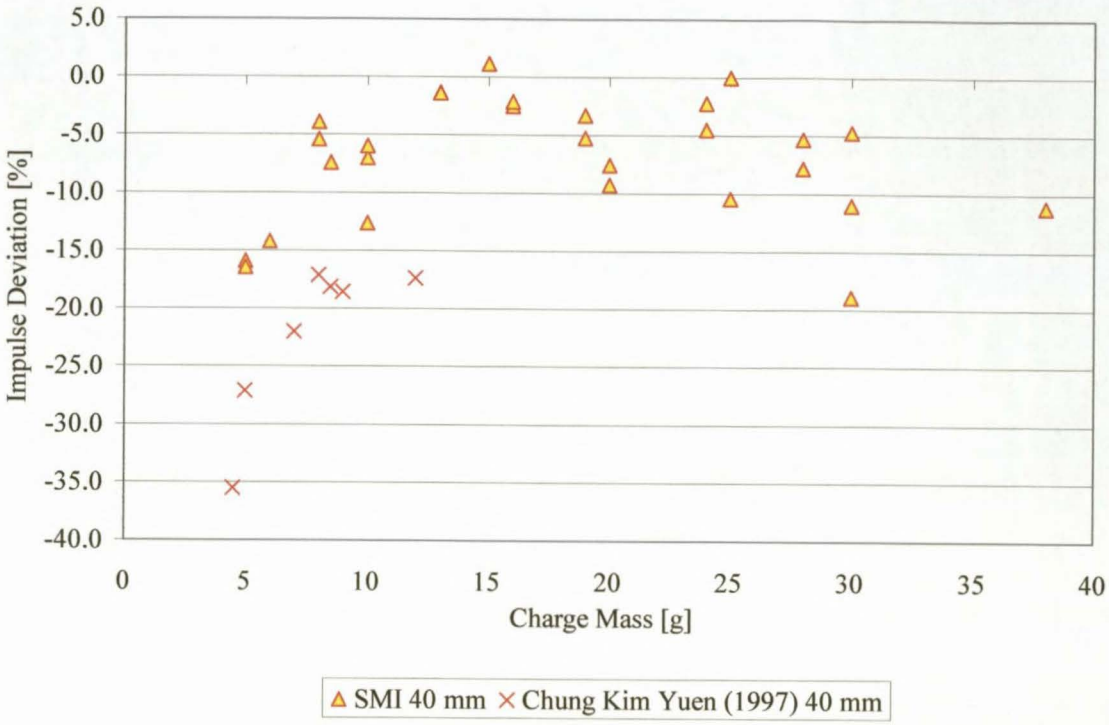

Figure 7.9: Experimental data from several sources showing the impulse measurement error relative to a linear curve fit for each data set versus charge mass.

Table 7.3: A summary of Figure 7.9.

	SMI 40 mm	Chung Kim Yuen (1997) 40 mm
Mean Deviation [%]	-7	-22
Deviation Range [%]	20	18
Number of data points	28	18

Figure 7.10 shows that the test results of the SMI system falls within the least squares fits of similar tests performed on horizontal ballistic pendulums. If it is assumed that difference in the two sets of ballistic pendulum results presented in Figure 7.10, represents the extent of the impulse source uncertainty, then the fact that the SMI results fall between the results of those tests proves the SMI accuracy to be at least similar to that of the horizontal ballistic pendulum.

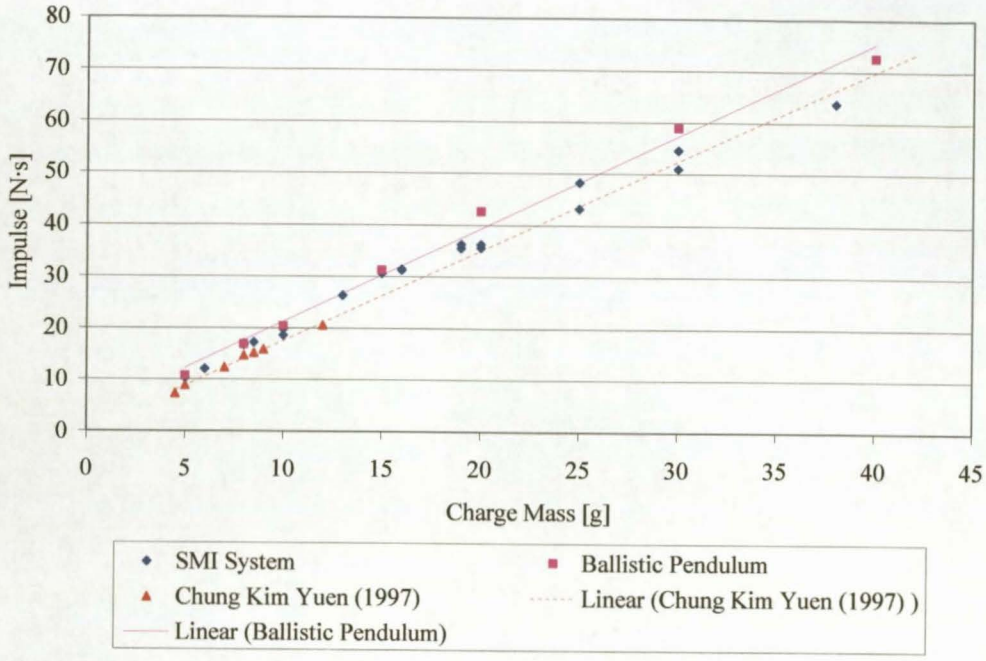

Figure 7.10: A comparison of the measured impulse vs. total charge mass for mode 1 failure plate-bulge tests and tests on rigid test specimens done on the SMI system with 40 mm charge diameter.

8. Conclusion

The SMI system was tested against a horizontal ballistic pendulum and the results were compared to published data from tests performed on horizontal ballistic pendulums. The most successful comparison method was found to be based on non-dimensional analysis. Non-dimensional analysis showed that the SMI25, over its whole range, and the SMI50 over a limited range, has the ability to produce results similar to those of a ballistic pendulum.

Figure 7.2 and Figure 7.3 showed that the non-dimensional results of the SMI system are accurate to within the magnitude of experimental variation of similar tests performed on horizontal ballistic pendulums. Non-dimensional analysis was however only useful up to impulse magnitudes of 35 N·s. Thereafter the plate bulge test specimens started to show mode 2 failures and the data could no longer be analysed in non-dimensional form using existing theory.

The explosive yield or impulse versus charge mass was used to compare test results at impulse magnitudes above 35 N·s. Explosive yield data from literature and horizontal ballistic pendulum tests was used to evaluate the measured impulse versus charge mass of the SMI system, but it was found that explosive yield is too erratic to use as a quantitative metric. The only conclusion that could be drawn from these comparisons in Figure 7.9 and Figure 7.10 was that the SMI system shows the same magnitude of measured impulse variation versus charge mass as any test done on a horizontal ballistic pendulum.

It was also shown by Figure 7.8 that the SMI system can perform impulse measurements with repeatability better than ±2.5%. Thus it was demonstrated that the SMI system could measure impulse, with excellent repeatability and with accuracy similar to that of a horizontal ballistic pendulum.

A series of 39 qualification tests were performed without a serious structural or system failure, proving the system to be sufficiently robust. During the series of tests it was also proved that the system could perform measurements over the range of impulses between 5 N·s and 64 N·s.

It is therefore concluded that the majority of specifications set for the design have been met. The ability to accurately measure vertical impulse forms a crucial milestone in the development of the capability to perform impulse measurements on buried charges. It is expected that the SMI system will be quite capable in measuring the blast effects of buried charges, since it incorporates design features such as variable standoff distance, modularity and flexibility. All of these features were included to allow the testing and installation of almost any conceivable test specimen to the base plate of the target mass assembly.

9. Recommendations

The accuracy of the SMI75 and SMI50 impulse measurements was not fully demonstrated and it is advised that these modules be evaluated in future with non-dimensional analysis. Impulse measurement variation due to blast wave reflection off the floor beneath the SMI system was also not investigated. It is recommended that the effect of this phenomenon be quantified.

The simple theory used to account for spring dynamics could also not be verified in detail for this thesis. It should be very interesting to see how well it accounts for spring dynamics.

A further recommendation is that the SMI system be investigated for user friendliness, e.g. the addition of an overhead block and tackle to aid in safely raising and lowering the target mass which can easily weigh in excess of 100 kg. Another modification which would greatly improve the user friendliness of the SMI system is to replace the recorder with an LVDT. An LVDT will introduce much less Coulomb friction into the system than the current recorder. It will also do away with the need to manually zero the recorder between the placing of the charge and of the detonator, reducing the exposure time and number of personnel in the blast cell. Recording of the peak deflection by electronic means should not be too severely affected by the EMI caused by the detonator, since the peak displacement only occurs 250 m·s later.

Probably the most important recommendation is a thorough examination and quantification of the accuracy of horizontal ballistic pendulums. The impulse source for such an investigation should not be explosives but rather an impactor with known mass and velocity.

The most important recommendation for future work is the application of the SMI system to measure the blast effects of buried charges. The system has been proven in simple air blasts and work may now proceed on more complex impulse measurements from buried charges.

10. References

American Society for Testing and Materials, ASTM A 370 – $02^{\varepsilon 1}$, "*Standard test methods and definitions for the mechanical testing of steel products*".

Callister, W.D., *Material Science and Engineering – An Introduction*, Fifth Edition, Wiley and Sons Inc., 2000.

Chung Kim Yuen, S., *Investigation into the effect of plate thickness on localised blast loads*, Pre-graduate thesis, University of Cape Town, 1997.

Chung Kim Yuen, S., Nurick, G.N., "*Experimental and numerical studies on the response of quadrangular stiffened plates. Part I* ", Int. J. Impact Engng., Vol. 31 pp 55–83, 2005.

Chung Kim Yuen, S., Nurick, G.N., "*The significance of the thickness of a plate when subjected to localised blast loads*", 16th International Symposium on Military Aspects of Blast and Shock (MABS16), Oxford, UK, Proceedings pp 491–9, September 2000.

Cook, R.D.,"*Finite Element Modeling for Stress Analysis*", J. Wiley & Sons, New York, 1995

Drotleff, J.E., Vincent, C.T., Mullen, S.A., Walker, J.D., Morris, B.L., "*Research in Close-In Blast Loading From High Explosives*", Report ARL-CR_308 prepared for the U.S. Army Research Laboratory, Aberdeen Proving Ground MD 21005–5066, September 1996.

Farrow G.H., Nurick G.N., and Mitchell G.P. *Modelling of impulsively loaded circular plates using the Abaqus Finite Element code*. Proc. 13th Symp. Finite Element methods in South Africa. Stellenbosch, South Africa Jan1995.

Humphreys, J.S., Plastic *deformation of impulsively loaded straight clamped beams*, J. appl. Mech. Vol 32, pp 7-10, 1965.

Inman, D.J., *Engineering Vibration*, Second Edition, Prentice Hall, 2001.

Jacob, N., Chung Kim Yuen, S., Nurick, G.N., Bonorchis, D., Desai, S.A., Tait, D., "*Scaling aspects of quadrangular plates subjected to localised blast loads – experiments and predictions*", Int. J. Impact Engng., Vol. 30 pp 1179–1208, 2004.

Johnson, W., *Impact Strength of materials*. Edward Arnold, London, 1972.

Jones, N., *Structural Impact*. Cambridge University Press, Cambridge 1989.

MSC.Dytran Theory Manual, Version 2005, MSC.Software Corporation, Part Number: DT*V2005*Z*Z*Z*DC-TEO, 2004.

MSC.Dytran User's Guide, Version 2005, MSC.Software Corporation, Part Number: DT*V2005*Z*Z*Z*DC-USR, 2004.

Nurick G.N., "*An Empirical Solution for Predicting Maximum Central Deflections of Impulsively Loaded Plates*", Inst. Phys. Conf. Ser. No 102: Session 9. Paper presented at the International Conference on the Mechanical Properties of Materials at High Strain Rates, Oxford, 1989

Nurick, G.N., Martin, J.B., "*Deformation of Thin Plates Subjected to Impulsive Loading – A Review, Parts I and II*", Int. J. Impact Engng., Vol. 8 No. 2 pp 159–186, 1989.

Olson, M.D., Nurick, G.N., Fagan, J.R., "*Deformation and Rupture of Blast Loaded Square Plates – Predictions and Experiments*", Int. J. Impact Engng., Vol. 13 No. 2 pp 279–291, 1993.

Radford, A.M. and Nurick, G.N., "*Circular plates subjected to localised central blast loads. Transient loading and response of structures.*", An International Symposium honouring Arnfinn Jenssen (Eds. M Langseth, T Krauthammer), Trondheim, Norway, Proceedings pp 503–548, May 1998.

Teeling-Smith, R.G., Nurick, G.N., "*The Deformation and Tearing of Thin Circular Plates Subjected to Impulsive Loads*", Int. J. Impact Engng., Vol. 11 No. 1 pp 77–91, 1991.

Canadian Centre for Mine Action Technologies, Website: http://www.ccmat.gc.ca/TestFacilities/index_e.html#mechanical, December 2005.

Appendix A: Compensation Factors and Error Analysis of the SMI System

A.1 The impulse response amplitude correction to include linear viscous damping

From the study of the free response of single degree of freedom spring-mass systems it becomes evident that the addition of linear viscous damping causes the amplitude of the response to decay in an exponential fashion such as in Figure A.1. For very lightly damped systems there is very little difference, less than 1%, between the natural frequency of the damped and undamped system. For the SMI the effect of viscous losses is so small that they are negligible. The viscous damping coefficient of the target mass c, was calculated to be in the order of 0.6 kg/s to 0.7 kg/s, using the logarithmic decrement method described by Inman (2001). The damping coefficient remains constant for objects of similar size and shape, but a more mathematically convenient expression for damping in a system is the damping ratio, ζ. Inman (2001) defines the damping ratio of a spring mass system as:

$$\zeta = \frac{c}{2\sqrt{km}} \qquad \textbf{Equation A.1}$$

The damping ratio of most SMI systems was calculated to be less than 0.0014.

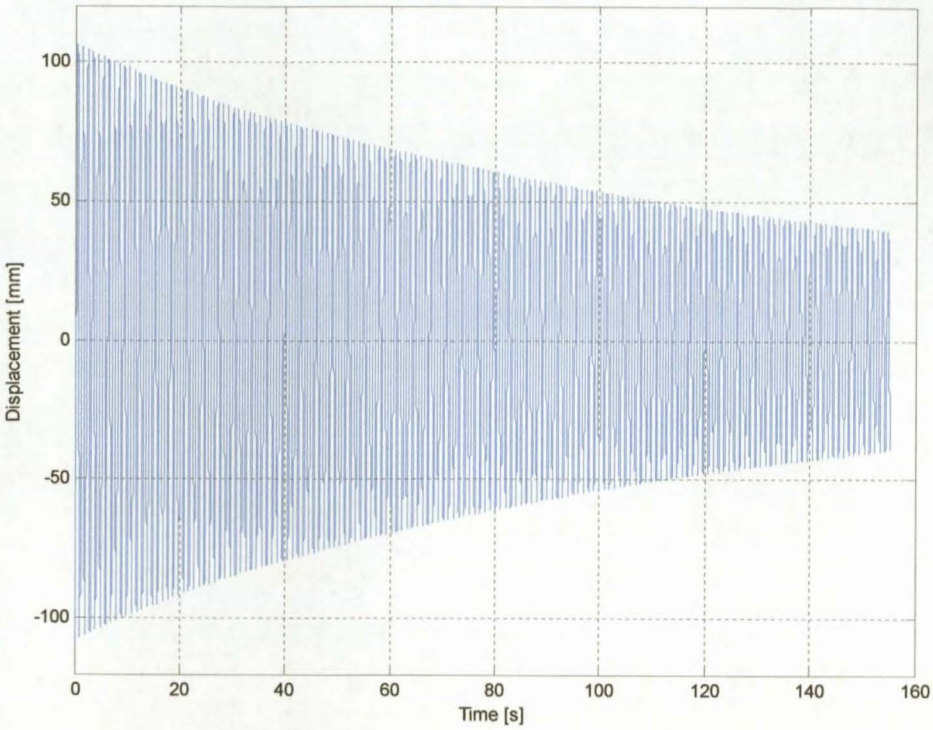

Figure A.1: A typical time deflection test result for SMI during its free response with linear viscous damping.

To correct the SMI response for this predictable amplitude decay requires the addition of an exponential decay term to the impulse response in Equation 6.26 to adjust the amplitude. This term can be shown to be $e^{-\zeta\varpi_n t}$,(Inman, 2001). Therefore, the impulse response for a system with very light linear viscous damping, initially at equilibrium, is given by:

$$A_i = \left(e^{-\zeta\varpi_n t}\right)\frac{I}{\sqrt{km}} \qquad \textbf{Equation A.2}$$

where: $t = \frac{\tau}{4}, \frac{3\tau}{4}, \frac{5\tau}{4}, \frac{7\tau}{4}$, with oscillation period τ.

For a typical SMI system with $\tau = 1$, and therefore $\omega_n = 2\pi$ and $\zeta = 0.0014$ the decay after a quarter period will be

$$\begin{aligned} \text{Decay} &= 1 - \exp\left(-0.0014 \times 2\pi \times 0.25\right) \\ &= 0.0022 \end{aligned}$$

This translates to a 0.22% amplitude decay. A comparison of the free viscous damped response of the SMI system with two simulated responses is shown in Figure A.2. The first simulation with a 0.7 kg/s damping coefficient was presented to show how well the SMI response could be simulated. The second response simulation had a zero friction coefficient and the close agreement between the three responses indicate the futility of viscous friction correction.

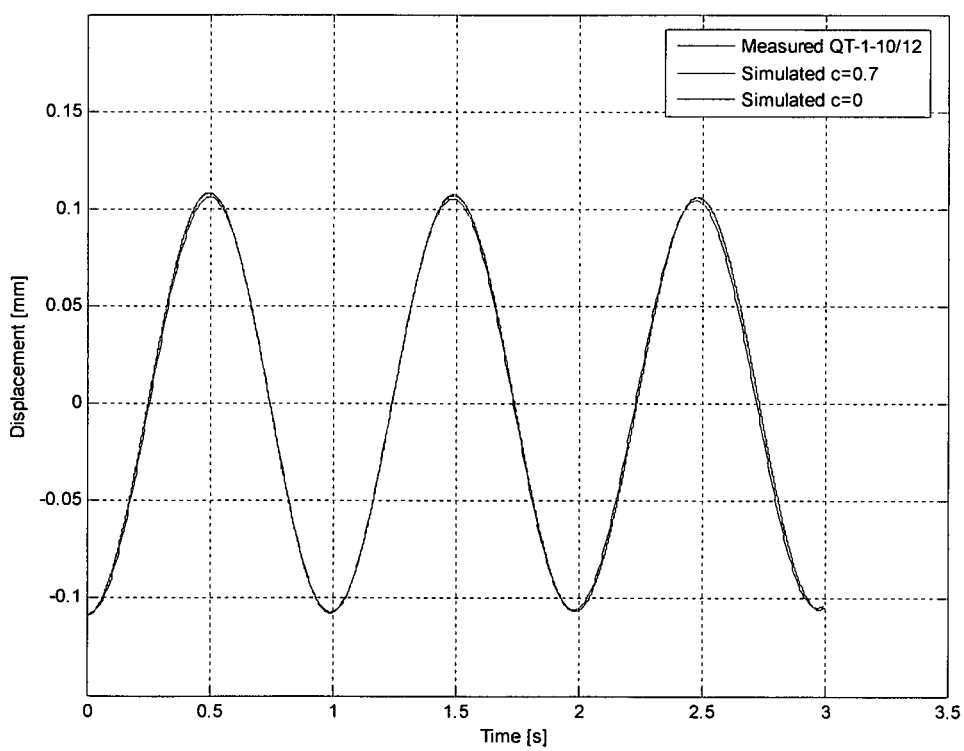

Figure A.2: A comparison of the free viscous damped response of the SMI system with simulation using various damping values.

A.2 The impulse response amplitude correction to include Coulomb damping

From the study of the free response of single degree of freedom spring-mass systems it becomes evident that the addition of Coulomb damping causes the amplitude of the response to decay in a linear fashion, as shown in Figure A.3. To correct the response for this predictable amplitude decay requires the addition of a linear decay term to the impulse response in Equation 6.26 to adjust the amplitude.

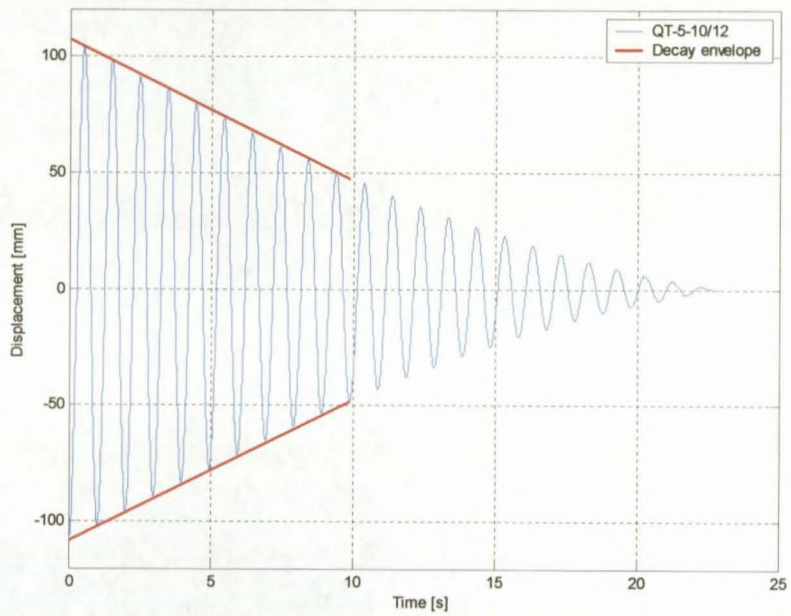

Figure A.3: The response in test QT-5-12/10, the linear decay envelope indicating the extent of Coulomb damping. This system includes a very small viscous damping component, but its effect is negligible relative to that of Coulomb damping.

This term for a horizontal spring mass system, with the mass resting on a rough surface, has been shown by Inman (2001) to be:

$$\frac{\Delta A}{\Delta t} = \frac{2\mu mg\varpi_n}{\pi k} \qquad \textbf{Equation A.3}$$

Where μ is the coefficient of dynamic friction and $\frac{\Delta A}{\Delta t}$ is the slope of the linear decay envelope.

In the case of the SMI recorder, which is the main source of Coulomb damping in the SMI system, the force between the sliding surfaces (pen tip and paper) is not *mg*, but $F_{pens.}$ Thus the correction term becomes:

$$\frac{\Delta A}{\Delta t} = \frac{2\mu F_{pens}\,\varpi_n}{\pi k} \qquad \textbf{Equation A.4}$$

Where F_{pens} is the sum of the four pen force magnitudes.

Therefore, the impulse response amplitude for a system with light Coulomb damping, initially at equilibrium, is given by:

$$A_i = \frac{I}{\sqrt{km}} - t\left(\frac{2\mu F_{pens}\,\varpi_n}{\pi k}\right) \qquad \textbf{Equation A.5}$$

where $t = \frac{\tau}{4}, \frac{3\tau}{4}, \frac{5\tau}{4}, \frac{7\tau}{4}$, with system period τ.

If the peak amplitude of a system with Coulomb friction is known, the applied impulse may be calculated by rewriting Equation A.5 in the form below:

$$I = \left(A + t\left(\frac{2\mu F_{pens}\,\varpi_n}{\pi k}\right)\right)\sqrt{km} \qquad \textbf{Equation A.6}$$

Equation A.6 has the same form as Equation 6.27, but with a Coulomb damping corrected amplitude $A_{corrected}$:

$$A_{corrected} = \left(A + t\left(\frac{2\mu F_{pens}\,\varpi_n}{\pi k}\right)\right) \qquad \textbf{Equation A.7}$$

The mathematical relation shown in Equation A.6 is convenient for simulation and theory purposes, but in practice the coefficient of dynamic friction and the pen forces are difficult to measure. One solution for this problem is to do characterization tests, where the SMI is set up with an initial displacement and released. Its subsequent response is then logged by the recorder and the amplitude decay is calculated from the recorder traces. Back substitution of the calculated decay slope in Equation A.4 is used to calculate the friction force μF_{pens}, which is then employed to correct future test data in which the same pens and paper are used with the same pen pressure.

Example:

For a SMI setup with target mass m = 125 kg, suspension spring stiffness k = 5000 N/m and system period τ = 1 s. Recorded first peak amplitude A_1=100 mm, recorded second peak amplitude A_2=95 mm.

$$\frac{\Delta A}{\Delta t} = \frac{A_2 - A_1}{\tau}$$
$$= \frac{100-95}{1}$$
$$= -5\,\text{mm/s}$$

From the recorded amplitudes it is calculated that Coulomb friction causes the peak amplitude of the systems impulse response to decay linearly by 5 mm/s or 5 mm per period. The target mass reaches its first peak amplitude a quarter period after the impulse is applied at t = 0.25 s, therefore its amplitude will have decayed by:

$$5 \times 0.25 = 1.25 \text{ mm.}$$

The Coulomb friction corrected amplitude; $A_{corrected}$, can then be calculated by adding the decay to the recorded first peak amplitude.

$$A_{corrected} = A_1 + 1.25$$
$$= 100 + 1.25$$
$$= 101.25\,\text{mm}$$

The applied impulse is then calculated by:

$$I = A_{corrected}\sqrt{km}$$
$$= 0.10125 \times \sqrt{5000 \times 125}$$
$$= 80\,\text{N·s}$$

A.3: The effect of measurement errors

Measurement errors have the potential to invalidate test results; therefore it is essential that the significance of errors in each measurement be evaluated. If the system responds as a frictionless single degree of freedom spring-mass system and all system parameters have been measured exactly, then the impulse-amplitude relationship will be:

$$I = A\sqrt{km} \qquad \textbf{Equation A.8}$$

If a measurement error factor ε_{km} is introduced in either the target mass or suspension spring stiffness measurement the calculated impulse becomes:

$$I_{\varepsilon} = A\sqrt{km\,\varepsilon_{km}} \qquad \textbf{Equation A.9}$$

The factor by which the calculated impulse becomes erroneous will be:

$$\frac{I_{\varepsilon}}{I} = \frac{A\sqrt{km\,\varepsilon_{km}}}{A\sqrt{km}} = \sqrt{\varepsilon_{km}} \qquad \textbf{Equation A.10}$$

Therefore the error in the calculated impulse will be smaller than the square root of the error factor made in the measurement of the suspension spring stiffness or the target mass. The suspension spring stiffness measurements were done with less than 0.13% variation in the measurements and the mass of the target mass can easily be measured to within 50 g, which represents an error of 0.143% on a 35 kg target mass. Given the accuracies of these parameters, the uncertainty in the calculated impulse due to the combined mass and stiffness measurement errors is in the order of 0.14%. The accuracy of the measured impulse response amplitude has a directly proportional effect on the accuracy of the calculated impulse; given an amplitude measurement error factor ε_A it follows that:

$$\frac{I_{\varepsilon}}{I} = \frac{A\varepsilon_A\sqrt{km}}{A\sqrt{km}} = \varepsilon_A \qquad \textbf{Equation A.11}$$

The amplitude measurement is usually done with an electronic vernier calliper which has 0.03 mm measurement repeatability. The recorder pen traces are 0.5 mm wide. Assuming the trace width to be the main source of measurement error in the ideal system, the error made on a 20 mm amplitude measurement will be 2.5%. According to Equation A.11, the error in the measured impulse will also be 2.5%. For a 100 mm amplitude measurement, the error will be in the order of 0.5%. Therefore tests should be planned and set up for amplitudes greater than 20 mm to maintain accuracy.

The accuracy of the Coulomb damping correction is more difficult to quantify since it is possible for the friction force to vary significantly between periods. The correction strategy employed uses the average decay over the first full period to calculate the decay over the first quarter period, up to the first peak amplitude. Since the Coulomb correction requires an second amplitude measurement to calculate an average decay, which is then divided by four before being added to the first amplitude measurement. It is therefore fair to assume that the error involved is no larger than twice the amplitude measurement error divided by four, or 0.25 mm.

According to the numerical analyses presented in Appendix B, the deviation of the SMI impulse response from that of the ideal 1-DOF spring-mass system, due to spring mass effects, is less than 1.25 mm on the recorded amplitude. By employing an impulse response relationship derived from numerical simulations for each SMI module instead of the ideal relationship, the error can theoretically be fully compensated for. Since the effect of spring inertia on the system is so small, the true Coulomb and viscous losses will be nearly identical to that of the ideal case, and may be corrected in the same way as for the ideal 1-DOF spring-mass system.

In Appendix A.2, it was reported that viscous damping reduces the measured first peak amplitude of the SMI25 module by 0.22%.

Thus the total measurement error on any SMI measurement should be less than the sum of the pen resolution and the measurement error on the Coulomb correction:

$$0.5 + 0.25 = 0.75 \text{ mm}$$

The error factor on the calculated impulse will then be:

$$\text{Error Factor} = \text{Amplitude Measurement Error} \times \ldots \text{Mass Error} \times \text{Stiffness Error} \times \text{Viscous Damping Error}$$

$$\text{Error Factor} = \left(1 + \frac{0.5 + 0.25}{\text{Coulomb Corrected Deflection}}\right) \times \sqrt{1.0014} \times \sqrt{1.0014} \times 1.0022$$

Thus the impulse calculation error is typically in the range of 1.1% to 4.1%, with higher response amplitudes giving more accurate measurements.

A.4 Derivation of the correction for non-negligible mass springs

Inman (2001) presents the following derivation for the calculation of a term for the dynamic mass of a spring using energy principles. During the oscillation of a one degree of freedom spring-mass system, such as shown in Figure A.4, the fixed end of the spring will have zero velocity and the moving end will have velocity $\dot{x}$. It is therefore assumed that the velocity of the spring varies linearly over its length and that it has mass m_{spring}.

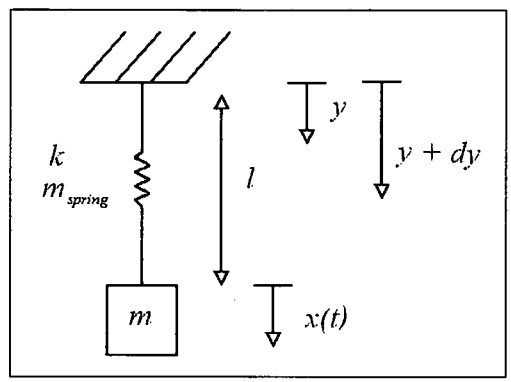

Figure A.4: A 1-DOF spring-mass system.

The kinetic energy E_k of a moving mass m, moving at velocity v, is described by:

$$E_k = \frac{1}{2}mv^2 \qquad \textbf{Equation A.12}$$

A set of relationships for the mass and velocity of the spring at various points along its length needs to be established in order to calculate the kinetic energy of a spring with one end moving and the other stationary.

The velocity v of the spring changes linearly along its length, therefore its velocity at any point "y" over its length l can be described by:

$$v(y) = \left(\frac{y}{l}\dot{x}\right) \qquad \textbf{Equation A.13}$$

A real spring also has evenly distributed mass along its length and there for its mass per unit length may be expressed as:

$$m = \frac{m_{spring}}{l} \qquad \textbf{Equation A.14}$$

By integrating the distributed kinetic energy of spring along its length it is possible to calculate the kinetic energy of the whole spring. The resulting Equation A.17, has the same form as the kinetic energy equation, Equation A.12, but the mass term is only a third of the total spring mass. This indicates that the dynamic mass of a spring with fixed-free end conditions is actually a third of the total spring mass. Thus all analyses that include spring mass effects should at least add a third of the total spring mass to the moving mass to compensate for spring mass effects.

$$\begin{aligned} E_k &= \int_0^l \frac{1}{2} m\, v(y)^2 dy \\ &= \frac{1}{2}\int_0^l \left(\frac{m_{spring}}{l}\right)\left(\frac{y}{l}\dot{x}\right)^2 dy \\ &= \frac{1}{2}\left(\frac{m_{spring}}{3}\right)\dot{x}^2 \end{aligned} \qquad \textbf{Equation A.15, A.16 and A.17}$$

Appendix B: Spring Dynamics Correction

It is important to realise that excessive spring mass not only affects the assumptions used in the derivation of the impulse response, but also the ability of the spring to follow the sudden motion of the target mass as it accelerates after the impulse is applied.

FE analysis has shown in Figure 6.20, that once an impulse is applied, the target mass accelerates to a constant mean velocity within 200 μs to 400 μs. Generally the inertia of an initially lightly loaded spring is so large that it is unable to match such high acceleration. Consequently, contact between the target mass and suspension system is temporarily lost. When contact is lost, the internal forces in the spring have to accelerate the spring and all suspension elements at its free end. Thus the larger the mass of the spring and the elements it has to accelerate, the less the chances of maintaining contact with the target mass.

Once the target mass loses contact with its suspension system it goes into ballistic flight and the only force acting on it is due to gravity, which slows it down. The spring on the other hand starts to accelerate to a velocity higher than that of the target and eventually the two collide. During the collision, the momentum of the moving suspension elements is distributed between the two colliding bodies so that the two bodies move at a common velocity afterwards. The collision can be seen as a secondary impulse on the target mass, which leads to measurement errors.

The effect of spring contact loss during the first few milliseconds was simulated for a system with a target mass of 125.5 kg , spring mass 2.91 kg, spring constant 3954 N/m and a 0.8 kg swivel joint between the target mass and spring. The result of that simulation is shown in Figure B.1.

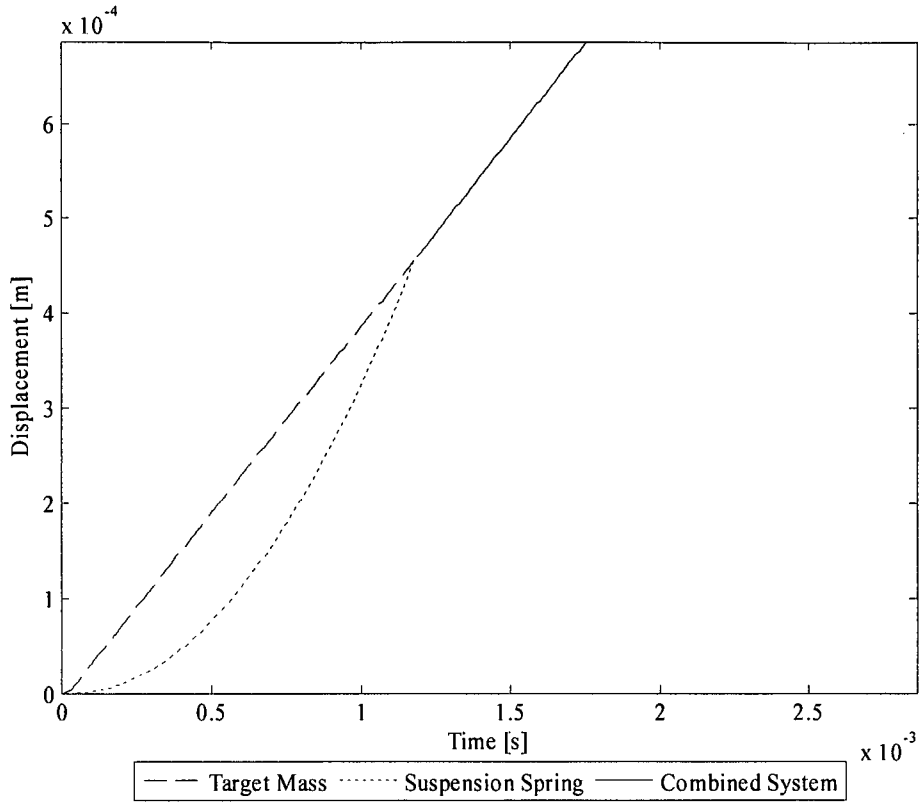

Figure B.1: The time-deflection history showing the initial separation of the spring and target mass. A change in the momentum of the target mass is evident from the very slight change in the slope after the re-uniting of the target mass and suspension system.

A second set of simulations were run to see how these events, which occur during the first 1 ms to 8 ms, depending on the target mass, affects the validity of a 1-DOF spring-mass model. Figures B.2 and B.3 present the results of these simulations and they indicate that there is a slight difference in the impulse response amplitudes of the ideal system and that of the SMI.

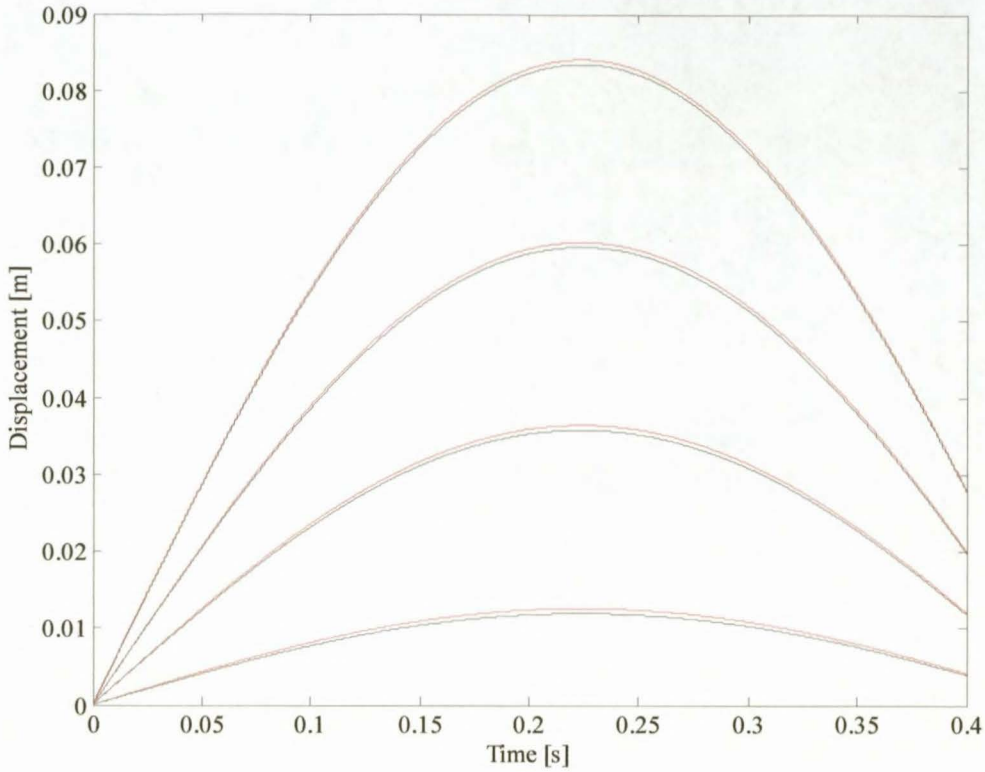

Figure B.2: A comparison of the ideal 1-DOF spring-mass system impulse response (black), versus that of SMI (red).

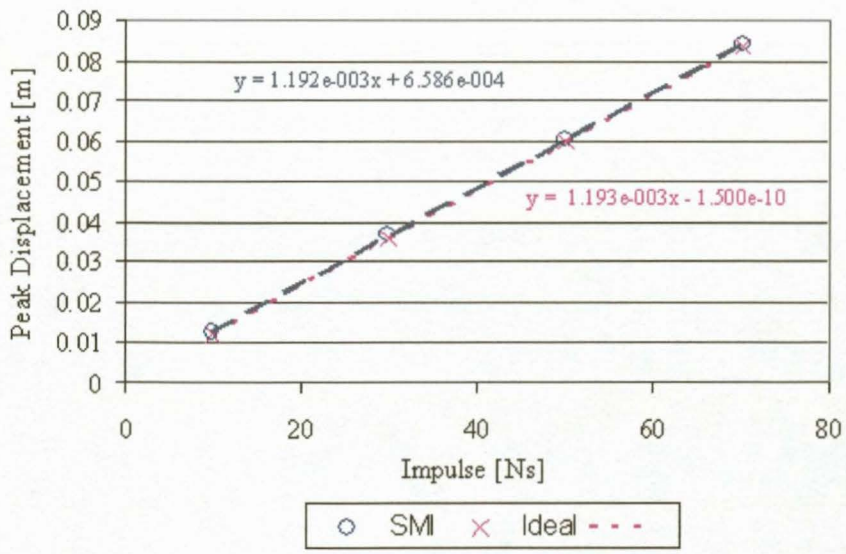

Figure B.3: The peak impulse response amplitude of the SMI compared to that of an ideal 1-DOF spring-mass system.

All analyses have shown that the impulse response of all SMI system combinations used in the qualification tests is linear. The analysis data can be seen in Table B.1, which shows that the SMI modules have a very small difference in the impulse versus displacement factor relative to the ideal case, with a constant positive offset of less than 1.25 mm. The offset is dependent on the target mass, heavier target masses tend to have a larger offset. An offset of 1.25 mm represents an error of 2.5% on 50 mm amplitude, which is acceptable, given the variability of blast loading. A 5% error on 25 mm amplitude, however, needs to be corrected. Correcting only the smallest amplitudes for this error would be too tiresome and prone to error, therefore a revised impulse response relationship for each system combination used in testing was formed from the results of a numerical simulations.

The linear impulse response relationship has the standard form:

$$I = my + c \qquad \textbf{Equation B.1}$$

Where y is the measured peak amplitude and the calculated impulse is I.

Table E.1: The spring characteristics of the SMI suspension springs.

Spring	Average Spring Coefficient [N/m]	Standard Deviation on Spring Coefficient [N/m]	Coefficient of Variation on Spring Coefficient Tests [%]	Pre-load [N]	Maximum Extension [mm]	Spring Mass [kg]	Minimum Extension for Linearity [mm]	Total Length [mm]
25 N·s	1595	1.7	0.11	145	500	2.6	20	500
50 N·s	3954	5.27	0.13	400	270	2.91	20	600
75 N·s	5873	2.95	0.05	400	270	4.97	20	750

Table E.2: The spring-based system characteristics of the SMI.

Spring	Maximum Static Load [N]	Minimum Target Mass for FSD Accuracy [kg]	Maximum Dynamic Load [N] 100 mm Amplitude]	τ min [s]	τ max [s]
25 N·s	943	35	783	0.931	1.406
50 N·s	1468	90	1072	0.948	1.045
75 N·s	1986	115	1398	0.879	0.979

Appendix C: Operational Procedure

C.1: Exeriment Design

It is suggested that the following steps are followed in the design of an experiment using the SMI system.

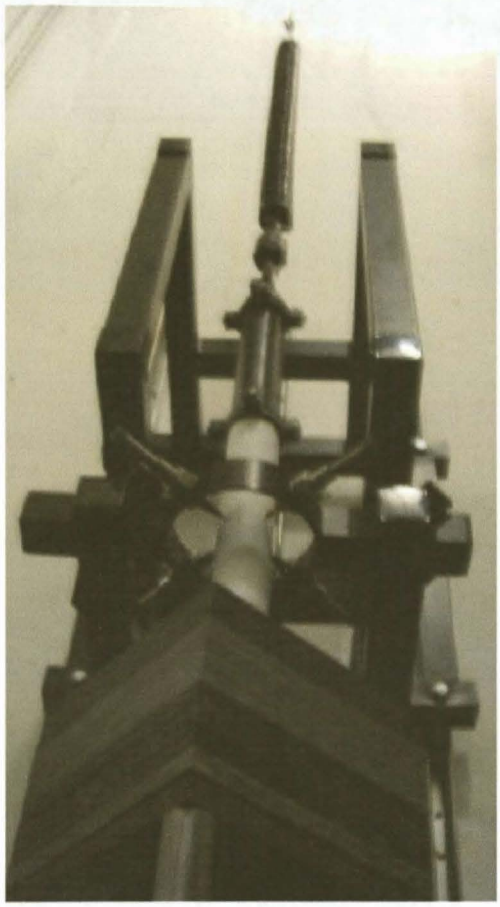

Figure C.1: The SMI system.

1. Decide on specimen geometry.
2. Decide on the loading magnitude.
3. Design specimen holder. For very low impulse tests, minimise the mass of the clamp structure. Try to keep the footprint of the specimen holder to 244 mm × 244 mm.
4. Calculate the mass of the specimen and specimen holder.
5. Calculate the total mass of the target mass, including all moving parts including the D-shackles between the spring and the target mass.
6. Calculate the suspension spring stiffness needed to keep the initial velocity below 0.75 m/s and the response amplitude to less than 100 mm.

7. For high impulse values, ballast mass in the form of 244 mm × 244 mm steel plates may be added to the target mass to reduce the initial velocity and peak amplitude.
8. Once the mass of the suspension spring is known it becomes possible to correct for the massless spring assumption in the impulse response derivation by adding a third of the mass of the suspension spring to the moving mass.
9. Prepare an A4 sheet of 80 g/m^2 paper for each test, noting the test number, specimen details and loading condition. The recording will be in portrait layout.

C.2: Test Setup

The following steps were followed during the SMI tests:

1. Weigh the moving components and note their masses. Table C.1 gives an example of the measured masses

Table C.1: Target mass component masses.

Component	Mass [kg]
Two D-shackles and Swivel joint	1
Basic Target	15.64
4 × M12 Hex-Key Bolts	0.815
Ballast Mass 1	9.15
Ballast Mass 2	9.18
Ballast Mass 3	9.15
Ballast Mass 4	9.13
Ballast Mass 5	9.18
Ballast Mass 6	7.6
Ballast Mass 7	7.82
Ballast Mass 8 & 9	17.18
4 × Standoff Bars	3.08
4 × M12 C-Sunk Clamp Bolts	0.204
8 × M10 C-Sunk Clamp Bolts & M10 nuts	0.344
Top Clamp	7.81
Bottom Clamp	7.74
Specimen (4 mm)	3.02
Total Moving Mass Uncorrected for spring mass	118.043

13. Connect the free end of the suspension spring to the target mass using a D-shackle and wire-tie the shackle bolt.
14. Carefully remove the table from under the target mass.
15. Attach the target and its support structure to the standoff bars.
16. Loosen the Uni-Rail mounting bolts of the recorder support frame and lower the frame so that the recorder is positioned in the middle of the recorder zone on the guide tube of the target base. From this point the target mass can travel 150 mm upwards and downwards before the ballast mass or lower bearing guide hits the recorder.
17. Adjust the recorder support frame to ensure that the recorder is level.
18. Place a set of pens in the recorder and centre the recorder to ensure that it is concentric with the recording tube.
19. Remove the recording pens and note the period of the free system. If this differs by more than 2% from the theoretical value the mass of the target mass must be checked. If the mass is correct the spring must be tested over its whole range to see if its stiffness is correct. This step is the main calibration check in this experiment.
20. Position the detonator holder below the test specimen, making sure that the non-polystyrene components of the detonator holder clears the corners of the target mass by at least 20 mm during downward travel. Tighten the two Uni-Rail bolts that fix the detonator holder to the wall.
21. Apply a 10 mm wide swath of Pritt adhesive to one side of a long edge of the recorder paper. Wrap the recorder paper in portrait orientation around the recorder section guide tube and stick the overlapping section to the Pritt adhesive swath.
22. Place the pens in the pen holders and connect the elastic threads. Make sure not to mark the recorder paper. This is done by placing each pen in its safe position by pulling it partially out of the pen guide tube until the pen tip enters the guide tube. Then let the elastic threads pull the pen back towards the paper while applying a slight sideways thrust.
23. Place the explosive charge mounted on a polystyrene standoff disk under the specimen.
24. Release the pens onto the paper; a slight tap on the side of the pen holder will release it onto the paper, but be careful not to let the pen tip impact the paper.

25. Rotate the recorder tube to produce a zero deflection line. Check that each pen is giving a clear trace.
26. Thread the leads of a detonator through the 5 mm hole in the one end of the polystyrene detonator holder.
27. Slide the other end of the polystyrene detonator holder into the friction clamp channel of the rigid part of the detonator holder and adjust the holder so that the detonator's leader charge sticks to the centre point of the main charge.
28. Check that the pens have not moved from their zeroed position.
29. Connect the detonator leads to the detonating system.
30. Apply the impulse.
31. The SMI system will go into Coulomb damped Simple Harmonic Motion.
32. Disengage the recorder once the target mass stops oscillating, remove the recording pens from their guides and remove the recorder paper from the recorder tube.
33. Measure the amplitude of the first two negative peaks. Check that the measured amplitudes are equal for all four pens, otherwise calculate and use the average amplitudes.
34. Calculate the true first peak amplitude by adding a quarter of the difference between the first two negative peaks to the first peak amplitude. This corrects for Coulomb friction losses.
35. Calculate the Impulse from the true peak amplitude, the corrected moving mass and the spring stiffness.

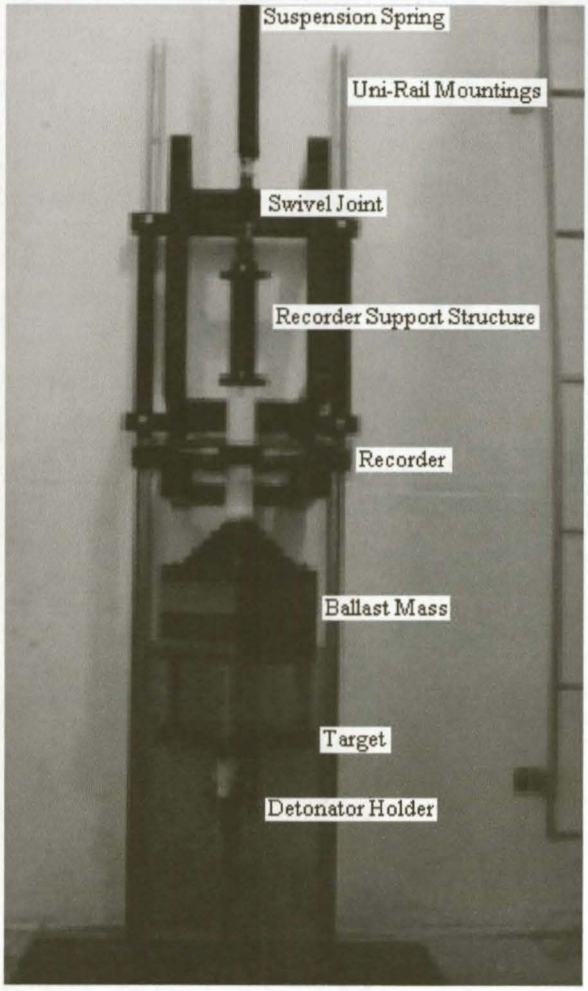

Figure C.2: The SMI system. Note that the swivel joint is incorrectly placed; it should be above the suspension spring.

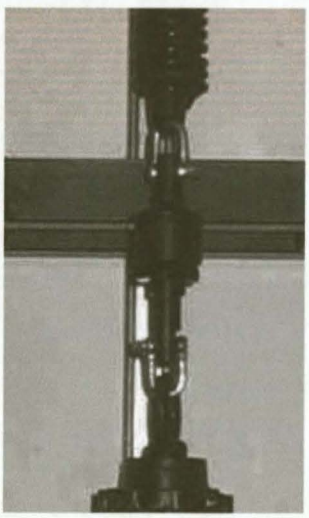

Figure C.3: The swivel joint shown between the target mass and the suspension spring. The swivel joint should never be placed below the spring, but always directly above it.

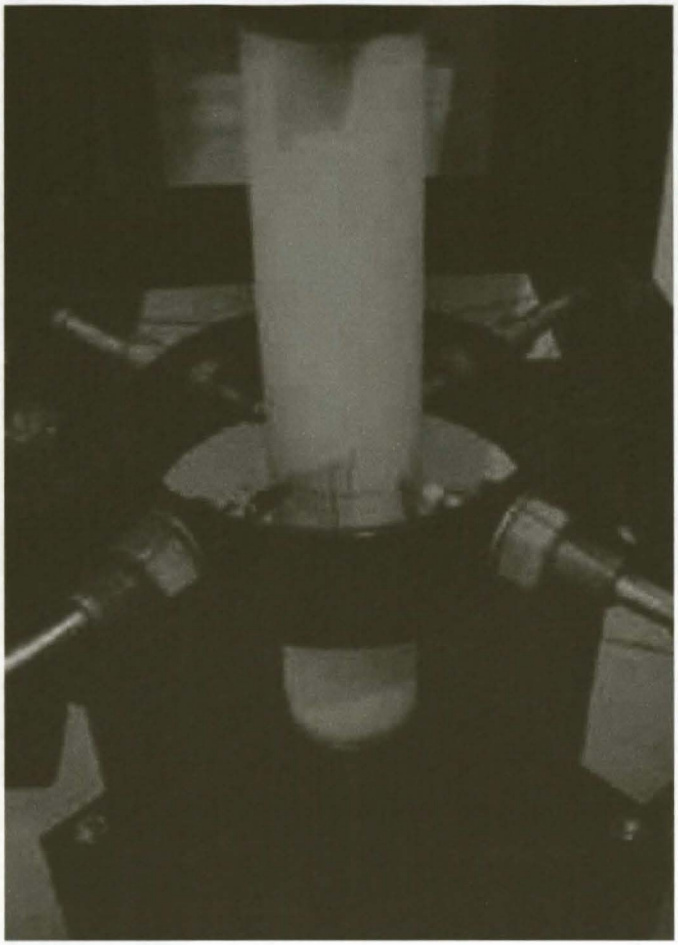

Figure C.4: The deflection recorder.

Figure C.5: The detonator holder.

Appendix D: Sample Test Recordings

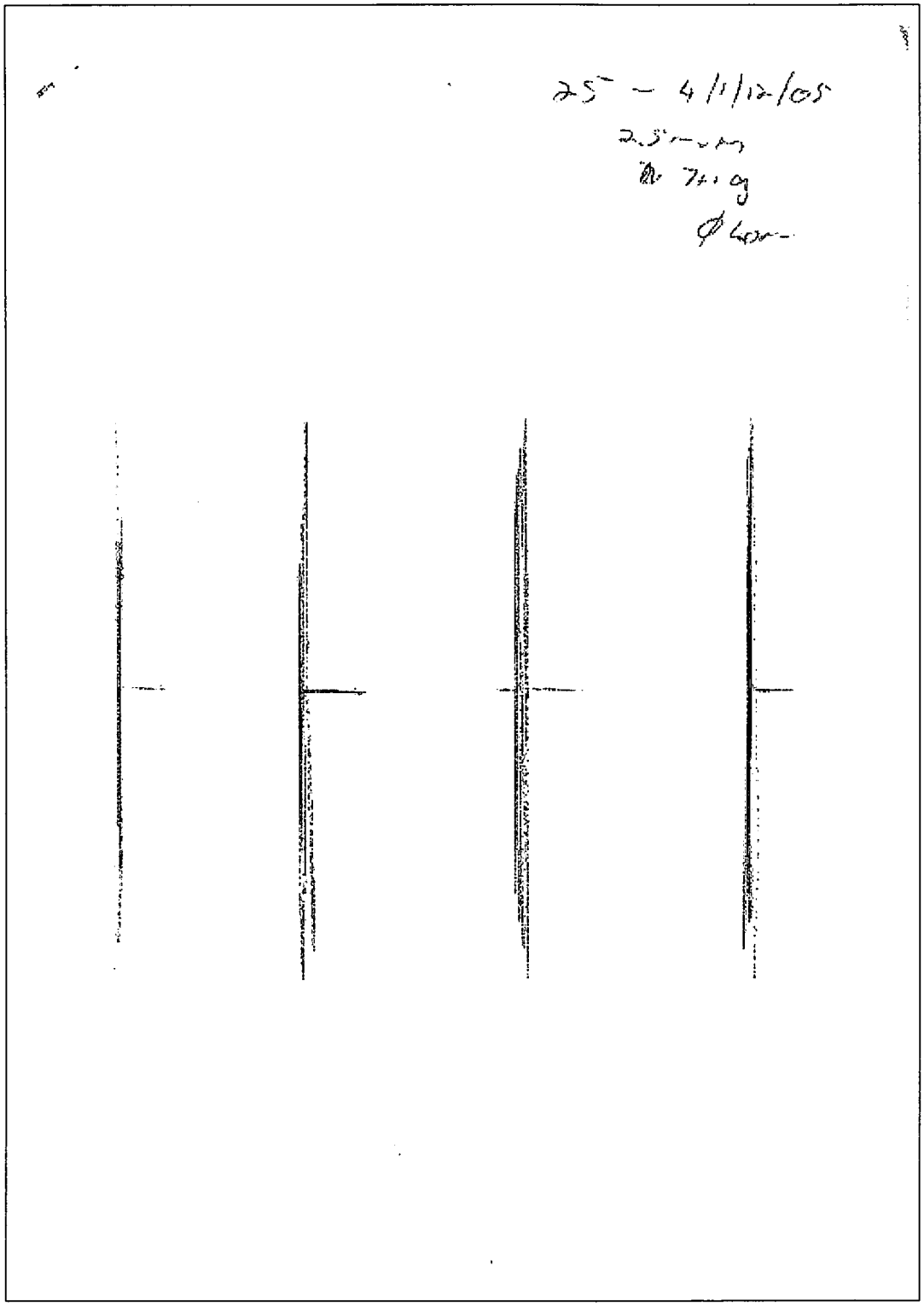

Figure D.1: A scan of an A4 sized page showing the peak recording of SMI25 test 4-1-12-05, charge mass of 7+1 g PE4, charge diameter 40 mm, specimen 2.5 mm mild steel plate. First peak amplitude 66.7 mm second peak amplitude 60 mm.

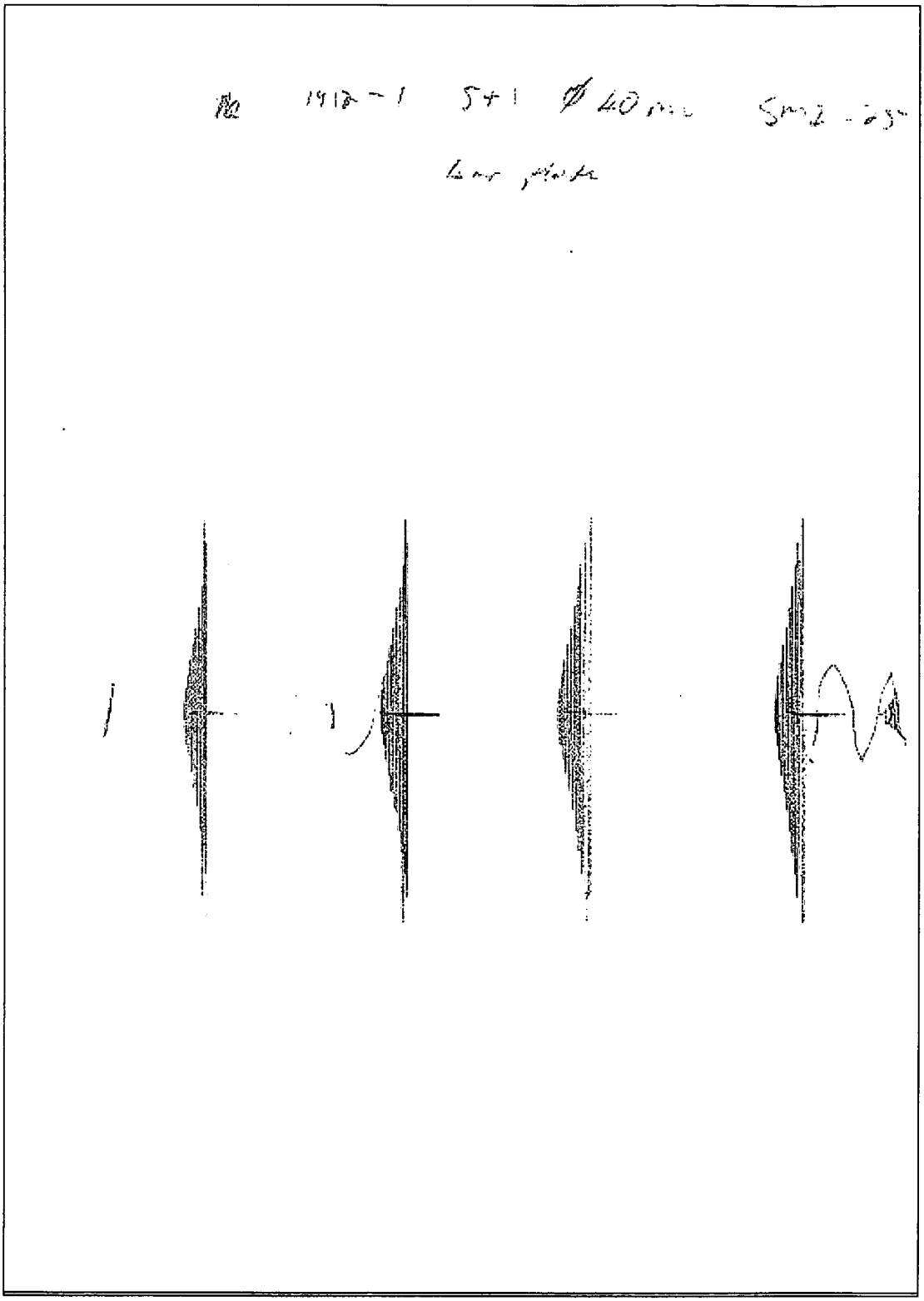

Figure D.2: A scan of an A4 sized page showing the peak recording of SMI25 test 1-19-12-05, charge mass of 5+1 g PE4, charge diameter 40 mm, specimen 4 mm mild steel plate. First peak amplitude 48.5 mm second peak amplitude 45.4 mm.

Appendix E: Spring Design and Testing

The SMI system was designed to operate as a modular system of springs and masses that can be combined to perform a series of impulse measurements from 10 N·s to 75 N·s. In order to achieve this modularity a set of three suspension springs was designed for minimum mass while taking available spring materials and manufacturing limitations into consideration. The minimum mass objective was set by the massless spring assumption used in the derivation of the system impulse response. The only readily available spring material was hard drawn carbon steel wire.

The design philosophy was also based on the fact that the springs were to be used under very controlled circumstances and that the factor of safety used to safeguard against spring material yielding could thus be kept to a minimum. A factor of safety of 1.2 (static) was used in all spring designs. The safety factor was raised further by the fact that the springs were specified to only operated in the central 75% of their range to maintain linearity. Spring constants were chosen along with target masses that would limit the peak velocity of the target mass to about 1 m/s. The lower peak velocity leads to reduced inertial forces and lowers the buckling risk in the target mass structure.

The variability in spring manufacture necessitated an approach of design and test, to check that the springs are fit for purpose. This approach worked well since it reduced the demands on the spring manufacturer and forced proper testing and characterisation of the suspension springs.

Fatigue failure was not considered in the design since the number of working cycles over the lifetime of the suspension spring is small. The operating frequency of the springs are in the order of 1 Hz, therefore the effects of a shockwave ravelling up the spring was the only concern. The loose coupling between the spring and the target mass due to the D-shackle joints reduces the severity of the shockwave transmitted to the suspension spring. The spring design was simplified through the use of W-shaped sheet metal spring ends that can easily be positioned to give a specific number of active. This improved the adjustability of the finished system while ensuring greater linearity than normal bent ends would.

A series of tensile tests were performed on each of the three suspension springs to determine their characteristics. Force-deflection data was collected during extension and contraction of the spring in each test. This data was then analysed to evaluate:

Spring coefficients.
Consistency of the spring coefficients.
Lower limit of linearity.
Pre-load magnitude.
Hysteresis.

The results of the tests were used to set the maximum load and maximum extension to avoid yielding as well as the spring mass and various useful parameters for test planning. The minimum mass of the target mass, for full scale defection was calculated to ensure that spring linearity is maintained for the given pre-load, spring coefficient and lower linearity limit. The dynamic load limit represents the largest target mass that may be used up to 100 mm response amplitudes without the risk that the spring response becomes non-linear. The test planning and evaluation data is presented in Table E.1 and E.2.

The force deflection graphs of the tests done on the springs are shown in Figure E.1 to Figure E.3, which are intended for condition monitoring purposes. The spring coefficients were found to be suitably linear and very constant with negligible hysteresis. The pre-load was poorly captured for the 25 N·s and 50 N·s spring tests.
The hysteresis in the 75 N·s test T4 was thought to have been caused by spring vibrations due to a suddenly applied crosshead motion.

A more convenient of quality control is to check that the measured free period of a SMI setup correlates to within 2% of the theoretical value. If spring mass is corrected for, any variations larger than 2% should be investigated by repeating the mass and period measurements, if that fails to solve the discrepancy the springs stiffness must be retested.

Table E.1: The spring characteristics of the SMI suspension springs.

Spring	Average Spring Coefficient [N/m]	Standard Deviation on Spring Coefficient [N/m]	Coefficient of Variation on Spring Coefficient Tests [%]	Pre-load [N]	Maximum Extension [mm]	Spring Mass [kg]	Minimum Extension for Linearity [mm]	Total Length [mm]
25 N·s	1595	1.7	0.11	145	500	2.6	20	500
50 N·s	3954	5.27	0.13	400	270	2.91	20	600
75 N·s	5873	2.95	0.05	400	270	4.97	20	750

Table E.2: The spring-based system characteristics of the SMI.

Spring	Maximum Static Load [N]	Minimum Target Mass for FSD Accuracy [kg]	Maximum Dynamic Load [N] 100 mm Amplitude]	τ min [s]	τ max [s]
25 N·s	943	35	783	0.931	1.406
50 N·s	1468	90	1072	0.948	1.045
75 N·s	1986	115	1398	0.879	0.979

Table E.3: Arrestor spring details.

Arrestor Spring	
12	Wire diameter [mm]
45	Inner diameter [mm]
17	Number of coils
1631	Preload [N]
65305	Stiffness [N/m]
1.5	SF on 30 mm extension
1.2	SF on 40 mm extension

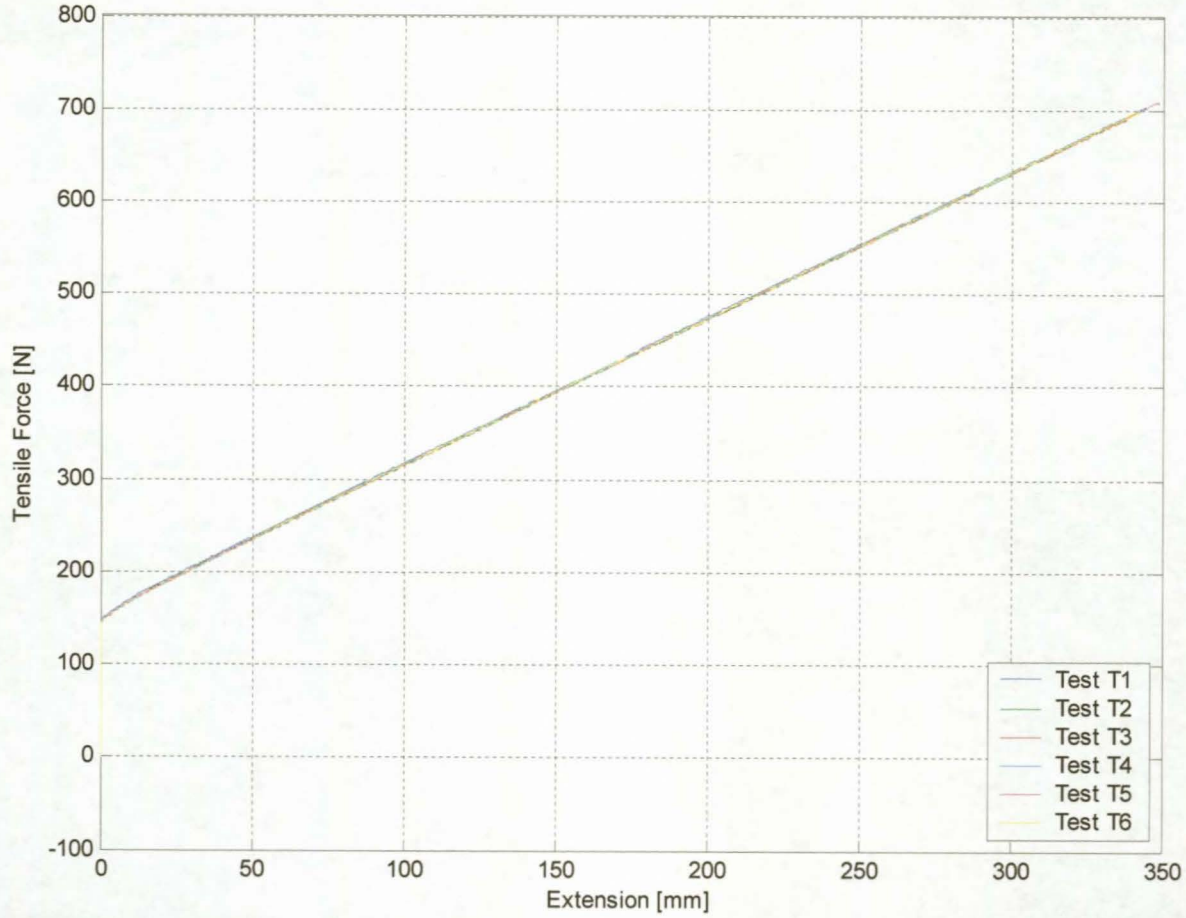

Figure E.1: 25 N·s spring test results.

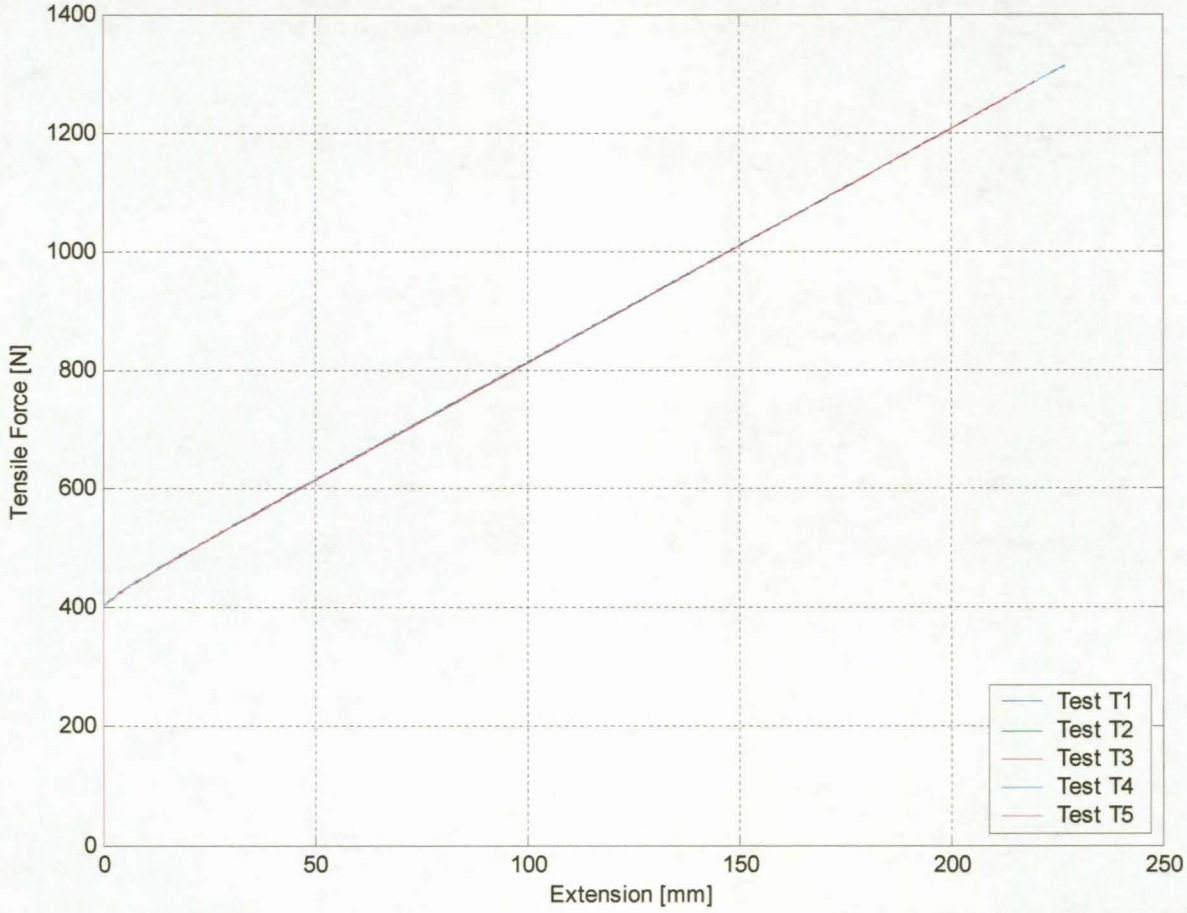

Figure E.2: 50 N·s spring test results.

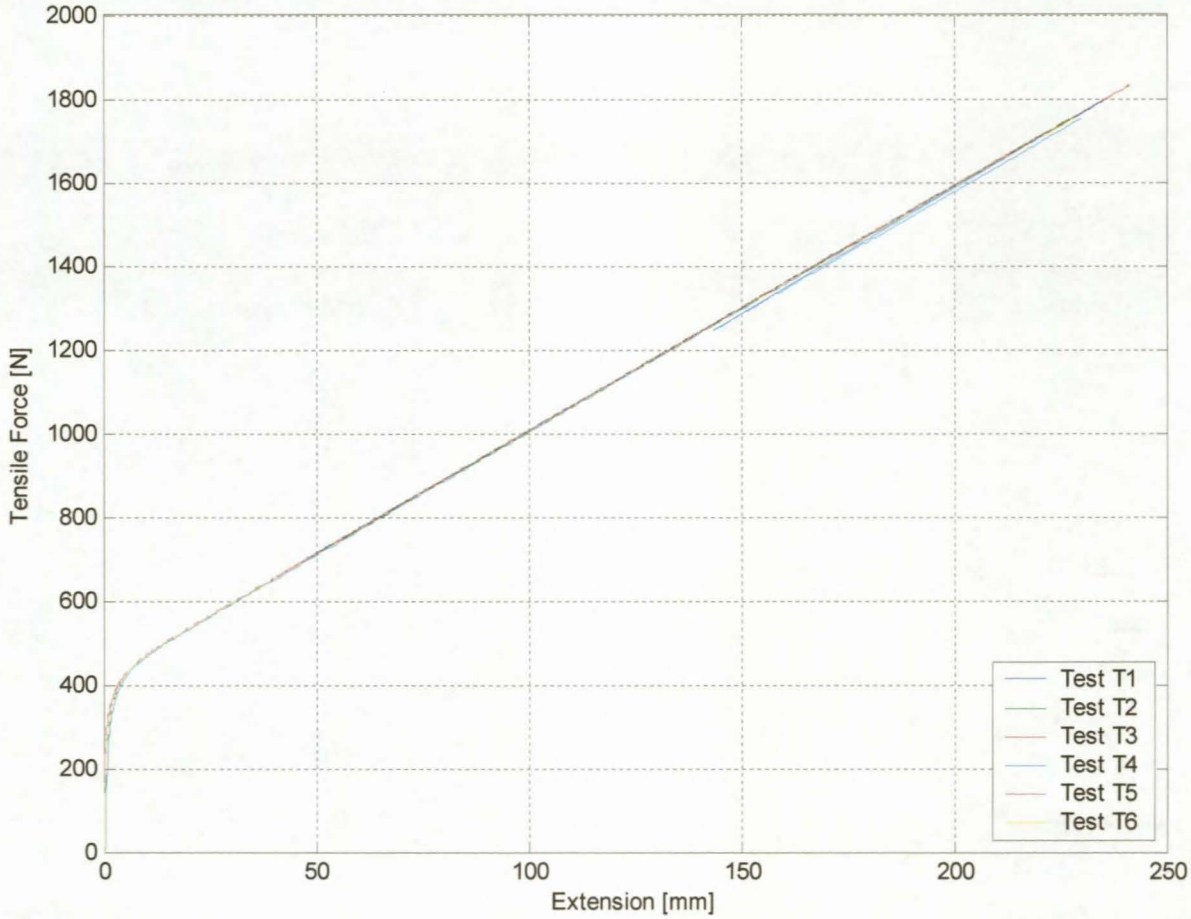

Figure E.3: 75 N·s spring test results.

Table E.3: Arrestor spring details.

Arrestor Spring	
12	Wire diameter [mm]
45	Inner diameter [mm]
17	Number of coils
1631	Preload [N]
65305	Stiffness [N/m]
1.5	SF on 30 mm extension
1.2	SF on 40 mm extension

Appendix F: Test Data

Table F.1: SMI test data.

Specimen	Explosive Mass [g]	Charge Diameter [mm]	Plate Thickness [mm]	Impulse [N·s]	Nurick Dimensionless Number	Midpoint Deflection [mm]	Deflection /Thickness	Experiment Comments	Spring Stiffness [N/m]	Corrected Target Mass [kg]
SMI25-QT-0711-1	3	33	1.61	5.4	24.8	14.5	9.0	-	1595	37.80
SMI25-QT-0711-2	7	33	1.61	14.1	-	-	-	Capped	1595	37.80
SMI25-QT-0711-3	5	33	1.61	10.1	-	-	-	Capped	1595	37.80
SMI25-QT-0711-1	3	33	1.61	5.2	24.0	14.5	9.0	-	1595	37.80
SMI25-1A-30-10-06	3.25	33	1.69	6.4	22.5	15.8	9.3	-	1595	37.76
SMI25-2-30-10-06	3.5	33	1.70	7.0	24.2	17.9	10.6	-	1595	37.76
SMI25-3-30-10-06	3.75	33	1.68	7.2	25.5	19.6	11.7	-	1595	37.76
SMI25-4-30-10-06	4	33	1.68	7.7	27.3	20.9	12.4	-	1595	37.76
SMI25-4A-30-10-06	4.25	33	1.68	8.6	30.4	21.7	12.9	-	1595	37.76
SMI25-1-31-10-06	4.25	33	1.68	8.2	28.9	21.4	12.8	-	1595	37.76
SMI25-5-30-10-06	8.5	40	2.54	17.2	22.4	24.9	9.8	-	1595	38.86
SMI25-QT-0112-1	5	40	2.54	10.3	13.4	16.1	6.3	-	1595	37.80
SMI25-QT-0112-2	5	40	2.54	10.2	13.3	14.9	5.9	-	1595	37.80
SMI25-QT-0112-3	8	40	2.54	16.9	22.1	25.1	9.9	-	1595	37.80
SMI25-QT-0112-4	8	40	2.54	16.7	21.8	23.4	9.2	-	1595	37.80
1912-1	6	40	4.11	12.0	6.4	11.0	2.7	-	1595	37.80
1912-2	10	40	4.11	19.8	10.4	15.9	3.9	-	1595	37.80
1912-3	13	40	4.11	26.3	13.9	21.4	5.2	-	1595	37.80
1912-4	13	40	4.11	26.3	13.9	21.4	5.2	-	1595	37.80
1912-5	16	40	4.11	31.3	16.5	25.2	6.1	-	3954	99.80

Table F.1 (cont.): SMI test data.

Specimen	Explosive Mass [g]	Charge Diameter [mm]	Plate Thickness [mm]	Impulse [N·s]	Nurick Dimensionless Number	Midpoint Deflection [mm]	Deflection /Thickness	Experiment Comments	Spring Stiffness [N/m]	Corrected Target Mass [kg]
17/05/06-1	16	40	4.08	31.4	16.8	24.2	5.9	-	3954	100.50
17/05/06-2	19	40	4.06	36.2	19.6	28.4	7.0	-	3954	100.50
17/05/06-3	19	40	4.11	35.5	18.8	28.3	6.9	-	3954	100.50
17/05/06-4	24	40	2.48x2	44.4	-	27.3	-	Top plate capped	3954	100.50
17/05/06-5	24	40	2.52+2.53	45.4	-	27.6	-	Top plate capped	3954	100.50
18/05/06-1	28	40	4.12+2.53	50.8	-	58.6	-	Top plate capped	5873	119.70
18/05/06-2	28	40	4.09+2.54	49.5	-	59.3	-	Top plate capped	5873	119.70
SMI25-1-30-10-06	3.25	33	1.69	2.6	9.1	7.7	4.6	Deflagrated	1595	37.76
SMI50-1-1-11-06	10	40	20	18.6	-	-	-	Rigid specimen	3954	127.23
SMI50-2-1-11-06	20	40	20	35.6	-	-	-	Rigid specimen	3954	127.23
SMI50-3-1-11-06	25	40	20	43.2	-	-	-	Rigid specimen	3954	127.23
SMI50-4-1-11-06	30	40	20	51.0	-	-	-	Rigid specimen	3954	127.23
SMI75-1-31-10-06	30	40	20	46.4	-	-	-	Rigid specimen - loose bolt	3954	127.38
SMI75-5-1-11-06	10	40	20	20.0	-	-	-	Rigid specimen	5873	127.92
SMI75-6-1-11-06	15	40	20	30.6	-	-	-	Rigid specimen	5873	127.92
SMI75-7-1-11-06	20	40	20	36.3	-	-	-	Rigid specimen	5873	127.92
SMI75-8-1-11-06	25	40	20	48.3	-	-	-	Rigid specimen	5873	127.92
SMI75-9-1-11-06	30	40	20	54.6	-	-	-	Rigid specimen	5873	127.92
SMI75-10-1-11-06	38	40	20	63.7	-	-	-	Rigid specimen	5873	127.92

Appendix G: Multimedia CD

The Compact disk attached to this section contains video and images files that depict the SMI system and some of the plate bulge tests.